EUROPEAN ORGANIZATION FOR NUCLEAR RESEARCH

ALICE-ANA-2016-xxx
February 27, 2018

Lambda-Kaon and Cascade-Kaon Femtoscopy in Pb-Pb Collisions at $\sqrt{s_{NN}} = 2.76$ TeV from the LHC ALICE Experiment

Jesse T. Buxton[1]

1. Department of Physics, The Ohio State University, Columbus, Ohio, USA

Email: jesse.thomas.buxton@cern.ch

Abstract

We present results from a femtoscopic analysis of Lambda-Kaon correlations in Pb-Pb collisions at $\sqrt{s_{NN}}$ = 2.76 TeV by the ALICE experiment at the LHC. All pair combinations of Λ and $\bar{\Lambda}$ with K^+, K^- and K^0_S are analyzed. The femtoscopic correlations are the result of strong final-state interactions, and are fit with a parametrization based on a model by R. Lednicky and V. L. Lyuboshitz [1]. This allows us to both characterize the emission source and measure the scattering parameters for the particle pairs. We observe a large difference in the Λ-K^+ ($\bar{\Lambda}$-K^-) and Λ-K^- ($\bar{\Lambda}$-K^+) correlations in pairs with low relative momenta ($k^* \lesssim 100$ MeV). Additionally, the average of the Λ-K^+ ($\bar{\Lambda}$-K^-) and Λ-K^- ($\bar{\Lambda}$-K^+) correlation functions is consistent with our Λ-K^0_S ($\bar{\Lambda}$-K^0_S) measurement. The results suggest an effect arising from different quark-antiquark interactions in the pairs, i.e. $s\bar{s}$ in Λ-K^+ ($\bar{\Lambda}$-K^-) and $u\bar{u}$ in Λ-K^- ($\bar{\Lambda}$-K^+). To gain further insight into this hypothesis, we currently are conducting a Ξ-K femtoscopic analysis.

Contents

List of Figures

1 Introduction

We present results from a femtoscopic analysis of Lambda-Kaon correlations in Pb-Pb collisions at $\sqrt{s_{NN}}$ = 2.76 TeV by the ALICE experiment at the LHC. All pair combinations of Λ and $\bar{\Lambda}$ with K^+, K^- and K^0_S are analyzed. The femtoscopic correlations are the result of strong final-state interactions, and are fit with a parametrization based on a model by R. Lednicky and V. L. Lyuboshitz [1]. This allows us to both characterize the emission source and measure the scattering parameters for the particle pairs. We observe a large difference in the Λ-K^+ ($\bar{\Lambda}$-K^-) and Λ-K^- ($\bar{\Lambda}$-K^+) correlations in pairs with low relative momenta ($k^* \lesssim 100$ MeV). Additionally, the average of the Λ-K^+ ($\bar{\Lambda}$-K^-) and Λ-K^- ($\bar{\Lambda}$-K^+) correlation functions is consistent with our Λ-K^0_S ($\bar{\Lambda}$-K^0_S) measurement. The results suggest an effect arising from different quark-antiquark interactions in the pairs, i.e. $s\bar{s}$ in Λ-K^+ ($\bar{\Lambda}$-K^-) and $u\bar{u}$ in Λ-K^- ($\bar{\Lambda}$-K^+). To gain further insight into this hypothesis, we currently are conducting a Ξ-K femtoscopic analysis.

2 Data Sample and Software

2.1 Data Sample

The analysis used "pass 2" reconstructed Pb-Pb data from LHC11h (AOD145). The runlist was selected from runs with global quality tag "1" in the ALICE Run Condition Table. Approximately 40 million combined central, semi-central, and minimum bias events were analyzed. Runs from both positive (++) and negative (--) magnetic field polarity settings were used.

Run list: 170593, 170572, 170388, 170387, 170315, 170313, 170312, 170311, 170309, 170308, 170306, 170270, 170269, 170268, 170230, 170228, 170207, 170204, 170203, 170193, 170163, 170159, 170155, 170091, 170089, 170088, 170085, 170084, 170083, 170081, 170040, 170027, 169965, 169923, 169859, 169858, 169855, 169846, 169838, 169837, 169835, 169591, 169590, 169588, 169587, 169586, 169557, 169555, 169554, 169553, 169550, 169515, 169512, 169506, 169504, 169498, 169475, 169420, 169419, 169418, 169417, 169415, 169411, 169238, 169167, 169160, 169156, 169148, 169145, 169144, 169138, 169099, 169094, 169091, 169045, 169044, 169040, 169035, 168992, 168988, 168826, 168777, 168514, 168512, 168511, 168467, 168464, 168460, 168458, 168362, 168361, 168342, 168341, 168325, 168322, 168311, 168310, 168115, 168108, 168107, 168105, 168076, 168069, 167988, 167987, 167985, 167920, 167915

Analysis was also performed on the LHC12a17a_fix (AOD149) Monte Carlo HIJING events for certain checks. THERMINATOR2 was also used for certain aspects, such as transform matrices described feed-down contributions.

2.2 Software

The analysis was performed on the PWGCF analysis train using AliRoot v5-08-18-1 and AliPhysics vAN-20161027-1.

The main classes utilized include: AliFemtoVertexMultAnalysis, AliFemtoEventCutEstimators, AliFemtoESDTrackCutNSigmaFilter, AliFemtoV0TrackCutNSigmaFilter, AliFemtoXiTrackCut, AliFemtoV0PairCut, AliFemtoV0TrackPairCut, AliFemtoXiTrackPairCut, and AliFemtoAnalysisLambdaKaon. All of these classes are contained in /AliPhysics/PWGCF/FEMTOSCOPY/AliFemto and .../AliFemtoUser.

3 Data Selection

3.1 Event Selection and Mixing

The events used in this study were selected with the class AliFemtoEventCutEstimators according to the following criteria:

- Triggers
  - minimum bias (kMB)
  - central (kCentral)
  - semi-central (kSemiCentral)
- z-position of reconstructed event vertex must be within 10 cm of the center of the ALICE detector
- the event must contain at least one particle of each type from the pair of interest

The event mixing was handled by the AliFemtoVertexMultAnalysis class, which only mixes events with like vertex position and centrality. The following criteria were used for event mixing:

- Number of events to mix = 5
- Vertex position bin width = 2 cm
- Centrality bin width = 5

The AliFemtoEventReaderAODChain class is used to read the events. Event flatteneing is not currently used. FilterBit(7). The centrality is determined by the "V0M" method of AliCentrality, set by calling AliFemtoEventReaderAOD::SetUseMultiplicity(kCentrality). I utilize the SetPrimaryVertexCorrectionTPCPoints switch, which causes the reader to shift all TPC points to be relative to the event vertex.

3.2 $K^{\pm}$ Track Selection

Charged kaons are identified using the AliFemtoESDTrackCutNSigmaFilter class. The specific cuts used in this analysis are as follows:

Track Selection:

- Kinematic range:
  - $0.14 < p_{\mathrm{T}} < 1.5$ GeV/c
  - $|\eta| < 0.8$
- FilterBit(7)
  - TPC tracks
- Track Quality
  - Minimum number of clusters in the TPC (fminTPCncls) = 80
  - Maximum allowed χ^2/N_{DOF} for ITS clusters = 3.0
  - Maximum allowed χ^2/N_{DOF} for TPC clusters = 4.0
- Primary Particle Selection:
  - Maximum XY impact parameter = 2.4 cm
  - Maximum Z impact parameter = 3.0 cm
- Remove particles with any kink labels (fRemoveKinks = true)
- Maximum allowed sigma to primary vertex (fMaxSigmaToVertex) = 3.0

$K^{\pm}$ Identification:

- PID Probabilities:
  - K: > 0.2
  - π: < 0.1
  - μ: < 0.8
  - p: < 0.1
- Most probable particle type must be Kaon (fMostProbable=3)
- TPC and TOF N_{σ} cuts:
  - $p < 0.4$ GeV/c: $N_{\sigma K,TPC} < 2$
  - $0.4 < p < 0.45$ GeV/c: $N_{\sigma K,TPC} < 1$
  - $0.45 < p < 0.8$ GeV/c: $N_{\sigma K,TPC} < 3$ & $N_{\sigma K,TOF} < 2$
  - $0.8 < p < 1.0$ GeV/c: $N_{\sigma K,TPC} < 3$ & $N_{\sigma K,TOF} < 1.5$
  - $p > 1.0$ GeV/c: $N_{\sigma K,TPC} < 3$ & $N_{\sigma K,TOF} < 1$
- Electron Rejection: Reject if $N_{\sigma e^{-},TPC} < 3$
- Pion Rejection: Reject if:
  - $p < 0.65$ GeV/c
    * if TOF and TPC available: $N_{\sigma\pi,TPC} < 3$ & $N_{\sigma\pi,TOF} < 3$
    * else
      · $p < 0.5$ GeV/c: $N_{\sigma\pi,TPC} < 3$
      · $0.5 < p < 0.65$ GeV/c: $N_{\sigma\pi,TPC} < 2$
  - $0.65 < p < 1.5$ GeV/c: $N_{\sigma\pi,TPC} < 5$ & $N_{\sigma\pi,TOF} < 3$
  - $p > 1.5$ GeV/c: $N_{\sigma\pi,TPC} < 5$ & $N_{\sigma\pi,TOF} < 2$

The purity of the $K^{\pm}$ collections was estimated using the MC data, for which the true identity of each reconstructed $K^{\pm}$ particle is known. Therefore, the purity may be estimated as:

$$Purity(K^{\pm}) = \frac{N_{true}}{N_{reconstructed}} \tag{1}$$

Purity(K^{+}) $\approx$ Purity(K^{-}) $\approx 97\%$

3.3 V0 Selection

Λ ($\bar{\Lambda}$) and K^{0}_{S} are neutral particles which cannot be directly detected, but must instead be reconstructed through detection of their decay products, or daughters. This process is illustrated in Figure 1. In general, particles which are topologically reconstructed in this fashion are called V0 particles. The class AliFemtoV0TrackCutNSigmaFilter (which is an extension of AliFemtoV0TrackCut) is used to reconstruct the V0s.

In order to obtain a true and reliable signal, one must ensure good purity of the V0 collection. The purity of the collection is calculated as:

$$Purity = \frac{Signal}{Signal + Background} \tag{2}$$

To obtain both the signal and background, the invariant mass distribution (m_{inv}) of all V0 candidates must be constructed immediately before the final invariant mass cut. Examples of such distribtions can be found in Figures 3 and 5. It is vital that this distribution be constructed immediately before the final m_{inv} cut, otherwise it would be impossible to estimate the background. As shown in Figures 3 and 5, the background is fit (with a polynomial) outside of the peak region of interest to obtain an estimate for the backfround within the region. Within the m_{inv} cut limits, the background is the region below the fit while the signal is the region above the fit.

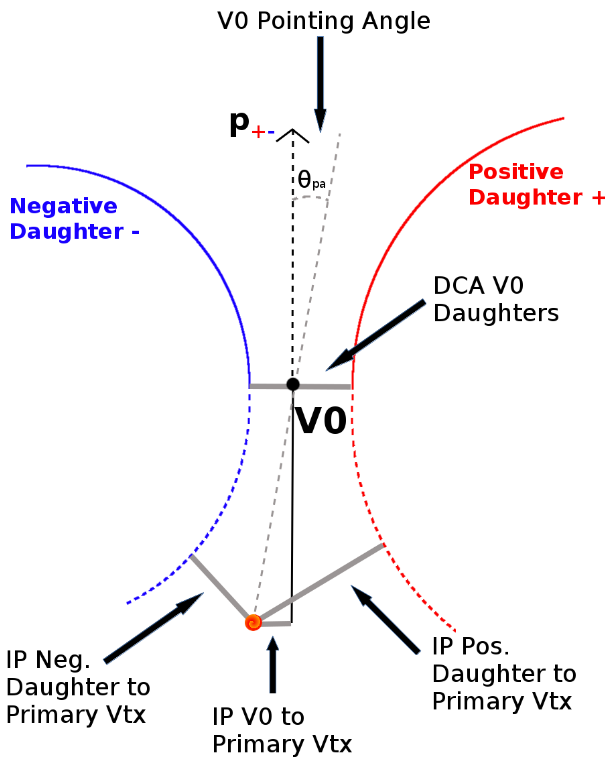

Fig. 1: V0 Reconstruction

3.3.1 Λ Reconstruction

The following cuts were used to select good Λ ($\bar{\Lambda}$) candidates:

1. Daughter Particle Cuts
   (a) Cuts Common to Both Daughters
      i. $|\eta| < 0.8$
      ii. SetTPCnclsDaughters(80)
      iii. SetStatusDaughters(AliESDtrack::kTPCrefit)
      iv. DCA πp Daughters < 0.4 cm
   (b) Pion Specific Daughter Cuts
      i. $p_{\mathrm{T}} > 0.16$ GeV/c
      ii. DCA to prim vertex > 0.3 cm
      iii. TPC and TOF Nσ Cuts
         A. $p < 0.5$ GeV/c : N$\sigma_{\mathrm{TPC}} < 3$
         B. $p > 0.5$ GeV/c :

- if TOF & TPC available: N$\sigma_{\mathrm{TPC}} < 3$ & N$\sigma_{\mathrm{TOF}} < 3$
- else N$\sigma_{\mathrm{TOF}} < 3$

(c) Proton Specific Daughter Cuts

i. $p_{\mathrm{T}} > 0.5(p)$ $[0.3(\bar{p})]$ GeV/c

ii. DCA to prim vertex > 0.1 cm

iii. TPC and TOF Nσ Cuts

A. $p < 0.8$ GeV/c : N$\sigma_{\mathrm{TPC}} < 3$

B. $p > 0.8$ GeV/c :

- if TOF & TPC available: N$\sigma_{\mathrm{TPC}} < 3$ & N$\sigma_{\mathrm{TOF}} < 3$
- else N$\sigma_{\mathrm{TOF}} < 3$

2. V0 Cuts

(a) $|\eta| < 0.8$

(b) $p_{\mathrm{T}} > 0.4$ GeV/c

(c) $|m_{\mathrm{inv}} - m_{\mathrm{PDG}}| < 3.8$ MeV

(d) DCA to prim. vertex < 0.5 cm

(e) Cosine of pointing angle > 0.9993

(f) OnFlyStatus = false

(g) Decay Length < 60 cm

3. Shared Daughter Cut for V0 Collection

- Iterate through V0 collection to ensure that no daughter is used in more than one V0 candidate

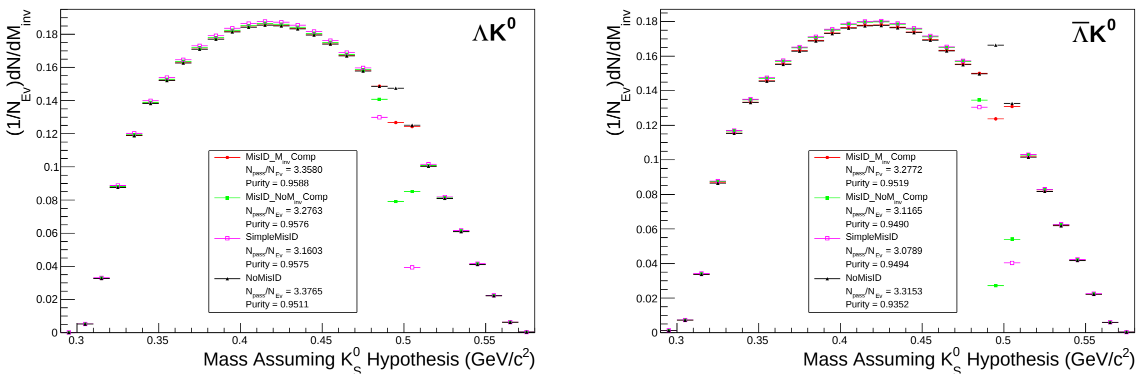

(a) Mass assuming K^0_S-hypothesis for Λ collection, i.e. assume the daughters are $\pi^+\pi^-$ instead of $p^+\pi^-$.

(b) Mass assuming K^0_S-hypothesis for $\bar{\Lambda}$ collection, i.e. assume the daughters are $\pi^+\pi^-$ instead of $\pi^+\bar{p}^-$.

Fig. 2: Mass assuming K^0_S-hypothesis for V0 candidates passing all Λ (2a) and $\bar{\Lambda}$ (2b) cuts. The "NoMisID" distribution (black triangles) uses the V0 finder without any attempt to remove misidentified K^0_S. The slight peak in the "NoMisID" distribution around m_{inv} = 0.5 GeV/c^2 contains misidentified K^0_S particles in our $\Lambda(\bar{\Lambda})$ collection. "SimpleMisID" (pink squares) simply cuts out the entire peak, which throws away some good Λ and $\bar{\Lambda}$ particles. "MisID_NoM$_{\mathrm{inv}}$Comp" (green squares) uses the misidentification cut outlined in the text, but does not utilize the invariant mass comparison method. "MisID_M$_{\mathrm{inv}}$Comp" (red circles) utilizes the full misidentification methods, and is currently used for this analysis. "N$_{pass}$/N$_{ev}$" is the total number of $\Lambda(\bar{\Lambda})$ particles found, normalized by the total number of events. The purity of the collection is also listed.

Figure 2a shows the mass assuming K^0_S hypothesis for the Λ collection, i.e. assume the daughters are $\pi^+\pi^-$ instead of $\pi^+\bar{p}^-$. Figure 2b is a similar plot, but is for the $\bar{\Lambda}$ collection, i.e. assume the daughters are $\pi^+\pi^-$ instead of $\pi^+\bar{p}^-$. The K^0_S contamination is visible, although not profound, in both in the slight peaks around $m_{\rm inv} = 0.497$ GeV/c^2. If one simply cuts out the entire peak, good Λ particles will be lost. Ideally, the Λ selection and K^0_S misidentification cuts are selected such that the peak is removed from this plot while leaving the distribution continuous. To attempt to remove these K^0_S contaminations without throwing away good Λ and $\bar{\Lambda}$ particles, the following misidentification cuts are imposed; a $\Lambda(\bar{\Lambda})$ candidate is rejected if all of the following criteria are satisfied:

- $\left|m_{\text{inv, K}^0_S\text{ Hypothesis}} - m_{\text{PDG, K}^0_S}\right| < 9.0$ MeV/c^2
- Positive and negative daughters pass π daughter cut implemented for K^0_S reconstruction
- $\left|m_{\text{inv, K}^0_S\text{ Hypothesis}} - m_{\text{PDG, K}^0_S}\right| < \left|m_{\text{inv, }\Lambda(\bar{\Lambda})\text{ Hypothesis}} - m_{\text{PDG, }\Lambda(\bar{\Lambda})}\right|$

Figure 3 shows the invariant mass ($m_{\rm inv}$) distribution of all $\Lambda(\bar{\Lambda})$ candidates immediately before the final invariant mass cut. These distributions are used to calculate the collection purities. The Λ and $\bar{\Lambda}$ purities are found to be: Purity(Λ) $\approx$ Purity($\bar{\Lambda}$) $\approx$ 95%.

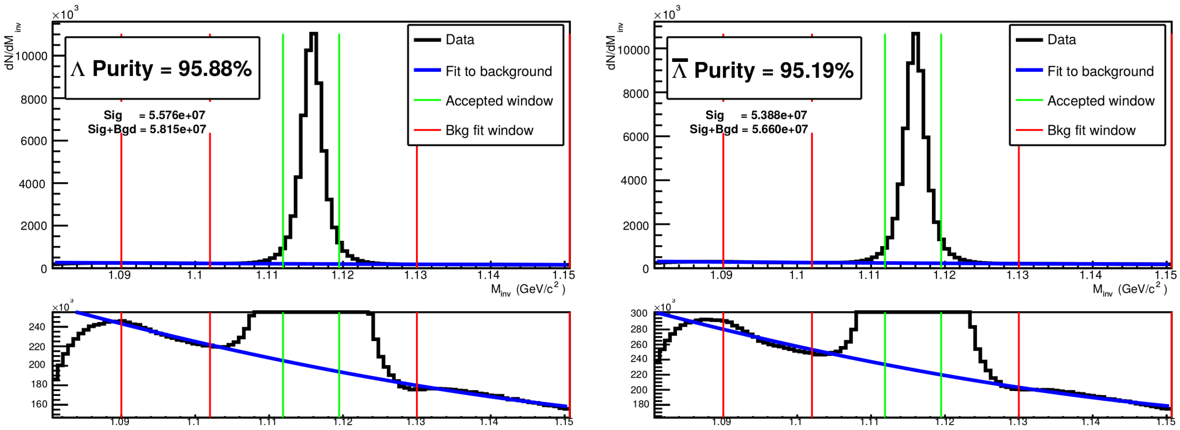

(a) Λ Purity (b) $\bar{\Lambda}$ Purity

Fig. 3: Invariant mass ($m_{\rm inv}$) distribution of all Λ (a) and $\bar{\Lambda}$ (b) candidates immediately before the final invariant mass cut. The bottom figures are zoomed to show the background with fit. The vertical green lines represent the $m_{\rm inv}$ cuts used in the analyses, the red vertical lines delineate the region over which the background was fit, and the blue line shows the background fit. These distributions are used to calculate the collection purities, Purity(Λ) $\approx$ Purity($\bar{\Lambda}$) $\approx$ 95%.

3.3.2 K^0_S Reconstruction

The following cuts were used to select good K^0_S candidates:

1. Pion Daughter Cuts
   (a) $|\eta| < 0.8$
   (b) SetTPCnclsDaughters(80)
   (c) SetStatusDaughters(AliESDtrack::kTPCrefic)
   (d) DCA $\pi^+\pi^-$ Daughters < 0.3 cm

(e) $p_T > 0.15$ GeV/c

(f) DCA to prim vertex > 0.3 cm

(g) TPC and TOF Nσ Cuts

i. $p < 0.5$ GeV/c : N$\sigma_{\rm TPC} < 3$

ii. $p > 0.5$ GeV/c :

– if TOF & TPC available: N$\sigma_{\rm TPC} < 3$ & N$\sigma_{\rm TOF} < 3$

– else N$\sigma_{\rm TOF} < 3$

2. K^0_S Cuts

(a) $|\eta| < 0.8$

(b) $p_T > 0.2$ GeV/c

(c) $m_{PDG} - 13.677$ MeV $< m_{\rm inv} < m_{\rm PDG} + 2.0323$ MeV

(d) DCA to prim. vertex < 0.3 cm

(e) Cosine of pointing angle > 0.9993

(f) OnFlyStatus = false

(g) Decay Length < 30 cm

3. Shared Daughter Cut for V0 Collection

– Iterate through V0 collection to ensure that no daughter is used in more than one V0 candidate

As can be seen in Figure 4, some misidentified Λ and $\bar{\Lambda}$ particles contaminate our K^0_S sample. Figure 4a shows the mass assuming Λ-hypothesis for the K^0_S collection, i.e. assume the daughters are $p^+\pi^-$ instead of $\pi^+\pi^-$. Figure 4b is similar, but shows the mass assuming $\bar{\Lambda}$ hypothesis for the collection, i.e. assume the daughters are $\pi^+\bar{p}^-$ instead of $\pi^+\pi^-$. The Λ contamination can be seen in 4a, and the $\bar{\Lambda}$ contamination in 4b, in the peaks around $m_{\rm inv}$ = 1.115 GeV/c^2. Additionally, the $\bar{\Lambda}$ contamination is visible in Figure 4a, and the Λ contamination visible in Figure 4b, in the region of excess around 1.65 $< m_{\rm inv} < 2.1$ GeV/c^2. This is confirmed as the number of misidentified Λ particles in the sharp peak of Figure 4a (misidentified $\bar{\Lambda}$ particles in the sharp peak of Figure 4b) approximately equals the excess found in the $1.65 < m_{\rm inv} < 2.1$ GeV/c^2 region of Figure 4a (Figure 4b).

The peaks around $m_{\rm inv} = 1.115$ GeV/c^2 in Figure 4 contain both misidentified Λ ($\bar{\Lambda}$) particles and good K^0_S. If one simply cuts out the entire peak, some good K^0_S particles will be lost. Ideally, the K^0_S selection and $\Lambda(\bar{\Lambda})$ misidentification cuts can be selected such that the peak is removed from this plot while leaving the distribution continuous. To attempt to remove these Λ and $\bar{\Lambda}$ contaminations without throwing away good K^0_S particles, the following misidentification cuts are imposed; a K^0_S candidate is rejected if all of the following criteria are satisfied (for either Λ or $\bar{\Lambda}$ hypothesis):

– $\left| m_{\rm inv,\ \Lambda(\bar{\Lambda})\ Hypothesis} - m_{\rm PDG,\ \Lambda(\bar{\Lambda})} \right| < 9.0$ MeV/c^2

– Positive daughter passes $p^+(\pi^+)$ daughter cut implemented for $\Lambda(\bar{\Lambda})$ reconstruction

– Negative daughter passes $\pi^-(\bar{p}^-)$ daughter cut implemented by $\Lambda(\bar{\Lambda})$ reconstruction

– $\left| m_{\rm inv,\ \Lambda(\bar{\Lambda})\ Hypothesis} - m_{\rm PDG,\ \Lambda(\bar{\Lambda})} \right| < \left| m_{{\rm inv,\ K^0_S\ Hypothesis}} - m_{{\rm PDG,\ K^0_S}} \right|$

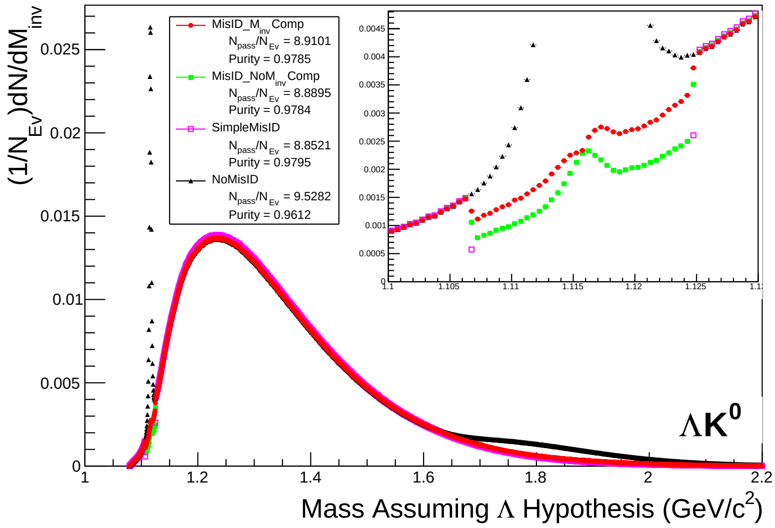

(a) Mass assuming Λ-hypothesis for K^0_S collection, i.e. assume the daughters are $p^+\pi^-$ instead of $\pi^+\pi^-$.

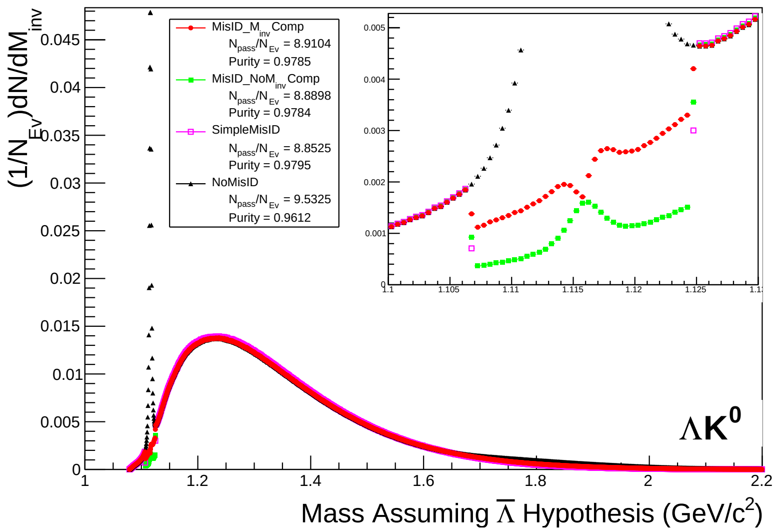

(b) Mass assuming $\bar{\Lambda}$-hypothesis for K^0_S collection, i.e. assume the daughters are $\pi^+\bar{p}^-$ instead of $\pi^+\pi^-$.

Fig. 4: Mass assuming Λ-hypothesis (4a) and $\bar{\Lambda}$-hypothesis (4b) for K^0_S collection. The "NoMisID" distribution (black triangles) uses the V0 finder without any attempt to remove misidentified Λ and $\bar{\Lambda}$. The peak in the "NoMisID" distribution around $m_{\text{inv}} = 1.115$ GeV/c^2 contains misidentified Λ (4a) and $\bar{\Lambda}$ (4b) particles in our K^0_S collection. "SimpleMisID" (pink squares) simply cuts out the entire peak, which throws away some good K^0_S particles. "MisID_NoM$_{inv}$Comp" (green squares) uses the misidentification cut outlined in the text, but does not utilize the invariant mass comparison method. "MisID_M$_{inv}$Comp" (red circles) utilizes the full misidentification methods, and is currently used for this analysis. "N$_{pass}$/N$_{ev}$" is the total number of K^0_S particles found, normalized by the total number of events. The purity of the collection is also listed. Also note, the relative excess of the "NoMisID" distribution around $1.65 < m_{\text{inv}} < 2.1$ GeV/c^2 shows misidified $\bar{\Lambda}$ (4a) and Λ (4b) particles in our K^0_S collection.

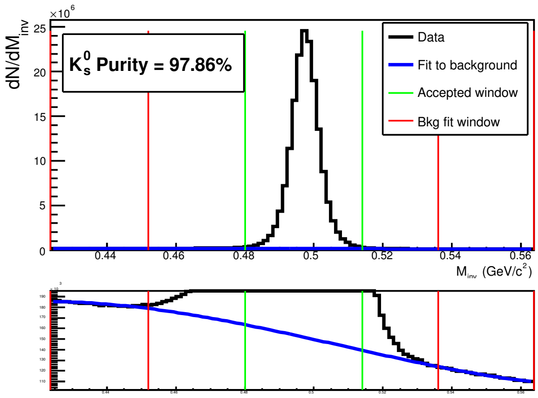

Fig. 5: Invariant mass (m_{inv}) distribution of all K^0_S candidates immediately before the final invariant mass cut. The bottom figure is zoomed to show the background with fit. The vertical green lines represent the m_{inv} cut used in the analyses, the red vertical lines delineate the region over which the background was fit, and the blue line shows the background fit. This distribution is used to calculate the collection purity, Purity(K^0_S) $\approx$ 98%.

3.4 Cascade Reconstruction

Our motivation for studying $\Xi K^{\pm}$ systems is to hopefully better understand the striking difference in the ΛK^{+} and ΛK^{-} data at low k^{*} (Figure 14).

The reconstruction of Ξ particles is one step above V0 reconstruction. V0 particles are topologically reconstructed by searching for the charged daughters' tracks into which they decay. With Ξ particles, we search for the V0 particle and charged daughter into which the Ξ decays. In the case of Ξ^{-}, we search for the Λ (V0) and π^{-} (track) daughters. We will refer to this π as the "bachelor π".

The following cuts were used to select good Ξ^{-} ($\bar{\Xi}^{+}$) candidates:

1. V0 Daughter Reconstruction
   (a) V0 Daughter Particle Cuts
      i. Cuts Common to Both Daughters
         A. $|\eta| < 0.8$
         B. SetTPCnclsDaughters(80)
         C. SetStatusDaughters(AliESDtrack::kTPCrefic)
         D. SetMaxDcaV0Daughters(0.4)
      ii. Pion Specific Daughter Cuts
         A. $p_T > 0.16$
         B. DCA to prim vertex > 0.3
      iii. Proton Specific Daughter Cuts
         A. $p_T > 0.5(p)$ $[0.3(\bar{p})]$ GeV/c
         B. DCA to prim vertex > 0.1
   (b) V0 Cuts
      i. $|\eta| < 0.8$
      ii. $p_T > 0.4$ GeV/c
      iii. $|m_{inv} - m_{PDG}| < 3.8$ MeV
      iv. DCA to prim. vertex > 0.2 cm
      v. Cosine of pointing angle to Ξ decay vertex > 0.9993

vi. OnFlyStatus = false
vii. Decay Length < 60 cm
viii. The misidentification cuts described in Section 3.3.1 are utilized

2. Bachelor π Cuts
   (a) $|\eta| < 0.8$
   (b) $p_T < 100$ GeV/c
   (c) DCA to prim vertex > 0.1 cm
   (d) SetTPCnclsDaughters(70)
   (e) SetStatusDaughters(AliESDtrack::kTPCrefic)

3. Ξ Cuts
   (a) $|\eta| < 0.8$
   (b) $0.8 < p_T < 100$ GeV/c
   (c) $|m_{inv} - m_{PDG}| < 3.0$ MeV
   (d) DCA to prim. vertex < 0.3 cm
   (e) Cosine of pointing angle > 0.9992

4. Shared Daughter Cut for Ξ Collection
   – Iterate through Ξ collection to ensure that no daughter is used in more than one Ξ candidate

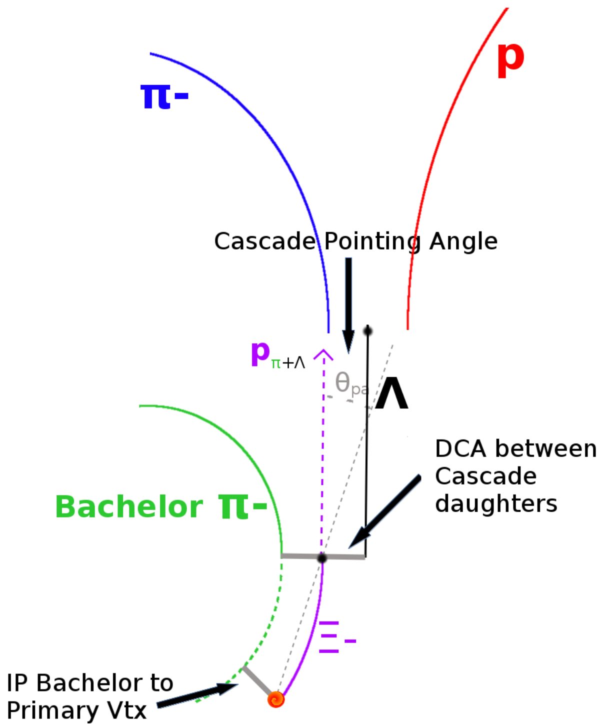

Fig. 6: Ξ Reconstruction

The purity of our Ξ and $\bar{\Xi}$ collections are calculated just as those of our V0 collections 3.3. Figure 7, which is used to calculate the purity, shows the m$_{inv}$ distribution of our $\Xi(\bar{\Xi})$ candidates just before the final m$_{inv}$ cut. Currently, we have Purity(Ξ^-) $\approx 90\%$ and Purity($\bar{\Xi}^+$) $\approx 92\%$.

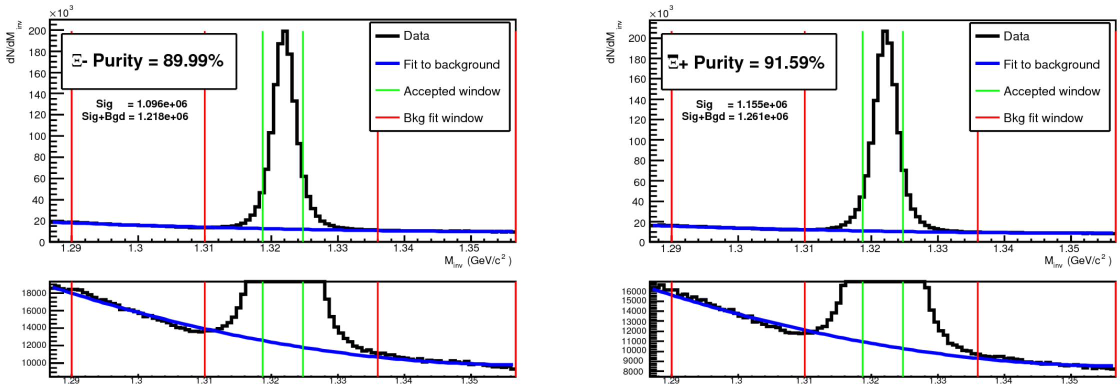

(a) Ξ^- Purity (b) $\bar{\Xi}$ Purity

Fig. 7: $\Xi^-(\bar{\Xi}^+)$ Purity 0-10%: Purity(Ξ^-) $\approx$ 90% and Purity($\bar{\Xi}^+$) $\approx$ 92%.

3.5 Pair Selection

It is important to obtain true particle pairs in the analysis. In particular, contamination from pairs constructed with split or merged tracks, and pairs sharing daughters, can introduce an artificial signal into the correlation function, obscuring the actual physics.

1. Shared Daughter Cut for Pairs
   (a) V0-V0 Pairs (i.e. $\Lambda(\bar{\Lambda})K^0_S$ analyses)
      - Remove all pairs which share a daughter
         - Ex. Λ and K^0_S particles which share a π^- daughter are not included

   (b) V0-Track Pairs (i.e. $\Lambda(\bar{\Lambda})K^\pm$ analyses)
      - Remove pairs if Track is also used as a daughter of the V0
         - In these analyses, this could only occur if, for instance, a K is misidentified as a π or p in the V0 reconstruction

   (c) Ξ-Track Pairs
      - Remove pairs if Track is also used as a daughter of the Ξ
         - In these analyses, this could only occur if, for instance, a K is misidentified as a π or p in the V0 reconstruction, or misidentified as bachelor π.
      - Remove pair if bachelor π is also a daughter of the Λ
         - This is not a pair cut, but is included here because this cut occurs in the AliFemtoXiTrackPairCut class

2. Average Separation Cuts
   - Used to cut out splitting and merging effects
   - The motivation for these cuts can be seen in Figures 8, 9, and 10, in which average separation correlation functions are presented

   (a) $\Lambda(\bar{\Lambda})K^0_S$ Analyses
      - Average separation $>$ 6.0 cm for like charge sign daughters
         - ex. p daughter of Λ and π^+ daughter of K^0_S
      - No cut for unlike-sign daughters

(b) $\Lambda(\bar{\Lambda})K^{\pm}$ Analyses

  - Average Separation > 8.0 cm for daughter of $\Lambda(\bar{\Lambda})$ sharing charge sign of $K^{\pm}$
    - ex. in ΛK^{+} analysis, p daughter of Λ with K^{+}
  - No cut for unlike signs

(c) $\Xi(\bar{\Xi})K^{\pm}$ Analyses

  - Average Separation > 8.0 cm for any daughter of Ξ sharing charge sign of $K^{\pm}$
    - ex. in $\Xi^{-}K^{-}$ analysis, π^{-} daughter of Λ daughter with K^{-}, and bachelor π^{-} daughter with K^{-}
  - No cut for unlike signs

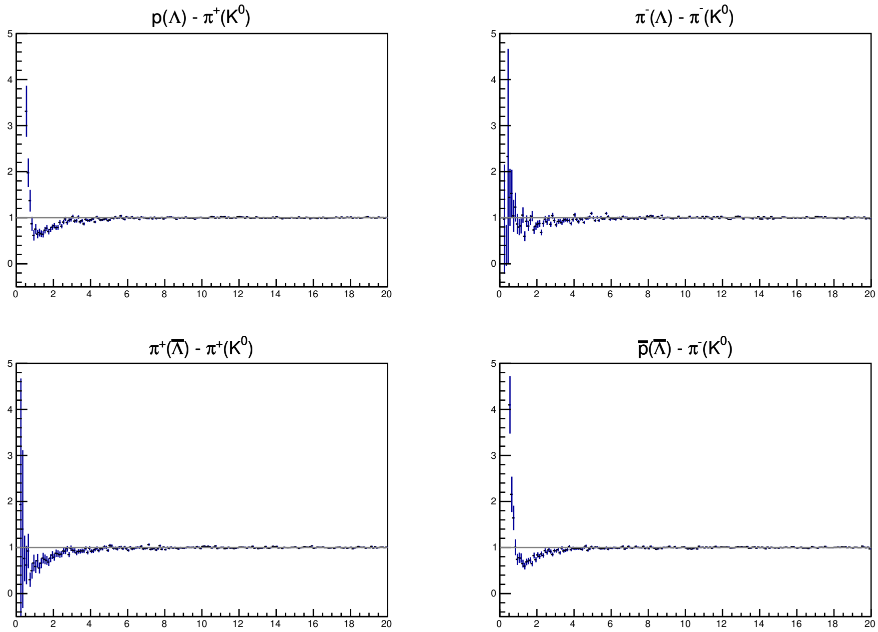

Fig. 8: Avgerage separation (cm) correlation functions of $\Lambda(\bar{\Lambda})$ and K^0_S Daughters. Only like-sign daughter pairs are shown (the distributions for unlike-signs were found to be flat). The title of each subfigure shows the daughter pair, as well as the mother of each daughter (in "()"), ex. top left is p from Λ with π^{+} from K^0_S.

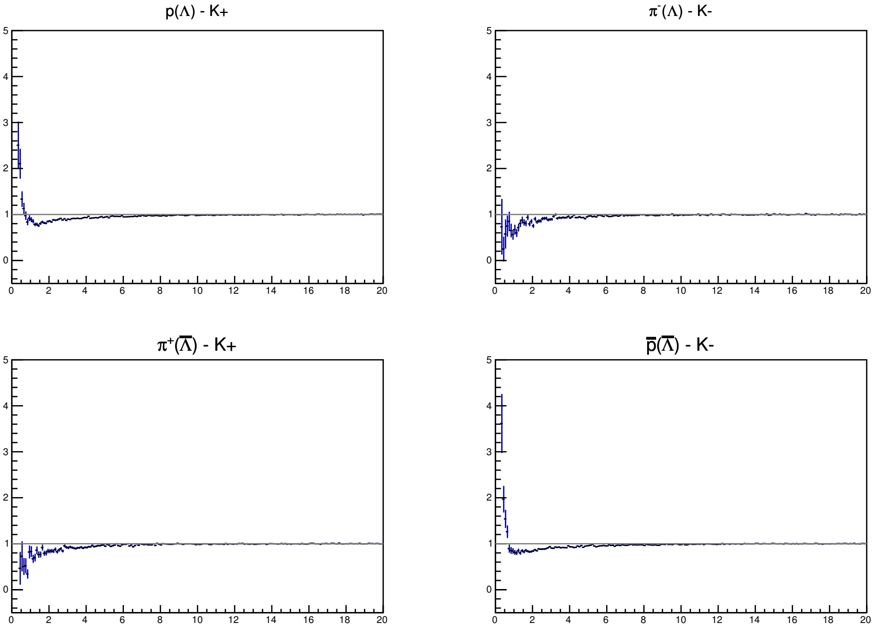

Fig. 9: Avgerage separation (cm) correlation functions of $\Lambda(\bar{\Lambda})$ Daughter and $K^{\pm}$. Only like-sign pairs are shown (unlike-signs were flat). In the subfigure titles, the particles in "()" represent the mothers, ex. top left is p from Λ with K^{+}.

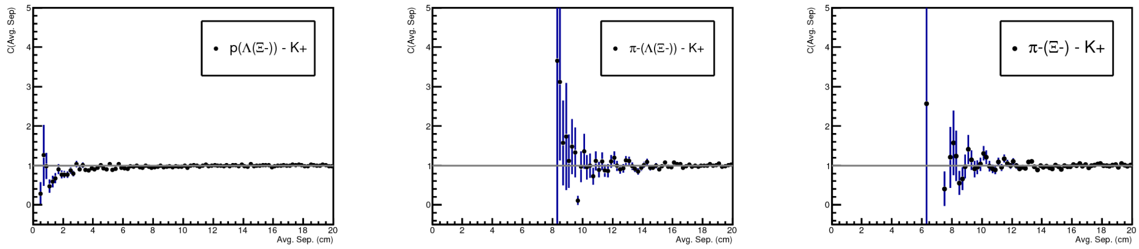

(a) $\Xi^{-}K^{+}$

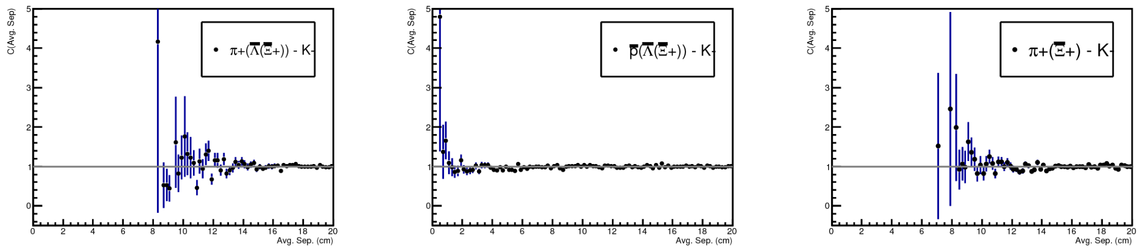

(b) $\bar{\Xi}^{+}K^{-}$

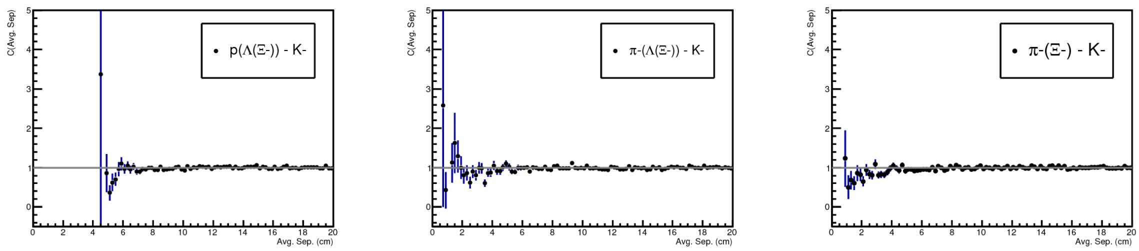

(c) $\Xi^{-}K^{-}$

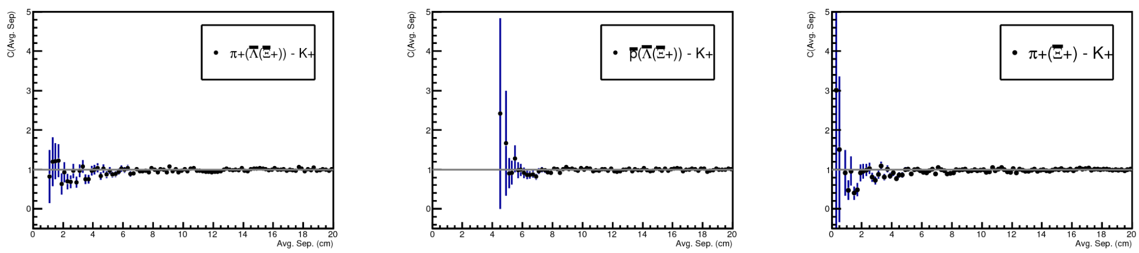

(d) $\bar{\Xi}^{+}K^{+}$

Fig. 10: Avgerage separation (cm) correlation functions of Ξ Daughter and $K^{\pm}$. In the subfigure titles, the particles in "()" represent the mothers, ex. top left is p from Λ from Ξ^{-} with K^{+}.

4 Correlation Functions

This analysis studies the momentum correlations of both Λ-K and Ξ-K pairs using the two-particle correlation function, defined as $C(k^*) = A(k^*)/B(k^*)$, where $A(k^*)$ is the signal distribution, $B(k^*)$ is the reference (or background) distribution, and k^* is the momentum of one of the particles in the pair rest frame. In practice, $A(k^*)$ is constructed by binning in k^* pairs from the same event. Ideally, $B(k^*)$ is similar to $A(k^*)$ in all respects excluding the presence of femtoscopic correlations [2]; as such, $B(k^*)$ is used to divide out the phase-space effects, leaving only the femtoscopic effects in the correlation function.

In practice, $B(k^*)$ is obtained by forming mixed-event pairs, i.e. particles from a given event are paired with particles from N_{mix}(= 5) other events, and these pairs are then binned in k^*. In forming the background distribution, it is important to mix only similar events; mixing events with different phase-spaces can lead to artificial signals in the correlaton function. Therefore, in this analysis, we mix events with primary vertices within 2 cm and centralities within 5% of each other. Also note, a vertex correction is also applied to each event, which essentially recenters the the primary vertices to z = 0.

This analysis presents correlation functions for three centrality bins (0-10%, 10-30%, and 30-50%), and is currently pair transverse momentum ($k_T = 0.5|\mathbf{p}_{T,1} + \mathbf{p}_{T,2}|$) integrated (i.e. not binned in k_T). The correlation functions are constructed separately for the two magnetic field configurations, and are combined using a weighted average:

$$C_{combined}(k^*) = \frac{\sum\limits_i w_i C_i(k^*)}{\sum\limits_i w_i} \tag{3}$$

where the sum runs over the correlation functions to be combined, and the weight, w_i, is the number of numerator pairs in $C_i(k^*)$. Here, the sum is over the two field configurations.

Figures 11, 12, and 13 show the correlation functions for all centalities studied for $\Lambda K^0_S(\bar{\Lambda}K^0_S)$, $\Lambda K^+(\bar{\Lambda}K^-)$, and $\Lambda K^-(\bar{\Lambda}K^+)$, respectively. All were normalized in the range $0.32 < k^* < 0.4$ GeV/c.

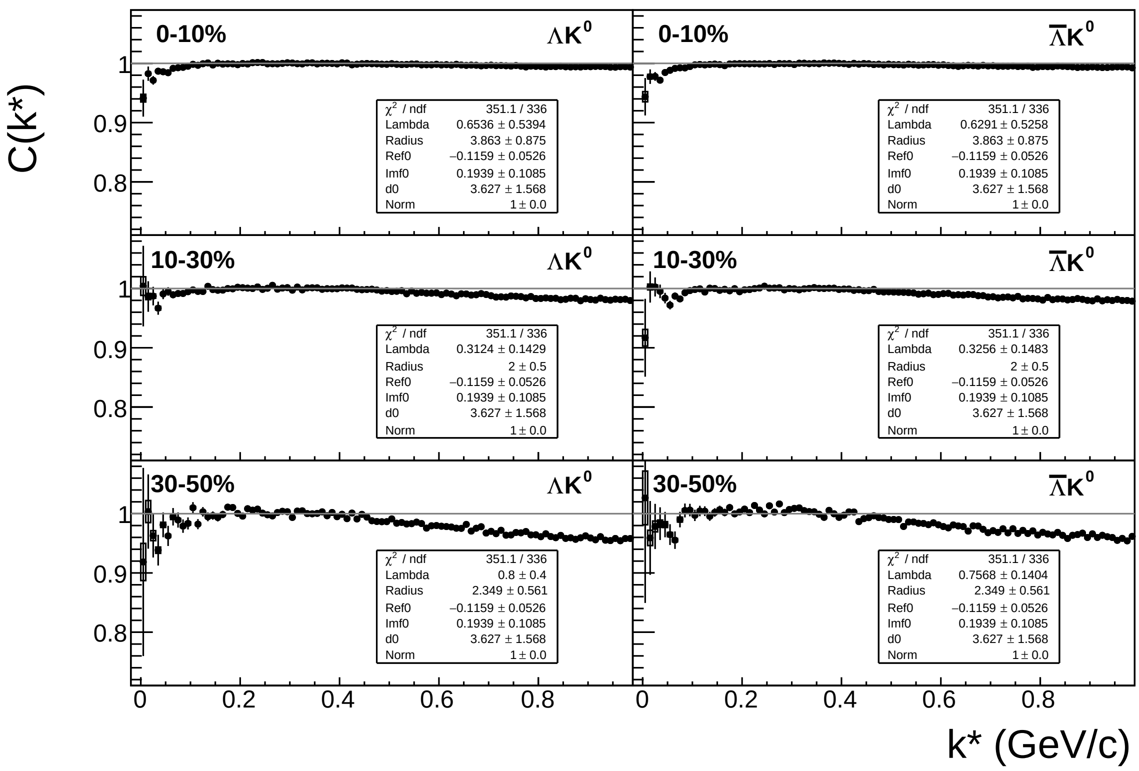

Fig. 11: ΛK^0_S (left) and $\bar{\Lambda}K^0_S$ (right) correlation functions for 0-10% (top), 10-30%(middle), and 30-50%(bottom) centralities. The lines represent the statistical errors, while the boxes represent the systematic errors.

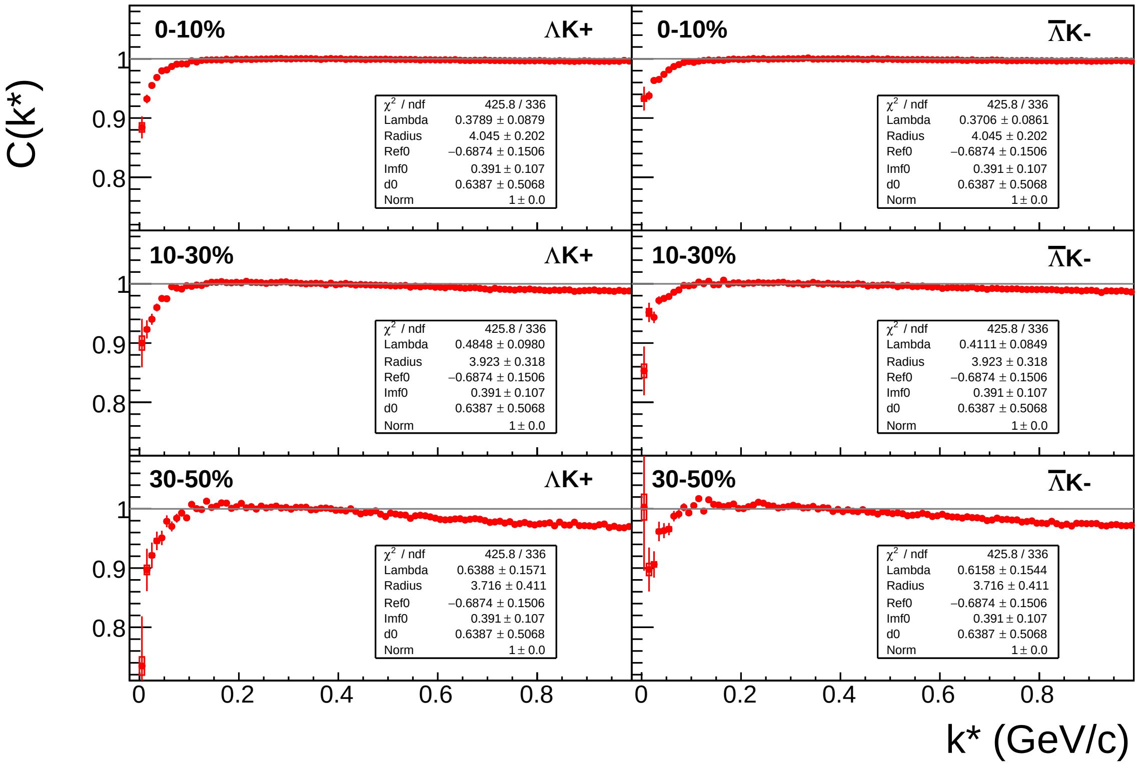

Fig. 12: ΛK^+ (left) and $\bar{\Lambda}K^-$ (right) correlation functions for 0-10% (top), 10-30%(middle), and 30-50%(bottom) centralities. The lines represent the statistical errors, while the boxes represent the systematic errors.

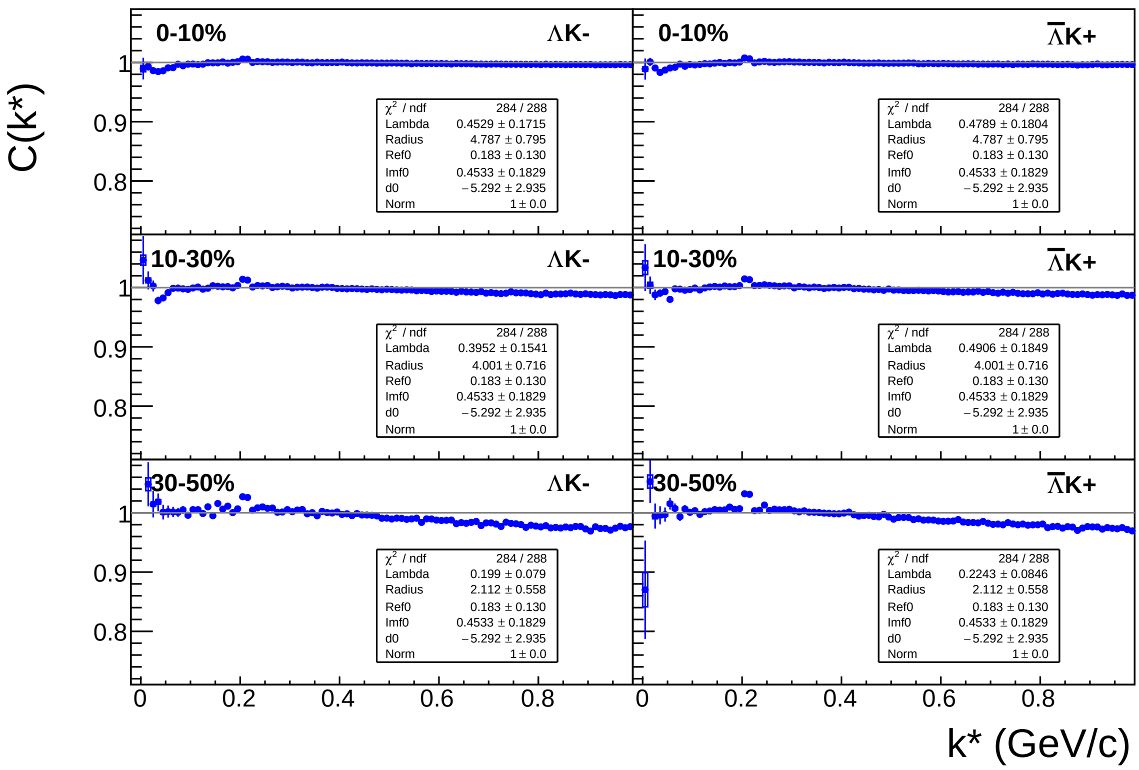

Fig. 13: ΛK^- (left) and $\bar{\Lambda}K^+$ (right) correlation functions for 0-10% (top), 10-30%(middle), and 30-50%(bottom) centralities. The lines represent the statistical errors, while the boxes represent the systematic errors. The peak at k* ≈ 0.2 GeV/c is due to the Ω^- resonance.

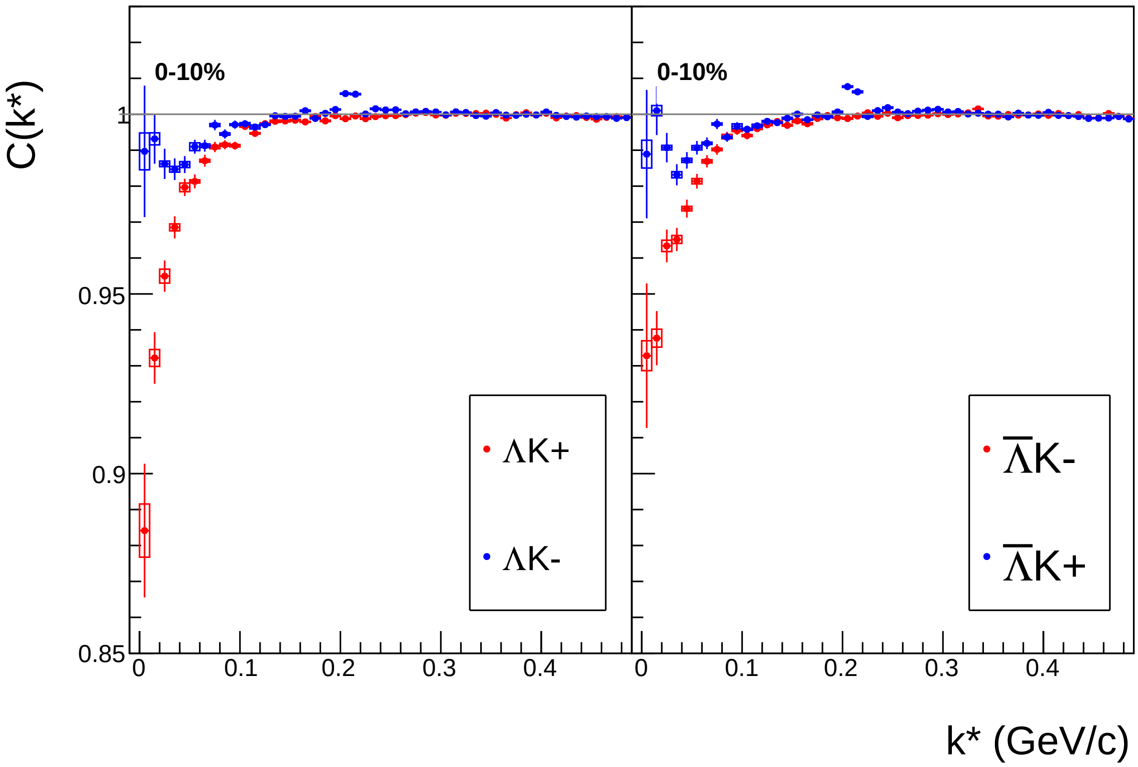

Fig. 14: Correlation Functions: ΛK^+ vs ΛK^- ($\bar{\Lambda}K^+$ vs $\bar{\Lambda}K^-$) for 0-10% centrality. The peak in ΛK^-($\bar{\Lambda}K^+$) at k* $\approx$ 0.2 GeV/c is due to the Ω^- resonance. The lines represent the statistical errors. (NOTE: This figure is slightly dated, and a new one will be generated which includes both statistical and systematic uncertainties)

5 Fitting

5.1 Model: ΛK^0_S, $\Lambda K^{\pm}$, $\Xi^{ch} K^0_S$

The two-particle relative momentum correlation function may be written theoretically by the Koonin-Pratt equation [3, 4]:

$$C(\mathbf{k}^*) = \int S(\mathbf{r}^*)|\Psi_{\mathbf{k}^*}(\mathbf{r}^*)|^2 d^3\mathbf{r}^* \tag{4}$$

In the absence of Coulomb effects, and assuming a spherically gaussian source of width R, the 1D femtoscopic correlation function can be calculated analytically using:

$$C(k^*) = 1 + \lambda[C_{QI}(k^*) + C_{FSI}(k^*)] \tag{5}$$

C_{QI} describes plane-wave quantum interference:

$$C_{QI}(k^*) = \alpha \exp(-4k^{*2}R^2) \tag{6}$$

where $\alpha = (-1)^{2j}/(2j+1)$ for identical particles with spin j, and $\alpha = 0$ for non-identical particles. Obviously, $\alpha = 0$ for all analyses presented in this note. C_{FSI} describes the s-wave strong final state interaction between the particles:

$$\begin{aligned} C_{FSI}(k^*) &= (1+\alpha)[\tfrac{1}{2}|\tfrac{f(k^*)}{R}|^2(1-\tfrac{d_0}{2\sqrt{\pi}R}) + \tfrac{2\mathbb{R}f(k^*)}{\sqrt{\pi}R}F_1(2k^*R) - \tfrac{\mathbb{I}f(k^*)}{R}F_2(2k^*R)] \\ f(k^*) &= (\tfrac{1}{f_0} + \tfrac{1}{2}d_0 k^{*2} - ik^*)^{-1}; \quad F_1(z) = \int_0^z \tfrac{e^{x^2-z^2}}{z}dx; \quad F_2(z) = \tfrac{1-e^{-z^2}}{z} \end{aligned} \tag{7}$$

where R is the source size, $f(k^*)$ is the s-wave scattering amplitude, f_0 is the complex scattering length, and d_0 is the effective range of the interaction.

5.2 Model: $\Xi^{ch} K^{ch}$

The two-particle correlation function may be written as:

$$C(\mathbf{k}^*) = \sum_S \rho_S \int S(\mathbf{r}^*)|\Psi^S_{\mathbf{k}^*}(\mathbf{r}^*)|^2 d^3\mathbf{r}^* \tag{8}$$

where ρ_S is the normalized emission probability of particles in a state with spin S, $S(\mathbf{r}^*)$ is the pair emission source distribution (assumed to be Gaussian), and $\Psi^S_{\mathbf{k}^*}(\mathbf{r}^*)$ is the two-particle wave-function including both strong and Coulomb interactions [5]:

$$\Psi_{\mathbf{k}^*}(\mathbf{r}^*) = e^{i\delta_c}\sqrt{A_c(\eta)}[e^{i\mathbf{k}^*\cdot\mathbf{r}^*}F(-i\eta,1,i\xi) + f_c(k^*)\frac{\tilde{G}(\rho,\eta)}{r^*}] \tag{9}$$

where $\rho = k^*r^*$, $\eta = (k^*a_c)^{-1}$, $\xi = \mathbf{k}^*\cdot\mathbf{r}^* + k^*r^* \equiv \rho(1+\cos\theta^*)$, and $a_c = (\mu z_1 z_2 e^2)^{-1}$ is the two-particle Bohr radius (including the sign of the interaction). δ_c is the Coulomb s-wave phase shift, $A_c(\eta)$ is the Coulomb penetration factor, $\tilde{G} = \sqrt{A_c}(G_0 + iF_0)$ is a combination of the regular (F_0) and singular (G_0) s-wave Coulomb functions. $f_c(k^*)$ is the s-wave scattering amplitude:

$$f_c(k^*) = [\frac{1}{f_0} + \frac{1}{2}d_0k^{*2} - \frac{2}{a_c}h(\eta) - ik^*A_c(\eta)]^{-1} \tag{10}$$

where, the "h-function", $h(\eta)$, is expressed through the digamma function, $\psi(z) = \Gamma'(z)/\Gamma(z)$ as:

$$h(\eta) = 0.5[\psi(i\eta) + \psi(-i\eta) - \ln(\eta^2)] \tag{11}$$

5.3 Momentum Resolution Corrections

Finite track momentum resolution causes the reconstructed momentum of a particle to smear around the true value. This, of course, also holds true for V0 particles. The effect is propagated up to the pairs of interest, which causes the reconstructed relative momentum (k^*_{Rec}) to differ from the true momentum (k^*_{True}). Smearing of the momentum typically will result in a suppression of the signal.

The effect of finite momentum resolution can be investigated using the MC data, for which both the true and reconstructed momenta are available. Figure 15 shows sample k^*_{True} vs. k^*_{Rec} plots for $\Lambda(\bar{\Lambda})K^{\pm}$ 0-10% analyses; Figure 15a was generated using same-event pairs, while Figure 15b was generated using mixed-event pairs (with $N_{mix} = 5$).

If there are no contaminations in our particle collection, the plots in Figure 15 should be smeared around $k^*_{True} = k^*_{Rec}$; this is mostly true in our analyses. However, there are some interesting features of our results which demonstrate a small (notice the log-scale on the z-axis) contamination in our particle collection. The structure around $k^*_{Rec} = k^*_{True} - 0.15$ is mainly caused by K^0_S contamination in our $\Lambda(\bar{\Lambda})$ sample. The remaining structure not distributed about $k^*_{Rec} = k^*_{True}$ is due to π and e contamination in our $K^{\pm}$ sample. These contaminations are more visible in Figure 16, which show k^*_{Rec} vs. k^*_{True} plots (for a small sample of the ΛK^+ 0-10% central analysis), for which the MC truth (i.e. true, known identity of the particle) was used to eliminate misidentified particles in the K^+(a) and Λ(b) collections. (NOTE: This is an old figure and is for a small sample of the data. A new version will be generated shortly. It, nonetheless, demonstrates the point well).

Information gained from looking at k^*_{Rec} vs k^*_{True} can be used to apply corrections to account for the effects of finite momentum resolution on the correlation functions. A typical method involves using the MC HIJING data to build two correlation functions, $C_{Rec}(k^*)$ and $C_{True}(k^*)$, using the generator-level momentum (k^*_{True}) and the measured detector-level momentum (k^*_{Rec}). The data is then corrected by multiplying by the ratio, C_{True}/C_{Rec}, before fitting. This essentially unsmears the data, which that can be compared directly to theoretical predictions and fits. Although this is conceptually simple, there are a couple of big disadvantages to this method. First, HIJING does not incorporate final-state interactions, so weights must be used when building same-event (numerator) distributions. These weights account for the interactions, and, in the absence of Coulomb interactions, can be calculated using Eq. 5. Of course, these weights are valid only for a particular set of fit parameters. Therefore, in the fitting process, during which the fitter explores a large parameter set, the corrections will not remain valid. As such, applying the momentum resolution correction and fitting becomes a long and drawn out iterative process. An ititial parameter set is obtained (through fitting without momentum resolution corrections, theoretical models, or a good guess), then the MC data is run over to obtain the correction factor, the data is fit using the correction factor, a refined parameter set is extracted, the MC data is run over again to obtain the new correction factor, etc. This process continues until the parameter set stabilizes. The second issue concerns statistics. With the MC data available on the grid, we were not able to generate the statistics necessary to use the raw C_{True}/C_{Rec} ratio. The ratio was not stable, and when applied to the data, obscured the signal. Attempting to fit the ratioto use to generate the corrections also proved problematic. However, as HIJING does not include final-state interactions, the same-event and mixed-event pairs are very similiar (with the exception of things like energy and momentum conservation, etc). Therefore, one may build the numerator distribution using mixed-event pairs. This corresponds, more or less, to simply running a the weight generator through the detector framework.

A second approach is to use information gained from plots like those in Figure 15, which can be considered response matrices. The reponse matrix describes quantitatively how each k^*_{Rec} bin receives contributions from multiple k^*_{True} bins, and can be used to account for the effects of finite momentum resolution. With this approach, the resolution correction is applied on-the-fly during the fitting process by propagating the theoretical (fit) correlation function through the response matrix, according to:

$$C_{fit}(k^*_{Rec}) = \frac{\sum\limits_{k^*_{True}} M_{k^*_{Rec},k^*_{True}} C_{fit}(k^*_{True})}{\sum\limits_{k^*_{True}} M_{k^*_{Rec},k^*_{True}}} \tag{12}$$

where $M_{k^*_{Rec},k^*_{True}}$ is the response matrix (Figure 15), $C_{fit}(k^*_{True})$ is the fit binned in k^*_{True}, and the denominator normalizes the result.

Equation 12 describes that, for a given k^*_{Rec} bin, the observed value of $C(k^*_{Rec})$ is a weighted average of all $C(k^*_{True})$ values, where the weights are the normalized number of counts in the [k^*_{Rec}, k^*_{True}] bin. As seen in Figure 15, overwhelmingly the main contributions comes from the k^*_{Rec} = k^*_{True} bins. Although the correction is small, it is non-negligible for the low-k* region of the correlation function.

Here, the momentum resolution correction is applied to the fit, not the data. In other words, during fitting, the theoretical correlation function is smeared just as real data would be, instead of unsmearing the data. This may not be ideal for the theorist attempting to compare a model to experimental data, but it leaves the experimental data unadulterated. The current analyses use this second approach to applying momentum resolution corrections because of two major advantages. First, the MC data must be analyzed only once, and no assumptions about the fit are needed. Secondly, the momentum resolution correction is applied on-the-fly by the fitter, delegating the iterative process to a computer instead of the user.

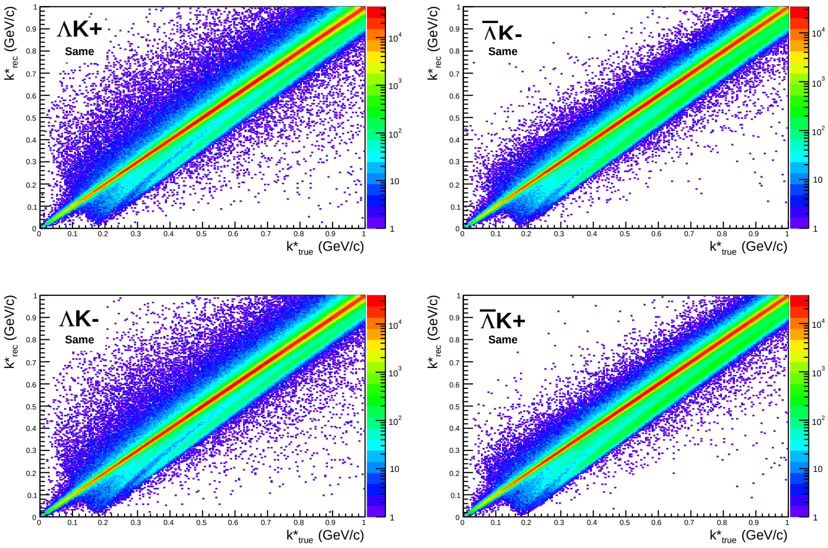

(a) Same Event Pairs ($\Lambda(\bar{\Lambda})$K$^{\pm}$, 0-10% Centrality)

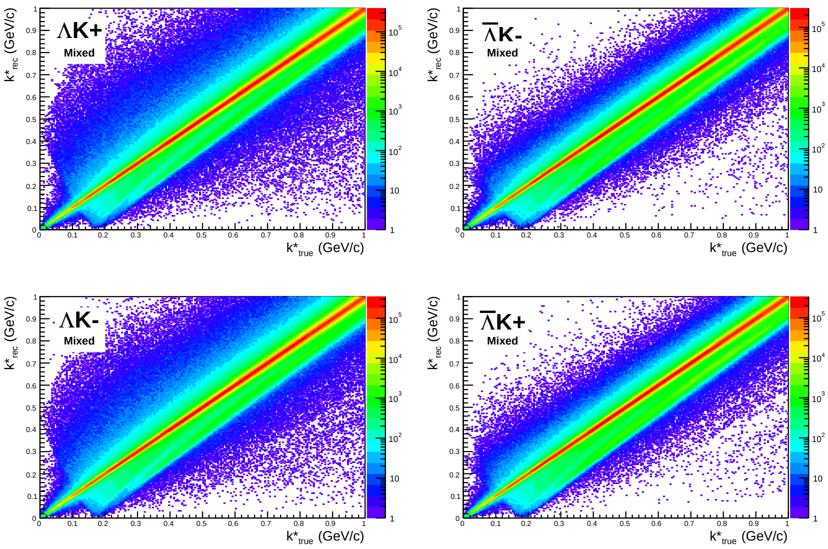

(b) Mixed Event Pairs ($\Lambda(\bar{\Lambda})$K$^{\pm}$, 0-10% Centrality)

Fig. 15: Sample k^*_{True} vs. k^*_{Rec} plot for $\Lambda(\bar{\Lambda})$K$^{\pm}$ 0-10% analyses. The structure which appears around $k^*_{Rec} = k^*_{True} - 0.15$ is mainly caused by K^0_S contamination in our $\Lambda(\bar{\Lambda})$ sample. The remaining structure not distributed about $k^*_{Rec} = k^*_{True}$ is due to π and e contamination in our K$^{\pm}$ sample. These contaminations are more clearly visible in Figure 16

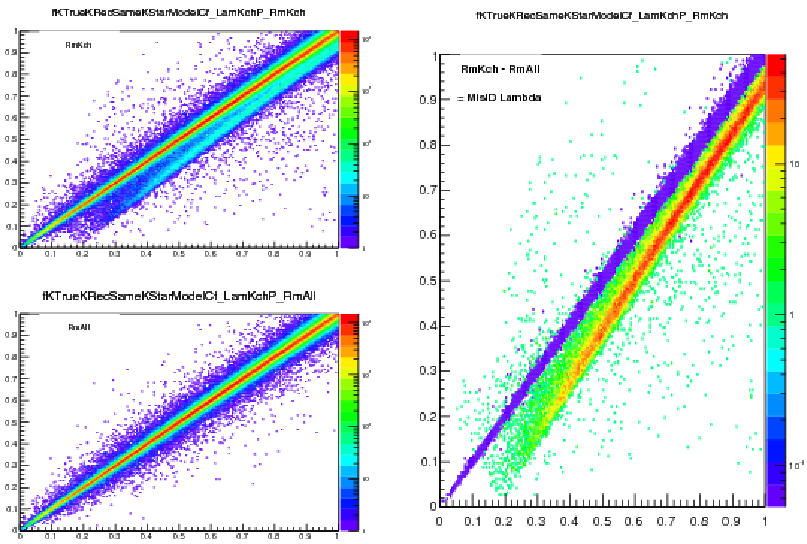

(a) (Top Left) All misidentified K^+ excluded. (Bottom Left) All misidentified Λ and K^+ excluded. (Right) The difference of (Top Left) - (Bottom Left), which reveals the contamination in our Λ collection. The structure which appears around $k^*_{Rec} = k^*_{True} - 0.15$ is mainly caused by K^0_S contamination in our $\Lambda(\bar{\Lambda})$ sample.

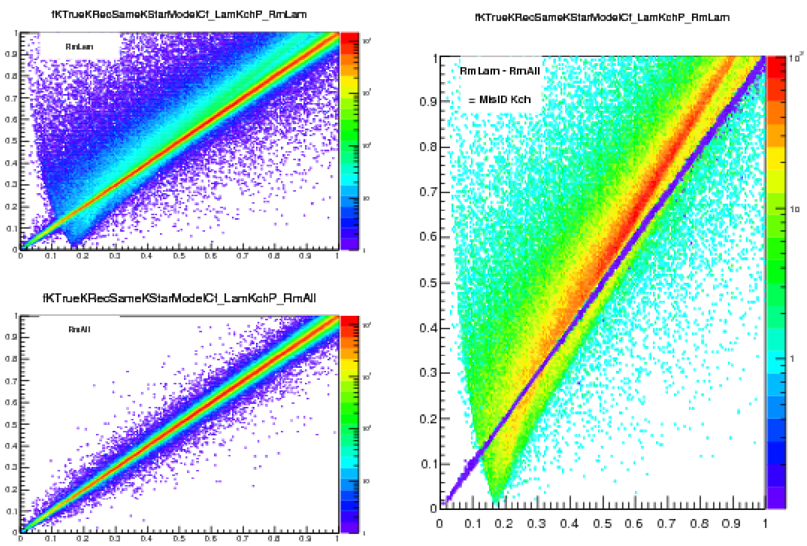

(b) (Top Left) All misidentified Λ excluded. (Bottom Left) All misidentified Λ and K^+ excluded. (Right) The difference of (Top Left) - (Bottom Left), which reveals the contamination in our K^+ collection. The structure not distributed about $k^*_{Rec} = k^*_{True}$ is due to π and e contamination in our K^+ sample.

Fig. 16: Note: This is an old figure and is for a small sample of the data. A new version will be generated shortly. y-axis = k^*_{Rec}, x-axis = k^*_{True}.
(Left) k^*_{Rec} vs. k^*_{True} plots for a small sample of the ΛK^+ 0-10% central analysis, MC truth was used to eliminate misidentified particles in the K^+(a) and Λ(b) collections. (Right) The difference of the top left and bottom left plots. Contaminations in our particle collections are clearly visible. Figure (a) demonstrates a K^0_S contamination in our Λ collection; Figure (b) demonstrates a π and e^- contamination in our $K^\pm$ collection.

5.4 Residual Correlations

The purpose of this analysis is study the interaction and scale of the emitting source of the pairs. In order to obtain correct results, it is important for our particle collections to consist of primary particles. In practice, this is difficult to achieve for our Λ and $\bar{\Lambda}$ collections. Many of our Λ particles are not primary, but originate as decay products from other hyperons, including Σ^0, Ξ^0, Ξ^- and $\Sigma^{*(+,-,0)}(1385)$. Additionally, many of our K particles are not primary, but decay from $K^{*(+,-,0)}(892)$ parents. In these decays, the Λ carries away a momentum very similar to that of its parent. As a result, the correlation function between a secondary Λ and, for instance, a K^+ will be sensitive to, and dependent upon, the interaction between the parent of the Λ and the K^+. In effect, the correlation between the parent of the Λ and the K^+ (ex. Σ^0K^+) will be visible, although smeared out, in the ΛK^+ data. We call this a residual correlation resulting from feed-down. Residual correlations are important in an analysis when three criteria are met [6]: i) the parent correlation signal is large, ii) a large fraction of pairs in the sample originate from the particular parent system, and iii) the decay momenta are comparable to the expected correlation width in $k*$.

As it is difficult for us to eliminate these residual correlations in our analyses, we must attempt to account for them in our fitter. To achieve this, we will simultaneously fit the data for both the primary correlation function and the residual correlations. For example, in the simple case of a ΛK^+ analysis with residuals arising solely from Σ^0K^+ feed-down:

$$
\begin{aligned}
C_{measured}(k^*_{\Lambda K^+}) &= 1+\lambda_{\Lambda K^+}[C_{\Lambda K^+}(k^*_{\Lambda K^+})-1]+\lambda_{\Sigma^0K^+}[C_{\Sigma^0K^+}(k^*_{\Lambda K^+})-1] \\
C_{\Sigma^0K^+}(k^*_{\Lambda K^+}) &\equiv \frac{\sum\limits_{k^*_{\Sigma^0K^+}} C_{\Sigma^0K^+}\left(k^*_{\Sigma^0K^+}\right)T\left(k^*_{\Sigma^0K^+},k^*_{\Lambda K^+}\right)}{\sum\limits_{k^*_{\Sigma^0K^+}} T\left(k^*_{\Sigma^0K^+},k^*_{\Lambda K^+}\right)}
\end{aligned}
\tag{13}
$$

$C_{\Sigma^0K^+}(k^*_{\Sigma^0K^+})$ is the Σ^0K^+ correlation function from, for instance, Equation 5, and T is the transform matrix generated with THERMINATOR. The transform matrix is formed for a given parent pair, AB, by taking all ΛK pairs originating from AB, calculating the relative momentum of the parents ($k*_{AB}$) and daughters ($k*_{\Lambda K}$), and filling a two-dimensional histogram with the values. The transform matrix is essentially an unnormalized probability distribution mapping the $k*$ of the parent pair to that of the daughter pair when one or both parents decay. An example of such transform matrices can be found in Figures 17 and 18.

The above equation can be easily extended to include feed-down from more sources:

$$
\begin{aligned}
C_{measured}(k^*_{\Lambda K}) &= 1+\lambda_{\Lambda K}[C_{\Lambda K}(k^*_{\Lambda K})-1]+\lambda_{\Sigma^0K}[C_{\Sigma^0K}(k^*_{\Lambda K})-1]+\ldots \\
&\quad +\lambda_{P_1P_2}[C_{P_1P_2}(k^*_{\Lambda K})-1]+\lambda_{other}[C_{other}(k^*_{\Lambda K})-1] \\
C_{P_1P_2}(k^*_{\Lambda K}) &\equiv \frac{\sum\limits_{k^*_{P_1P_2}} C_{P_1P_2}\left(k^*_{P_1P_2}\right)T\left(k^*_{P_1P_2},k^*_{\Lambda K}\right)}{\sum\limits_{k^*_{P_1P_2}} T\left(k^*_{P_1P_2},k^*_{\Lambda K}\right)}
\end{aligned}
\tag{14}
$$

Or, more compactly:

$$
C_{measured}(k^*_{\Lambda K}) = 1+\sum_i \lambda_i[C_i(k^*_{\Lambda K})-1] \tag{15}
$$

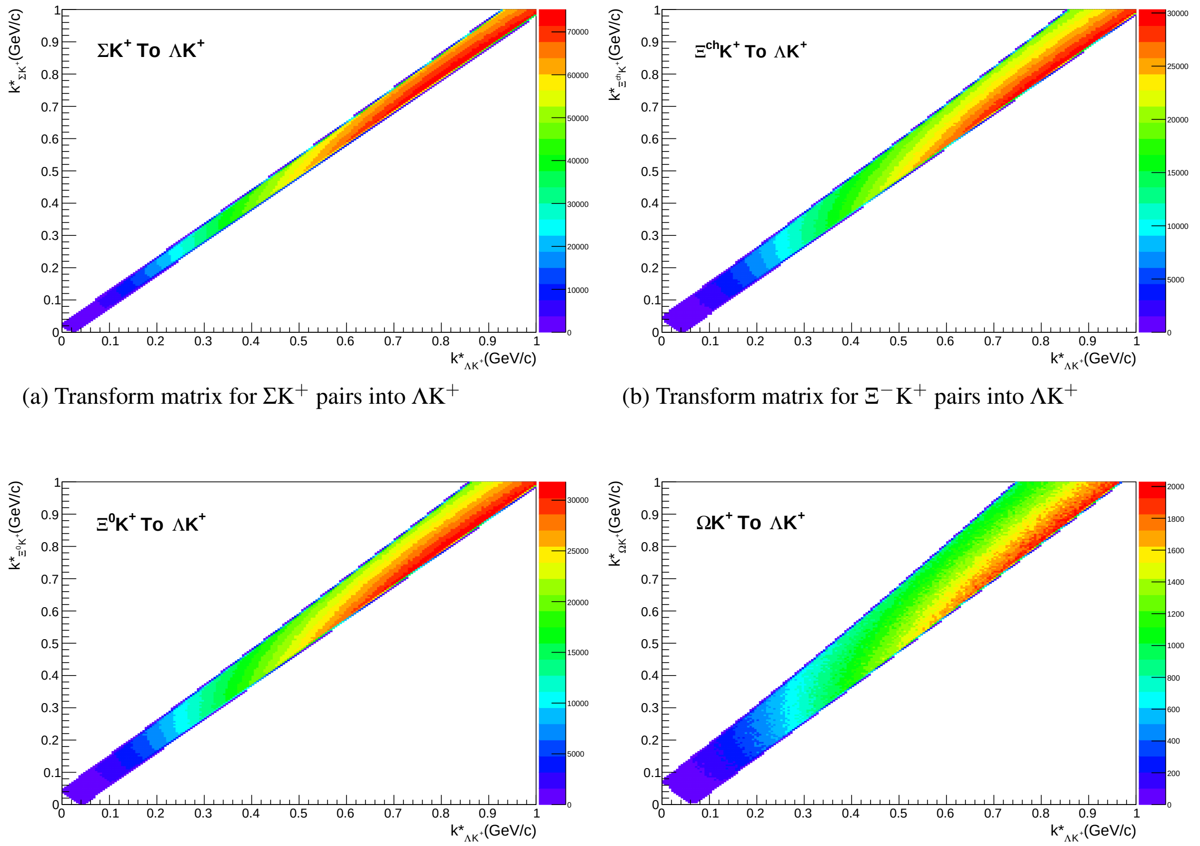

(a) Transform matrix for ΣK^+ pairs into ΛK^+

(b) Transform matrix for $\Xi^- K^+$ pairs into ΛK^+

(c) Transform matrix for $\Xi^0 K^+$ pairs into ΛK^+

(d) Transform matrix for $\Omega^- K^+$ pairs into ΛK^+

Fig. 17: Transform Matrices generated with THERMINATOR for ΛK^+ Analysis

So, in practice, we model the correlation function of the parents, and run the correlation function through the appropriate transform matrix to determine the contribution to the daughter correlation function. A few questions still remain. First, what λ values should be used in the above equation? One option would be to leave all of these λ-parameters free during the fit process. However, this would introduce a huge number of new parameters into the fitter, and would make the fit results less trustworthy. The λ parameters roughly dictate the strength of the parent contribution to the daughter pair. Additionally, as found in [7], the reconstruction efficiency for primary Λ particles is nearly equal to that of Λ particles originating from Σ, Σ^*, Ξ^0, Ξ^-, and Ω hyperons. Therefore, the λ parameter for parent system AB can be estimated using THERMINATOR as the total number of ΛK pairs originating from AB (N_{AB}) divided by the total number of ΛK pairs (N_{Total}):

$$\lambda_{AB} = \frac{N_{AB}}{N_{Total}} \tag{16}$$

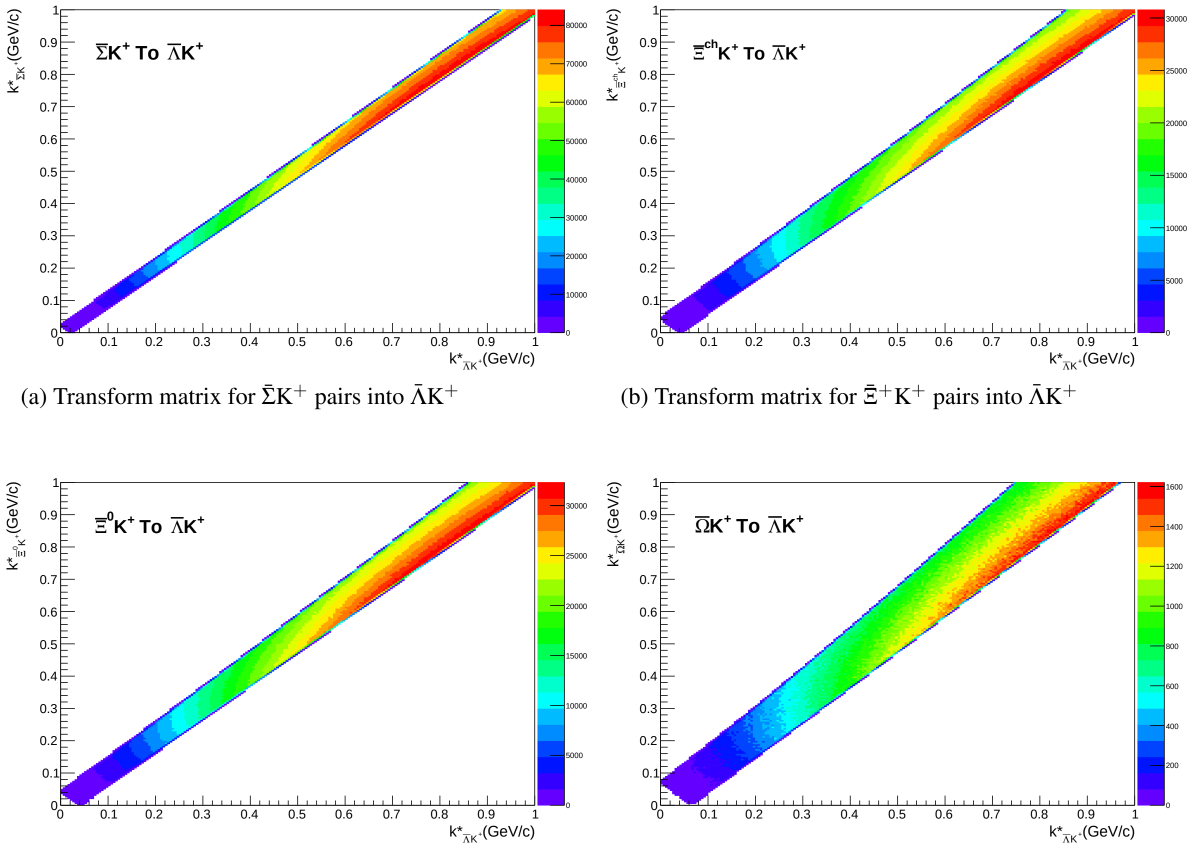

(a) Transform matrix for $\bar{\Sigma}K^+$ pairs into $\bar{\Lambda}K^+$

(b) Transform matrix for $\bar{\Xi}^+K^+$ pairs into $\bar{\Lambda}K^+$

(c) Transform matrix for $\bar{\Xi}^0K^+$ pairs into $\bar{\Lambda}K^+$

(d) Transform matrix for $\bar{\Omega}^+K^+$ pairs into $\bar{\Lambda}K^+$

Fig. 18: Transform Matrices generated with THERMINATOR for $\bar{\Lambda}K^+$ Analysis

ΛK^+ Residuals

Pair System	λ value
ΛK^+	0.154
$\Sigma^0 K^+$	0.099
$\Xi^0 K^+$	0.072
$\Xi^- K^+$	0.069
Other	0.558
Fakes	0.048

$\bar{\Lambda} K^-$ Residuals

Pair System	λ value
$\bar{\Lambda} K^-$	0.158
$\bar{\Sigma}^0 K^-$	0.102
$\bar{\Xi}^0 K^-$	0.067
$\bar{\Xi}^+ K^-$	0.065
Other	0.560
Fakes	0.048

Table 1: λ values for the individual components of the ΛK^+ (left) and $\bar{\Lambda} K^-$ (right) correlation functions for the case of 3 residual contributions.

ΛK^+ Residuals

Pair System	λ value
ΛK^+	0.154
$\Sigma^0 K^+$	0.099
$\Xi^0 K^+$	0.072
$\Xi^- K^+$	0.069
$\Sigma^{*+} K^+$	0.046
$\Sigma^{*-} K^+$	0.042
$\Sigma^{*0} K^+$	0.042
ΛK^{*0}	0.039
$\Sigma^0 K^{*0}$	0.035
$\Xi^0 K^{*0}$	0.025
$\Xi^- K^{*0}$	0.024
Other	0.305
Fakes	0.048

$\bar{\Lambda} K^-$ Residuals

Pair System	λ value
$\bar{\Lambda} K^-$	0.158
$\bar{\Sigma}^0 K^-$	0.102
$\bar{\Xi}^0 K^-$	0.067
$\bar{\Xi}^+ K^-$	0.065
$\bar{\Sigma}^{*-} K^-$	0.046
$\bar{\Sigma}^{*+} K^-$	0.045
$\bar{\Sigma}^{*0} K^-$	0.040
$\bar{\Lambda} \bar{K}^{*0}$	0.041
$\bar{\Sigma}^0 \bar{K}^{*0}$	0.036
$\bar{\Xi}^0 \bar{K}^{*0}$	0.024
$\bar{\Xi}^+ \bar{K}^{*0}$	0.023
Other	0.305
Fakes	0.048

Table 2: λ values for the individual components of the ΛK^+ (left) and $\bar{\Lambda} K^-$ (right) correlation functions for the case of 10 residual contributions.

ΛK^- Residuals

Pair System	**λ value**
ΛK^-	0.154
$\Sigma^0 K^-$	0.099
$\Xi^0 K^-$	0.071
$\Xi^- K^-$	0.068
Other	0.561
Fakes	0.048

$\bar{\Lambda} K^+$ Residuals

Pair System	**λ value**
$\bar{\Lambda} K^+$	0.158
$\bar{\Sigma}^0 K^+$	0.103
$\bar{\Xi}^0 K^+$	0.068
$\bar{\Xi}^+ K^+$	0.066
Other	0.557
Fakes	0.048

Table 3: λ values for the individual components of the ΛK^- (left) and $\bar{\Lambda} K^+$ (right) correlation functions for the case of 3 residual contributions.

ΛK^- Residuals

Pair System	**λ value**
ΛK^-	0.154
$\Sigma^0 K^-$	0.099
$\Xi^0 K^-$	0.071
$\Xi^- K^-$	0.068
$\Sigma^{*+} K^-$	0.046
$\Sigma^{*-} K^-$	0.041
$\Sigma^{*0} K^-$	0.041
$\Lambda \bar{K}^{*0}$	0.039
$\Sigma^0 \bar{K}^{*0}$	0.035
$\Xi^0 \bar{K}^{*0}$	0.025
$\Xi^- \bar{K}^{*0}$	0.024
Other	0.308
Fakes	0.048

$\bar{\Lambda} K^+$ Residuals

Pair System	**λ value**
$\bar{\Lambda} K^+$	0.158
$\bar{\Sigma}^0 K^+$	0.103
$\bar{\Xi}^0 K^+$	0.068
$\bar{\Xi}^+ K^+$	0.066
$\bar{\Sigma}^{*-} K^+$	0.046
$\bar{\Sigma}^{*+} K^+$	0.045
$\bar{\Sigma}^{*0} K^+$	0.041
$\bar{\Lambda} K^{*0}$	0.041
$\bar{\Sigma}^0 K^{*0}$	0.036
$\bar{\Xi}^0 K^{*0}$	0.024
$\bar{\Xi}^+ K^{*0}$	0.023
Other	0.301
Fakes	0.048

Table 4: λ values for the individual components of the ΛK^- (left) and $\bar{\Lambda} K^+$ (right) correlation functions for the case of 10 residual contributions.

ΛK^0_S Residuals

Pair System	λ value
ΛK^0_S	0.165
$\Sigma^0 K^0_S$	0.107
$\Xi^0 K^0_S$	0.077
$\Xi^- K^0_S$	0.075
Other	0.528
Fakes	0.048

$\bar{\Lambda} K^0_S$ Residuals

Pair System	λ value
$\bar{\Lambda} K^0_S$	0.169
$\bar{\Sigma}^0 K^0_S$	0.111
$\bar{\Xi}^0 K^0_S$	0.073
$\bar{\Xi}^+ K^0_S$	0.071
Other	0.528
Fakes	0.048

Table 5: λ values for the individual components of the ΛK^0_S (left) and $\bar{\Lambda} K^0_S$ (right) correlation functions for the case of 3 residual contributions.

ΛK^0_S Residuals

Pair System	λ value
ΛK^0_S	0.165
$\Sigma^0 K^0_S$	0.107
$\Xi^0 K^0_S$	0.077
$\Xi^- K^0_S$	0.075
$\Sigma^{*+} K^0_S$	0.050
$\Sigma^{*-} K^0_S$	0.045
$\Sigma^{*0} K^0_S$	0.045
ΛK^{*0}	0.019
$\Sigma^0 K^{*0}$	0.017
$\Xi^0 K^{*0}$	0.012
$\Xi^- K^{*0}$	0.012
Other	0.329
Fakes	0.048

$\bar{\Lambda} K^0_S$ Residuals

Pair System	λ value
$\bar{\Lambda} K^0_S$	0.169
$\bar{\Sigma}^0 K^0_S$	0.111
$\bar{\Xi}^0 K^0_S$	0.073
$\bar{\Xi}^+ K^0_S$	0.071
$\bar{\Sigma}^{*-} K^0_S$	0.050
$\bar{\Sigma}^{*+} K^0_S$	0.049
$\bar{\Sigma}^{*0} K^0_S$	0.044
$\bar{\Lambda} K^{*0}$	0.020
$\bar{\Sigma}^0 K^{*0}$	0.017
$\bar{\Xi}^0 K^{*0}$	0.011
$\bar{\Xi}^+ K^{*0}$	0.011
Other	0.326
Fakes	0.048

Table 6: λ values for the individual components of the ΛK^0_S (left) and $\bar{\Lambda} K^0_S$ (right) correlation functions for the case of 10 residual contributions.

Now, the remaining question is how do we model the parent correlation functions? In an ideal world, we would simply look up the parent interaction in some table, and input this into our Lednicky equation (for the case of one or more charge neutral particle in the pair), or run it through the CoulombFitter machinery described in Sec. 5.2. Unfortunately, the world in which we live is not perfect, such a table does not exists, and little is know about the interaction between the residual pairs in this study. One solution would be to introduce a set of scattering parameters and radii for each residual system. However, as will the case of the λ-parameters above, this would introduce a large number of additional fit parameters, and would make our fitter too unconstrained and would yield untrustworthy results. The second option, which is adopted in this analysis, is to assume all residual pairs have the same source size as the daughter pair, and all Coulomb-neutral residual pairs also share the same scattering parameters as the daughter pair (the case of charged pairs will be described below).

Concerning the radii of the residual parent pairs, it was suggested that these should be set to smaller values. In the interest of minimizing the number of parameters in the fitter, we tested this by introducing an m_{T}-scaling of the parent radii. The motivation for this scaling comes from the approximate m_{T}-scaling of the radii observed in 39. To achieve this scaling, we assume the radii follow an inverse-square-root distribution: $R_{AB} = \alpha m_{\mathrm{T}}^{-1/2}$. Then, it follows that we should scale the parent radii as:

$$R_{AB} = R_{\Lambda K} \left(\frac{m_{\mathrm{T},AB}}{m_{\mathrm{T},\Lambda K}} \right)^{-1/2} \tag{17}$$

The values for m_{T} for each pair system was taken from THERMINATOR. As the fitter dances around parameter space and selects new radii for the ΛK pairs, the radii of the residuals is scaled by the above factor. In the end, this scaling factor made no significant difference in our fit results, so this complication is excluded from our final results. Note that this is not surprising, as the most extreme scaling factor was, in the case of using 10 residual systems, between ΛK+ with $m_{\mathrm{T},\Lambda K+} \approx 1.4$ GeV/c^2 and $\Xi^-\mathrm{K}^{*0}$ with $m_{\mathrm{T},\Xi^- K^{*0}} \approx 1.8$ GeV/c^2, resulting in a scale factor of ≈ 0.9.

Now, as hinted above, accounting for charged residuals adds a complication in that they necessitate the inclusion of the CoulombFitter into the process. The complication of combining the two fitters is not troubling, but it increases the fitting time drastically (the parallelization of the CoulombFitter across a large number of GPU cores, to drastically decrease run-time, is currently underway). We have two solutions to bypass such a large increase in run time. First, we can use our experimental $\Xi^{\mathrm{ch}}\mathrm{K}^{\mathrm{ch}}$ data to represent all charged parent pair system. In this case, there is no need to make any assumption about scattering parameters or source sizes, as we already have the experimental data. The downside is that, especially in the 30-50% centrality bin, the error bars on the data are large. Alternatively, we can assume the strong interaction is negligible in the charged residual, and generate the parent correlation function given radius and λ parameters. We find in our $\Xi^{\mathrm{ch}}\mathrm{K}^{\mathrm{ch}}$ study that a Coulomb-only description of the system describes, reasonably well, the broad features of the correlation. The strong interaction is necessary for the fine details. However, as these correlations are run through a transform matrix, which largely flattens out and fine details, a Coulomb-only description should be sufficient. In practice, this Coulomb-only scenario is achieved by first building a large number of Coulomb-only correlations for various radii and λ parameter values, and interpolating from this grid during the fitting process. We find consistent results between using the ΞK data and the Coulomb-only interpolation method. When the number of residual pairs used is increased to 10, so that pairs such as $\Sigma^{*+}\mathrm{K}^-$ enter the picture, the Coulomb-only interpolation method is used. In other words, the ΞK experimental data is only used to model the ΞK residual contribution, all other charged pairs are treated with the Coulomb-only interpolation method.

Two examples of how very different transform matrices can alter a correlation function are shown in Figures 19 and 20 below. These figures were taken using parameter values obtained from fits to the data. In the top left corner of the figures, the input correlation function (closed symbols) is shown together with the output, transformed, correlation function (open symbols). In the bottom left, the transformed correlation is shown by itself. This is especially helpful when the λ parameter is very small, in which case the contribution in the top left can look flat, but the zoomed in view in the bottom left shows the structure. The right two plots in each figure show the transform matrix without (top right) and with (bottom right) a log-scale on the z-axis. Note, more examples of these transforms can be found in Sec. 9.

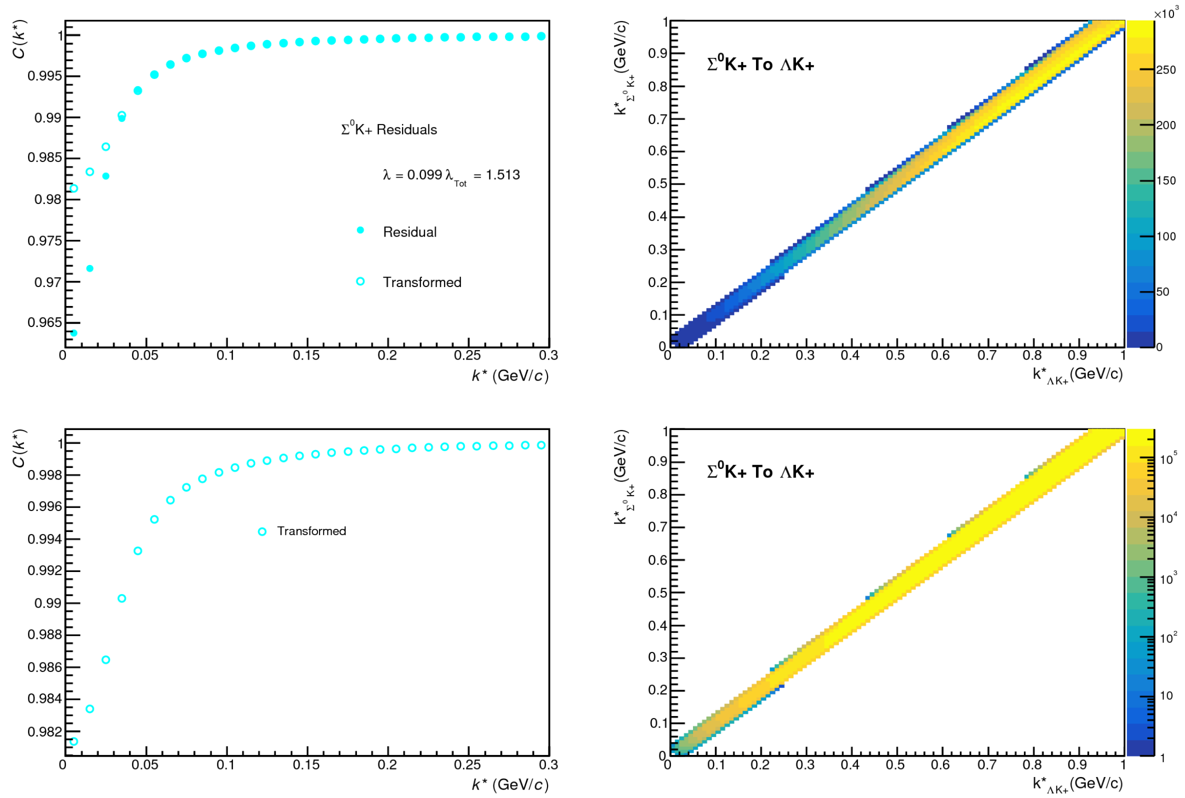

Fig. 19: Σ^0K$^+$ Transform. These figures were taken using parameter values obtained from fits to the data. In the top left corner of the figures, the input correlation function (closed symbols) is shown together with the output, transformed, correlation function (open symbols). In the bottom left, the transformed correlation is shown by itself. The right two plots in each figure show the transform matrix without (top right) and with (bottom right) a log-scale on the z-axis.

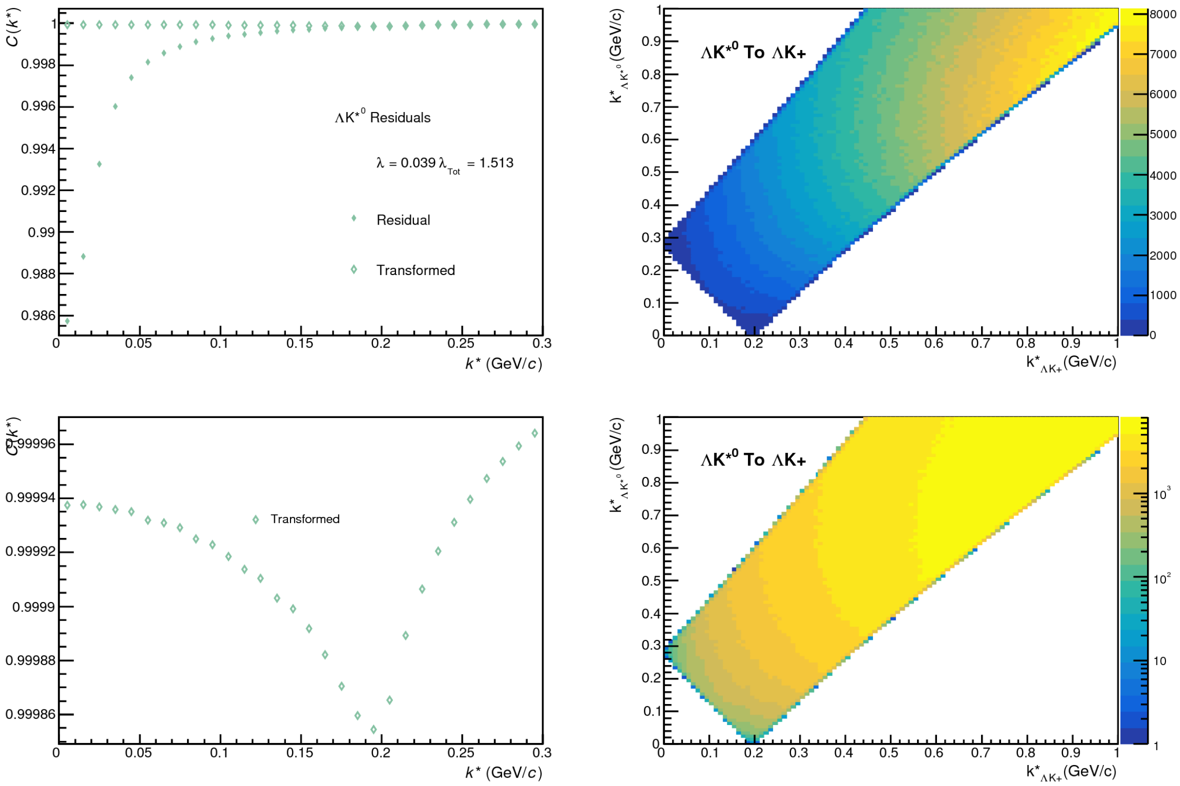

Fig. 20: Σ^0K^+ Transform. These figures were taken using parameter values obtained from fits to the data. In the top left corner of the figures, the input correlation function (closed symbols) is shown together with the output, transformed, correlation function (open symbols). In the bottom left, the transformed correlation is shown by itself. The right two plots in each figure show the transform matrix without (top right) and with (bottom right) a log-scale on the z-axis.

5.5 Non-Flat Background

Non-flat background

5.6 LednickyFitter

The code developed to fit the data is called "LednickyFitter", and utilizes the ROOT TMinuit implementation of the MINUIT fitting package. In short, given a function with a number of parameters, the fitter explores the parameter space searching for the minimum of the equation. In this implementation, the function to be minimized should represent the difference between the measure and theoretical correlation functions. However, a simple χ^2 test in inappropriate for fitting correlation functions, as the ratio two Poisson distributions does not result in a Poisson distribution. Instead, a log-likelihood fit function of the following form is used [2]:

$$\chi^2_{PML} = -2\left[A\ln\left(\frac{C(A+B)}{A(C+1)}\right) + B\ln\left(\frac{A+B}{B(C+1)}\right)\right] \tag{18}$$

where A is the experimental signal distribution (numerator), B is the experimental background distribution (denominator), and C is the theoretical fit correlation function.

The LednickyFitter uses Equations 5 – 7 to build the theoretical fit, and Equation 18 as the statistic quantifying the quality of the fit. The parameters to be varied by MINUIT are: λ, R, f_0 ($\mathbb{R}f_0$ and $\mathbb{I}f_0$ separately), d_0, and normalization N. The fitter currently includes methods to correct for momentum resolution and a non-flat background. These corrections are applied to the fit function, the data is never touched. The fitter is able to share parameters between different analyses and fit all simultaneously.

In a typical fit, a given pair is fit with its conjugate (ex. ΛK^+ with $\bar{\Lambda}K^-$) across all centralities (0-10%, 10-30%, 30-50%), for a total of 6 simultaneous analyses. Each analysis has a unique λ and normalization parameter. The radii are shared between analyses of like centrality, as these should have similar source sizes. The scattering parameters ($\mathbb{R}f_0$, $\mathbb{I}f_0$, d_0) are shared amongst all.

Figures 25, 27, and 29 (32, 33, and 34, or 36, 37, and 38), in Section 7, show experimental data with fits for all studied centralities for ΛK^0_S with $\bar{\Lambda}K^0_S$, ΛK^+ with $\bar{\Lambda}K^-$, and ΛK^- with $\bar{\Lambda}K^+$, respectively. In the figures, the black solid line represents the "raw" fit, i.e. not corrected for momentum resolution effects nor non-flat background. The green line shows the fit to the non-flat background. The purple points show the fit after momentum resolution, non-flat background, and residual correlations (if applicable) corrections have been applied. The initial values of the parameters is listed, as well as the final fit values with uncertainties.

5.7 Coulomg Fitter

When fitting the $\Xi^-(\bar{\Xi}^+)K^\pm$ results, it is necessary to include both strong and Coulomb effects. In this case, Equation 5 is no longer valid, and, in fact, there is no analytical form with which to fit. Therefore, we must begin with the wave function describing the pair interaction, and simulate many particle pairs to obtain a theoretical fit correlation function. The code developed to achieve this functionality is called "CoulombFitter". Currently, in order to generate the statistics needed for a stable fit, we find that $\sim 10^4$ simulated pairs per 10 MeV bin are necessary. Unfortunately, the nature of this process means that the "CoulombFitter" takes much longer to run than the "LednickyFitter" of Section 5.1.

Unfortunately, with this analysis, we are not sensitive to, and therefore not able to distinguish between, the iso-spin singlet and triplet states. We proceed with our analysis, but the results must be interpreted as iso-spin averaged scattering parameters.

As stated before, to generate a fit correlation function, we must simulate a large number of pairs, calculate the wave-function, and average Ψ^2 over all pairs in a given k* bin. Essentially, we calculate Equation 8 by hand:

$$\begin{aligned}
&C(\mathbf{k}^*) = \sum_S \rho_S \int S(\mathbf{r}^*)|\Psi^S_{\mathbf{k}^*}(\mathbf{r}^*)|^2 d^3\mathbf{r}^* \\
&\longrightarrow C(|\mathbf{k}^*|) \equiv C(k^*) = \sum_S \rho_S \langle|\Psi^S(\mathbf{k}^*_\mathbf{i}, \mathbf{r}^*_\mathbf{i})|^2\rangle_i \\
&\longrightarrow C(k^*) = \lambda \sum_S \rho_S \langle|\Psi^S(\mathbf{k}^*_\mathbf{i}, \mathbf{r}^*_\mathbf{i})|^2\rangle_i + (1-\lambda)
\end{aligned} \tag{19}$$

where $\langle\rangle_i$ represents an average over all pairs in a given k* bin.

In summary, for a given k* bin, we must draw $N_{pairs} \sim 10^4$ pairs, and for each pair:

1. Draw a random $\mathbf{r}^*$ vector according to our Gaussian source distribution $S(\mathbf{r}^*)$
2. Draw a random $\mathbf{k}^*$ vector satisfying the $|\mathbf{k}^*|$ restriction of the bin
   - We draw from real k^* vectors obtained from the data
   - However, we find that drawing from a distribution flat in k^* gives similar results
3. Construct the wave-function Ψ

After all pairs for a given k* bin are simulated and wave-functions obtained, the results are averaged to give the fit result.

Construction of the wave-functions, Equation 9, involves a number of complex functions not included in standard C++ or ROOT libraries (namely, $h(\eta)$, $\tilde{G}(\rho,\eta)$), and $F(-i\eta,1,i\xi)$. These functions were even difficult to find and implement from elsewhere. Our solution was to embed a Mathematica kernel into our C++ code to evaluate these functions. However, having Mathematica work on-the-fly with the fitter was far too time consuming (fitter would have taken day, maybe weeks to finish). Our solution was to use Mathematica to create matrices representing these functions for different parameter values. During fitting, these matrices were then interpolated and the results used to build the wave-functions. This method decreased the running time dramatically, and we are not able to generate results in under $\sim$ 1 hour. This process will be explained in more detail in future versions of the note.

6 Systematic Errors

In order to understand my systematic uncertainties, the analysis code was run many times using slightly different values for a number of important cuts, and the results were compared.

In order to quantify the systematic errors on the data, all correlation functions built using all varied cut values were bin-by-bin averaged, and the resulting variance of each bin was taken as the systematic error. The cuts which were utilized in this study are presented in Sections 6.1.1 (ΛK^0_S) and 6.2.1 ($\Lambda K^\pm$).

Similarly, the fit parameters extracted from all of these correlation functions were averaged, and the resulting variances were taken as the systematic errors for the fit parameters. As with the systematic errors on the data, this was performed for all varied cut values. Additionally, a systematic analysis was done on our fit method (which, for now, just includes our choice of fit range). These two sources of uncertainty were combined in quadrature to obtain the final systematic uncertainties on the extracted fit parameters.

6.1 Systematic Errors: ΛK^0_S

6.1.1 Particle and Pair Cuts

The cuts included in the systematic study, as well as the values used in the variations, are listed below. Note, the central value corresponds to that used in the analysis.

1. DCA $\Lambda(\bar{\Lambda})$: {4, 5, 6 mm}
2. DCA K^0_S: {2, 3, 4 mm}
3. DCA $\Lambda(\bar{\Lambda})$ Daughters: {3, 4, 5 mm}
4. DCA K^0_S Daughters: {2, 3, 4 mm}
5. $\Lambda(\bar{\Lambda})$ Cosine of Pointing Angle: {0.9992, 0.9993, 0.9994}
6. K^0_S Cosine of Pointing Angle: {0.9992, 0.9993, 0.9994}
7. DCA to Primary Vertex of $p(\bar{p})$ Daughter of $\Lambda(\bar{\Lambda})$: {0.5, 1, 2 mm}
8. DCA to Primary Vertex of $\pi^-(\pi^+)$ Daughter of $\Lambda(\bar{\Lambda})$: {2, 3, 4 mm}
9. DCA to Primary Vertex of π^+ Daughter of K^0_S: {2, 3, 4 mm}
10. DCA to Primary Vertex of π^- Daughter of K^0_S: {2, 3, 4 mm}
11. Average Separation of Like-Charge Daughters: {5, 6, 7 cm}

6.1.2 Non-Flat Background

We fit our non-flat background with a linear function. To study the contribution of this choice to our systematic errors, we also fit with a quadratic and Gaussian form. The resulting uncertainties are combined with the uncertainties arising from our particle cuts.

6.1.3 Fit Range

Our choice of k^* fit range was varied by $\pm$ 25%. The resulting uncertainties in the extracted parameter sets were combined with our uncertainties arising from our particle and pair cuts.

6.2 Systematic Errors: $\Lambda K^\pm$

6.2.1 Particle and Pair Cuts

The cuts included in the systematic study, as well as the values used in the variations, are listed below. Note, the central value corresponds to that used in the analysis.

1. DCA $\Lambda(\bar{\Lambda})$: {4, 5, 6 mm}
2. DCA $\Lambda(\bar{\Lambda})$ Daughters: {3, 4, 5 mm}
3. $\Lambda(\bar{\Lambda})$ Cosine of Pointing Angle: {0.9992, 0.9993, 0.9994}
4. DCA to Primary Vertex of $p(\bar{p})$ Daughter of $\Lambda(\bar{\Lambda})$: {0.5, 1, 2 mm}
5. DCA to Primary Vertex of $\pi^-(\pi^+)$ Daughter of $\Lambda(\bar{\Lambda})$: {2, 3, 4 mm}
6. Average Separation of $\Lambda(\bar{\Lambda})$ Daughter with Same Charge as $K^\pm$: {7, 8, 9 cm}
7. Max. DCA to Primary Vertex in Transverse Plane of $K^\pm$: {1.92, 2.4, 2.88}
8. Max. DCA to Primary Vertex in Longitudinal Direction of $K^\pm$: {2.4, 3.0, 3.6}

6.2.2 Non-Flat Background

We fit our non-flat background with a linear function. To study the contribution of this choice to our systematic errors, we also fit with a quadratic and Gaussian form. The resulting uncertainties are combined with the uncertainties arising from our particle cuts.

6.2.3 Fit Range

Our choice of k^* fit range was varied by $\pm$ 25%. The resulting uncertainties in the extracted parameter sets were combined with our uncertainties arising from our particle and pair cuts.

6.3 Systematic Errors: ΞK$^{\pm}$

6.3.1 Particle and Pair Cuts

The cuts included in the systematic study, as well as the values used in the variations, are listed below. Note, the central value corresponds to that used in the analysis.

1. Max. DCA $\Xi(\bar{\Xi})$: {2, 3, 4 mm}
2. Max. DCA $\Xi(\bar{\Xi})$ Daughters: {2, 3, 4 mm}
3. Min. $\Xi(\bar{\Xi})$ Cosine of Pointing Angle to Primary Vertex: {0.9991, 0.9992, 0.9993}
4. Min. $\Lambda(\bar{\Lambda})$ Cosine of Pointing Angle to $\Xi(\bar{\Xi})$ Decay Vertex: {0.9992, 0.9993, 0.9994}
5. Min. DCA Bachelor π: {0.5, 1, 2 mm}
6. Min. DCA $\Lambda(\bar{\Lambda})$: {1, 2, 3 mm}
7. Max. DCA $\Lambda(\bar{\Lambda})$ Daughters: {3, 4, 5 mm}
8. Min. DCA to Primary Vertex of $p(\bar{p})$ Daughter of $\Lambda(\bar{\Lambda})$: {0.5, 1, 2 mm}
9. Min. DCA to Primary Vertex of $\pi^-(\pi^+)$ Daughter of $\Lambda(\bar{\Lambda})$: {2, 3, 4 mm}
10. Min. Average Separation of $\Lambda(\bar{\Lambda})$ Daughter and K$^{\pm}$ with like charge: {7, 8, 9 cm}
11. Min. Average Separation of Bachelor π and K$^{\pm}$ with like charge: {7, 8, 9 cm}
12. Max. DCA to Primary Vertex in Transverse Plane of K$^{\pm}$: {1.92, 2.4, 2.88}
13. Max. DCA to Primary Vertex in Longitudinal Direction of K$^{\pm}$: {2.4, 3.0, 3.6}

7 Results and Discussion

7.1 Results: ΛK^0_S and ΛK$^{\pm}$

I first collect all of the summary results, and will show the actual fits to the data in Sections 7.1.1, 7.1.2, and 7.1.3. In the first of the summary plots, we show the extracted scattering parameters in the form of a Im[f_0] vs Re[f_0] plot, which includes the d_0 values to the right side. The next three summary plots show the λ vs. Radius parameters. The first group of plots shows: 1) results without any residual correlations included in the fit (marked as ”QM 2017”), 2) results with 10 residual pairs included, and 3) results with 3 residual pairs included. The second group of plots also includes the case where we fixed the d_0 parameter to zero.

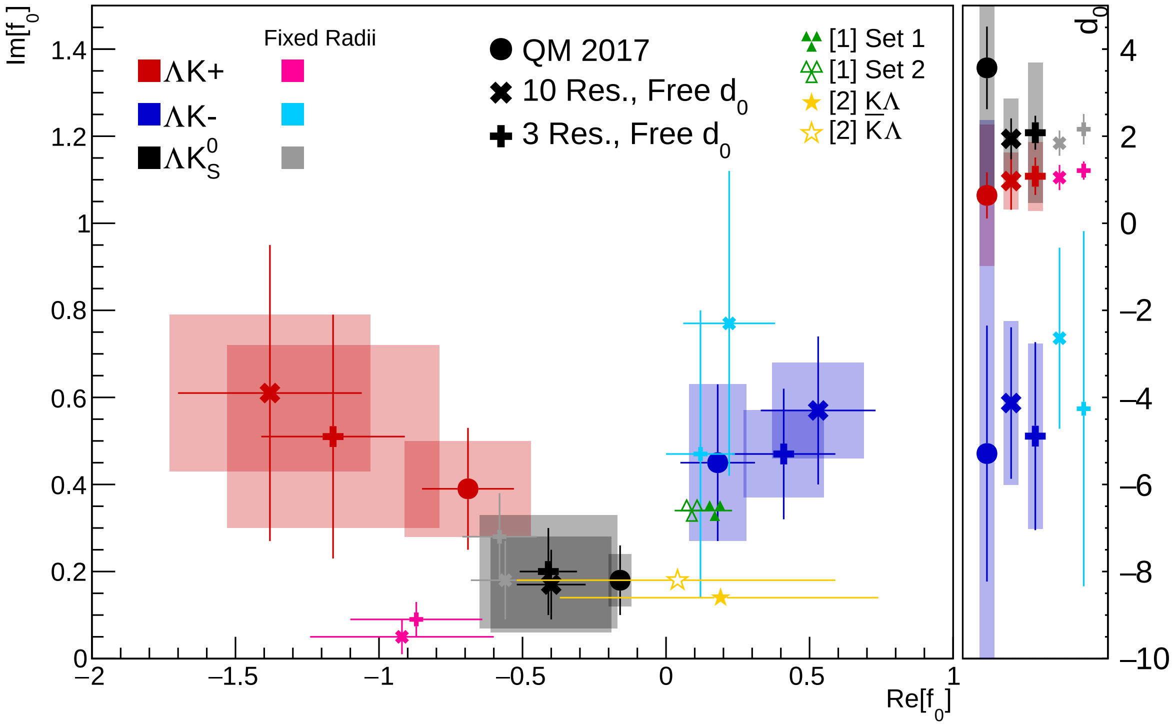

Fig. 21: Extracted scattering parameter results, Im[f_0] vs. Re[f_0], together with d_0 to the right, for all of our ΛK systems. The plot shows results including no residuals (circles), 10 residual pairs (X), and 3 residual pairs (+). The lighter color markers (pink, sky blue, gray) show the extracted parameters when we fix the radii to roughly align with the m_T-scaling plot, Fig. 31. The green [8] and yellow [9] points show theoretical predictions made using chiral perturbation theory. Note, ΛK^+ on the plot is shorthand for ΛK^+ and $\bar{\Lambda} K^-$, and similar for the others.

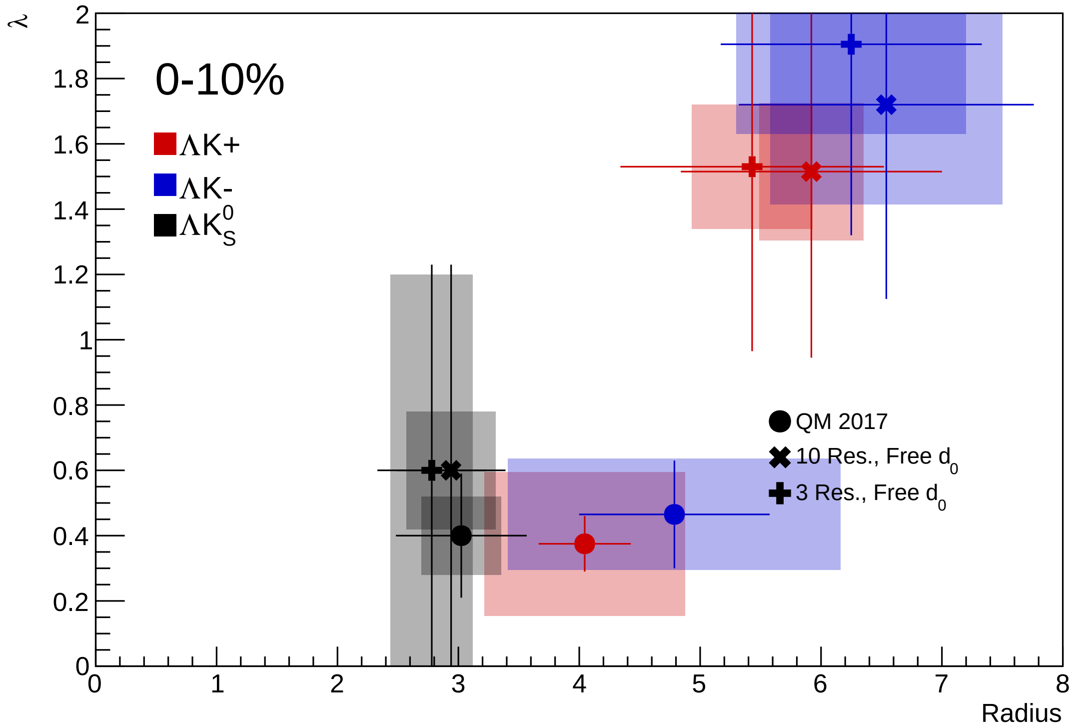

Fig. 22: Extracted λ vs Radius results, for the 0-10% centrality bin, for all of our ΛK systems. The plot shows results including no residuals (circles), 10 residual pairs (X), and 3 residual pairs (+). Note, ΛK^+ on the plot is shorthand for ΛK^+ and $\bar{\Lambda} K^-$, and similar for the others.

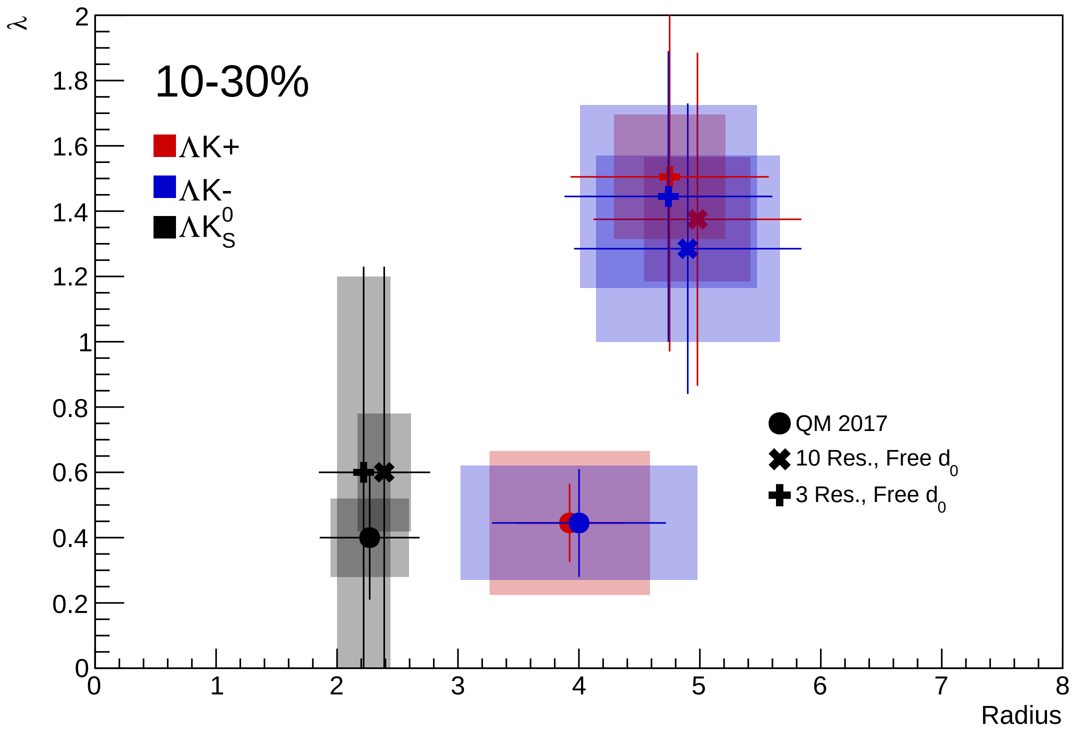

Fig. 23: Extracted λ vs Radius results, for the 10-30% centrality bin, for all of our ΛK systems. The plot shows results including no residuals (circles), 10 residual pairs (X), and 3 residual pairs (+). Note, ΛK^+ on the plot is shorthand for ΛK^+ and $\bar{\Lambda} K^-$, and similar for the others.

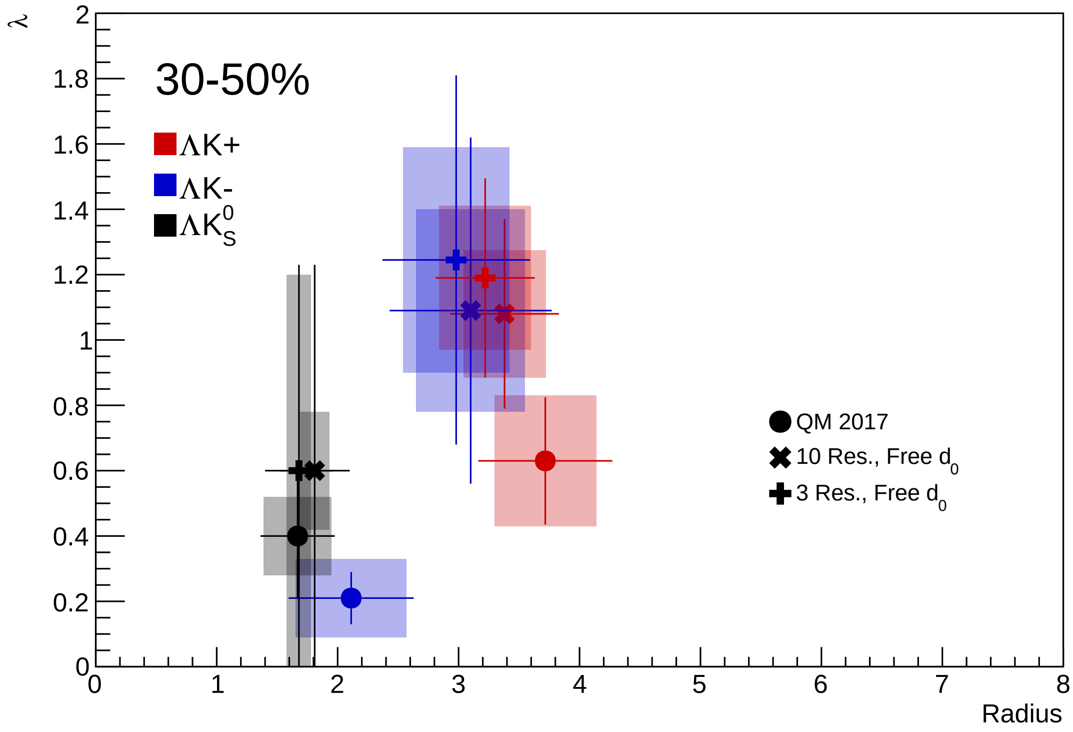

Fig. 24: Extracted λ vs Radius results, for the 30-50% centrality bin, for all of our ΛK systems. The plot shows results including no residuals (circles), 10 residual pairs (X), and 3 residual pairs (+). Note, ΛK^{+} on the plot is shorthand for ΛK^{+} and $\bar{\Lambda}K^{-}$, and similar for the others.

7.1.1 Results: ΛK^0_S and $\Lambda K^{\pm}$: No Residual Correlations Included in Fit

Figures 25, 27, and 29 (Section 7) show experimental data with fits for all studied centralities for ΛK^0_S with $\bar{\Lambda}K^0_S$, ΛK^+ with $\bar{\Lambda}K^-$, and ΛK^- with $\bar{\Lambda}K^+$, respectively. The parameter sets extracted from the fits can be found in Tables 7 and 8. All correlation functions were normalized in the range $0.32 < k^* < 0.40$ GeV/c, and fit in the range $0.0 < k^* < 0.30$ GeV/c. For the ΛK^- and $\bar{\Lambda}K^+$ analyses, the region $0.19 < k^* < 0.23$ GeV/c was excluded from the fit to exclude the bump caused by the Ω^- resonance. The non-flat background was fit with a linear form from $0.6 < k^* < 0.9$ GeV/c. The theoretical fit function was then multiplied by this background during the fitting process.

In the figures (25, 27, and 29), the black solid line represents the "raw" fit, i.e. not corrected for momentum resolution effects nor non-flat background. The green line shows the fit to the non-flat background. The purple points show the fit after momentum resolution and non-flat background corrections have been applied. The initial values of the parameters is listed, as well as the final fit values with uncertainties.

For the ΛK^0_S fits without residuals, λ was restricted to [0.4, 0.6].

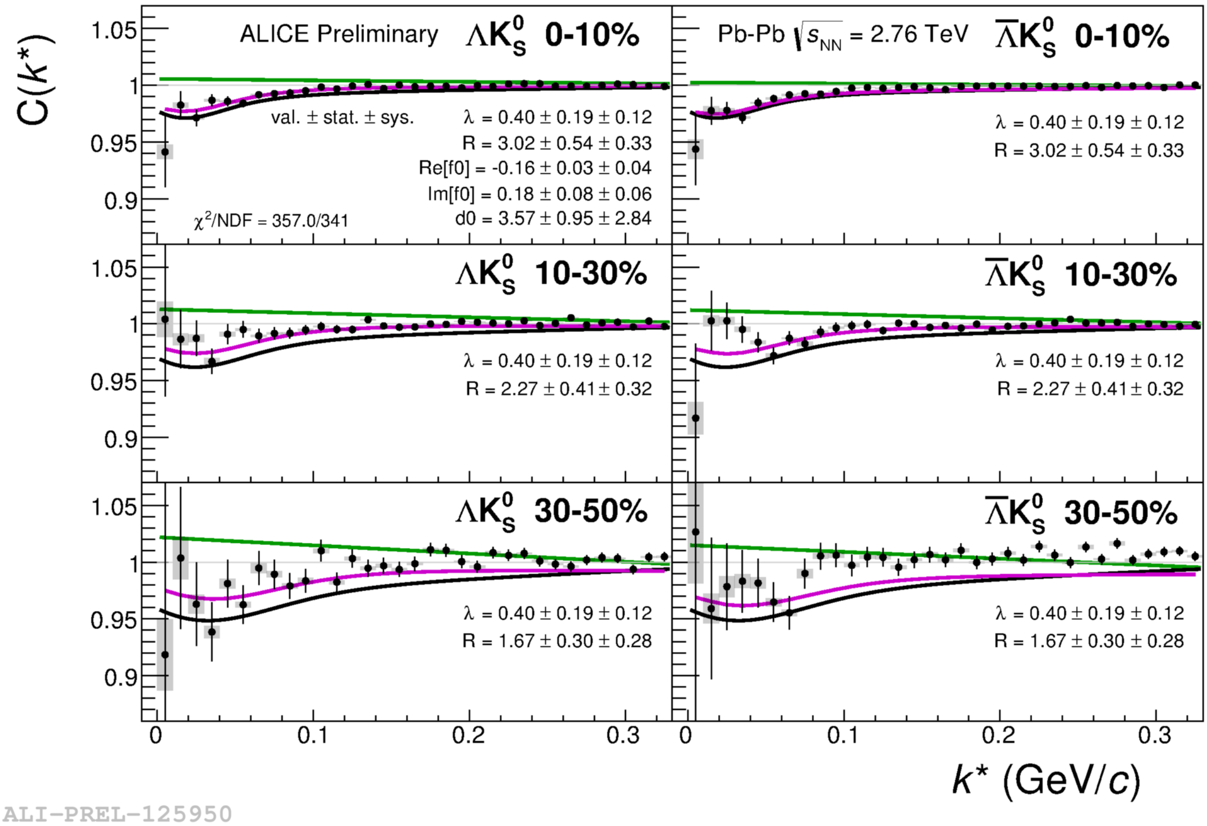

Fig. 25: Fits, with NO residual correlations included, to the ΛK^0_S (left) and $\bar{\Lambda}K^0_S$ (right) data for the centralities 0-10% (top), 10-30% (middle), and 30-50% (bottom). The lines represent the statistical errors, while the boxes represent the systematic errors. Each has unique λ and normalization parameters. The radii are shared amongst like centralities; the scattering parameters ($\mathbb{R}f_0$, $\mathbb{I}f_0$, d_0) are shared amongst all. The black solid line represents the "raw" fit, i.e. not corrected for momentum resolution effects nor non-flat background. The green line shows the fit to the non-flat background. The purple points show the fit after momentum resolution and non-flat background corrections have been applied. The initial values of the parameters is listed, as well as the final fit values with uncertainties. Here, R was restricted to [2.,10.] and Λ was restricted to [0.1,0.8].

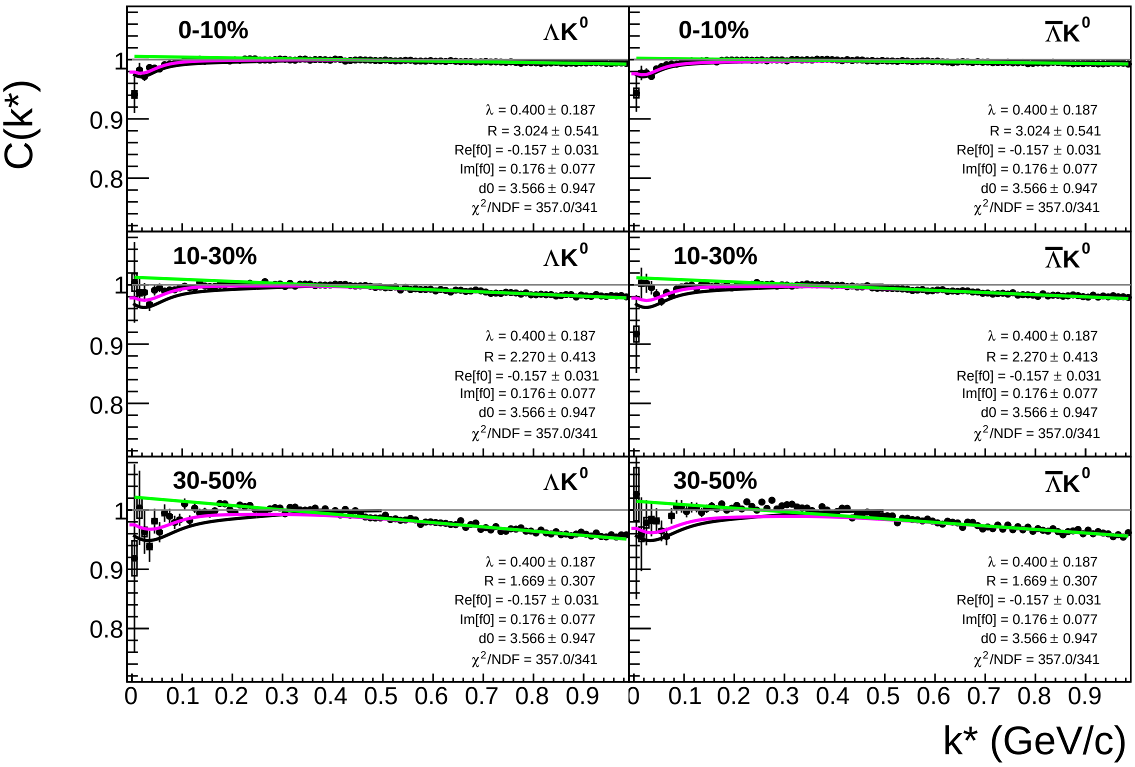

Fig. 26: Same as Fig. 25, but with a wider range of view. Fits, with NO residual correlations included, to the ΛK^0_S (left) and $\bar{\Lambda} K^0_S$ (right) data for the centralities 0-10% (top), 10-30% (middle), and 30-50% (bottom). The lines represent the statistical errors, while the boxes represent the systematic errors. Each has unique λ and normalization parameters. The radii are shared amongst like centralities; the scattering parameters ($\mathbb{R}f_0$, $\mathbb{I}f_0$, d_0) are shared amongst all. The black solid line represents the "raw" fit, i.e. not corrected for momentum resolution effects nor non-flat background. The green line shows the fit to the non-flat background. The purple points show the fit after momentum resolution and non-flat background corrections have been applied. The initial values of the parameters is listed, as well as the final fit values with uncertainties. Here, R was restricted to [2.,10.] and Λ was restricted to [0.1,0.8].

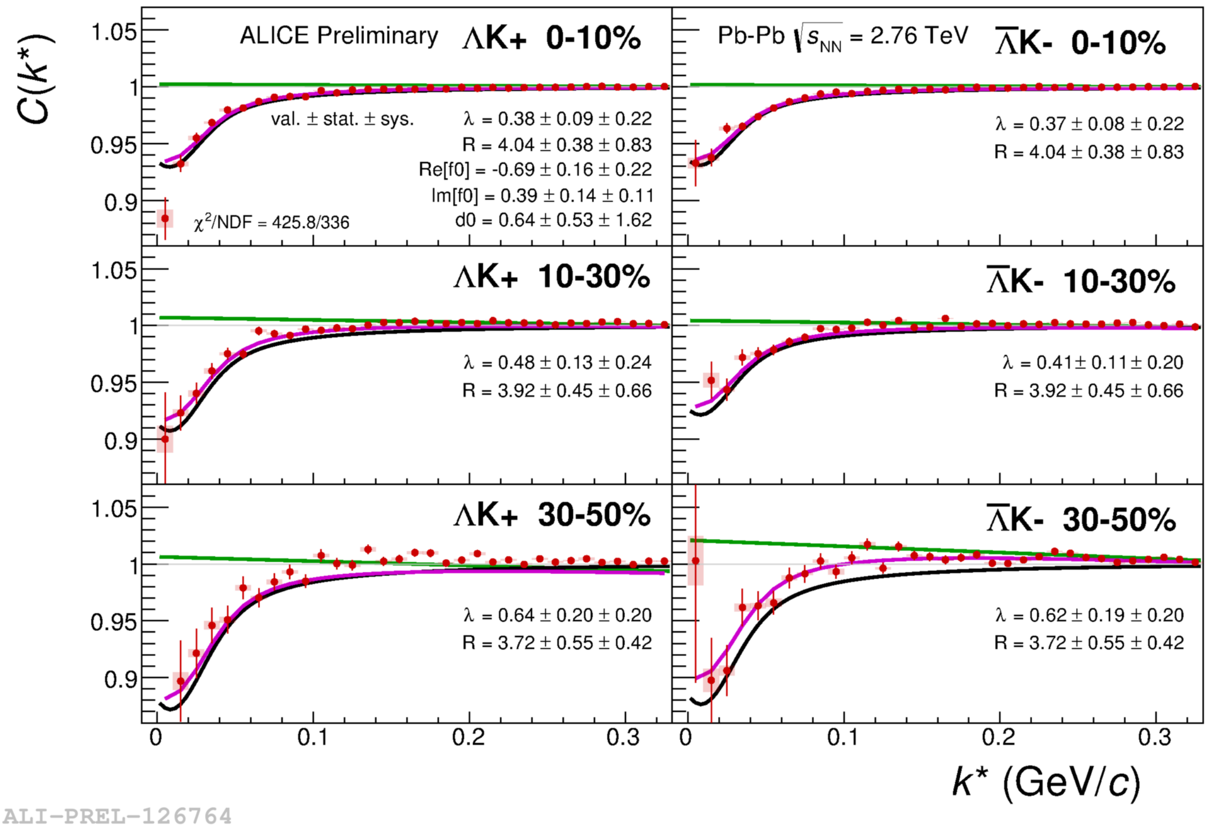

Fig. 27: Fits to the ΛK^+ (left) and $\bar{\Lambda}K^-$ (right) data for the centralities 0-10% (top), 10-30% (middle), and 30-50% (bottom). The lines represent the statistical errors, while the boxes represent the systematic errors. Each has unique λ and normalization parameters. The radii are shared amongst like centralities; the scattering parameters ($\mathbb{R}f_0$, $\mathbb{I}f_0$, d_0) are shared amongst all. The black solid line represents the "raw" fit, i.e. not corrected for momentum resolution effects nor non-flat background. The green line shows the fit to the non-flat background. The purple points show the fit after momentum resolution and non-flat background corrections have been applied. The initial values of the parameters is listed, as well as the final fit values with uncertainties.

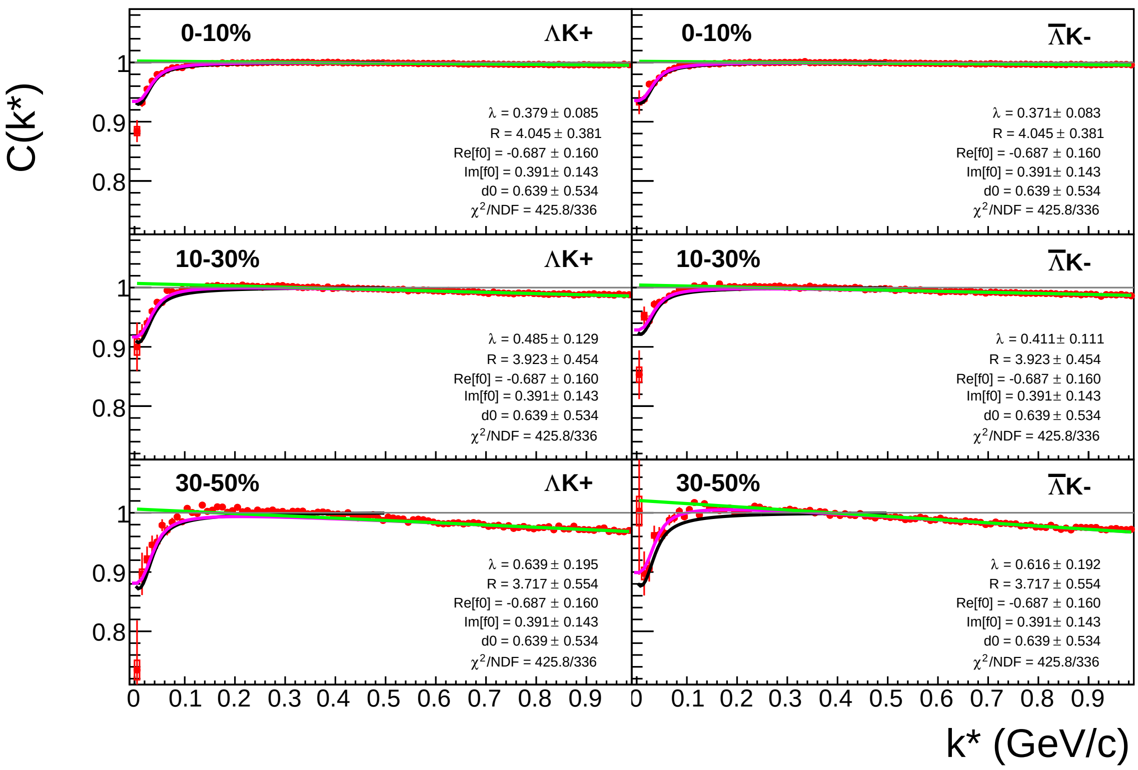

Fig. 28: Same as Fig. 27, but with a wider range of view. Fits, with NO residual correlations included, to the ΛK^+ (left) and $\bar{\Lambda}K^-$ (right) data for the centralities 0-10% (top), 10-30% (middle), and 30-50% (bottom). The lines represent the statistical errors, while the boxes represent the systematic errors. Each has unique λ and normalization parameters. The radii are shared amongst like centralities; the scattering parameters ($\mathbb{R}f_0$, $\mathbb{I}f_0$, d_0) are shared amongst all. The black solid line represents the "raw" fit, i.e. not corrected for momentum resolution effects nor non-flat background. The green line shows the fit to the non-flat background. The purple points show the fit after momentum resolution and non-flat background corrections have been applied. The initial values of the parameters is listed, as well as the final fit values with uncertainties.

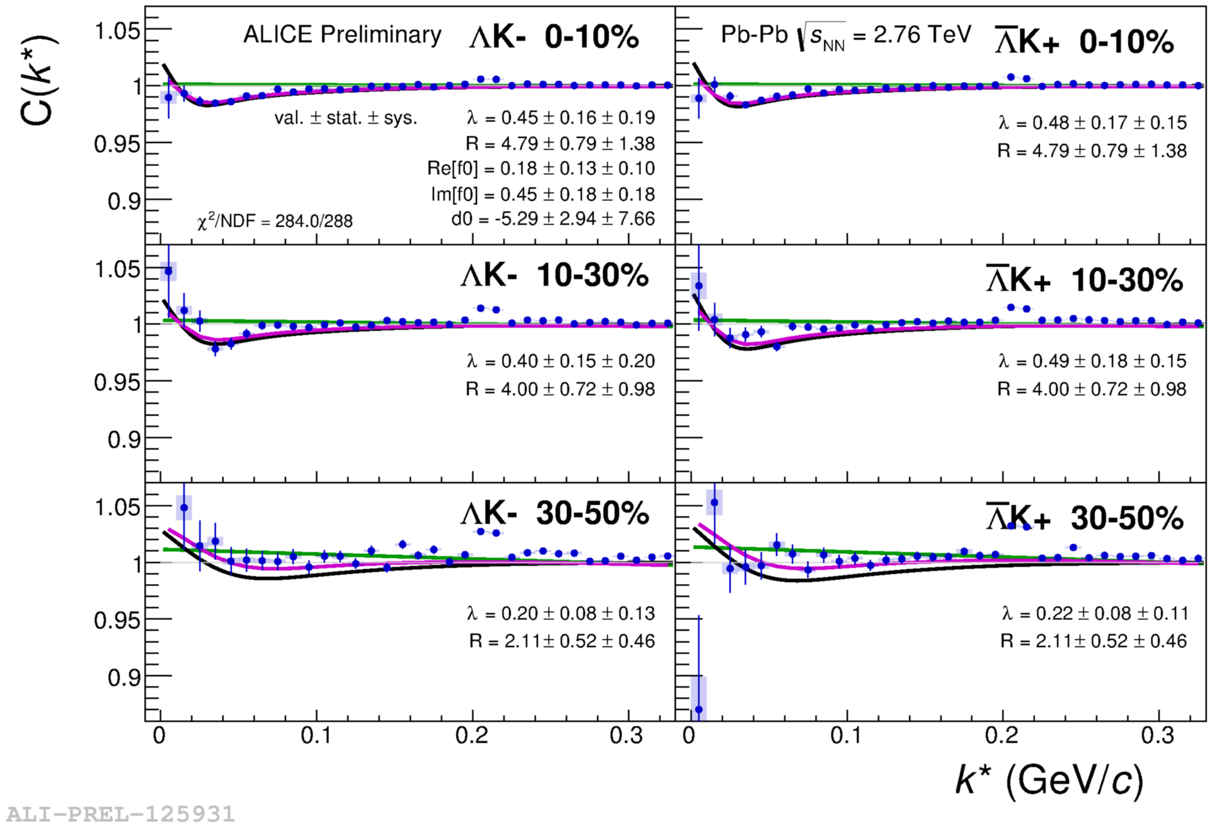

Fig. 29: Fits, with NO residual correlations included, to the ΛK^-(left) with $\bar{\Lambda}K^+$ (right) data for the centralities 0-10% (top), 10-30% (middle), and 30-50% (bottom). The lines represent the statistical errors, while the boxes represent the systematic errors. Each has unique λ and normalization parameters. The radii are shared amongst like centralities; the scattering parameters ($\mathbb{R}f_0$, $\mathbb{I}f_0$, d_0) are shared amongst all. The black solid line represents the "raw" fit, i.e. not corrected for momentum resolution effects nor non-flat background. The green line shows the fit to the non-flat background. The purple points show the fit after momentum resolution and non-flat background corrections have been applied. The initial values of the parameters is listed, as well as the final fit values with uncertainties.

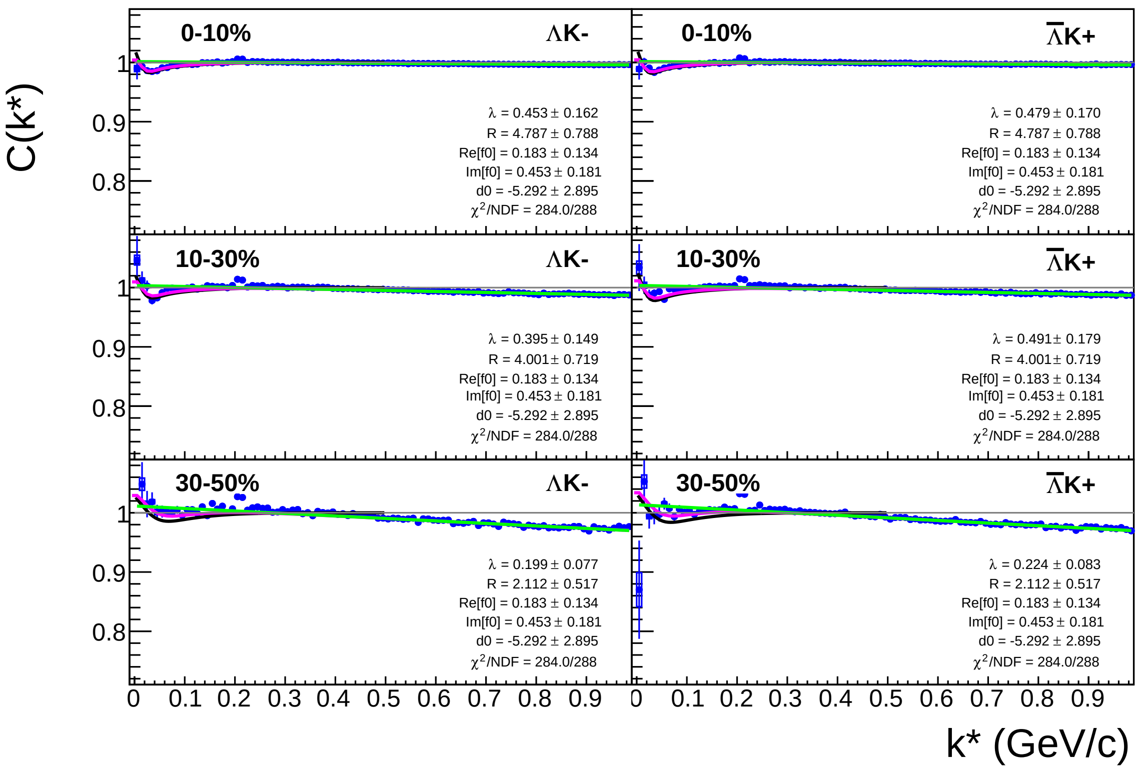

Fig. 30: Same as Fig. 29, but with a wider range of view. Fits, with NO residual correlations included, to the ΛK^-(left) with $\bar{\Lambda}K^+$ (right) data for the centralities 0-10% (top), 10-30% (middle), and 30-50% (bottom). The lines represent the statistical errors, while the boxes represent the systematic errors. Each has unique λ and normalization parameters. The radii are shared amongst like centralities; the scattering parameters ($\mathbb{R}f_0$, $\mathbb{I}f_0$, d_0) are shared amongst all. The black solid line represents the "raw" fit, i.e. not corrected for momentum resolution effects nor non-flat background. The green line shows the fit to the non-flat background. The purple points show the fit after momentum resolution and non-flat background corrections have been applied. The initial values of the parameters is listed, as well as the final fit values with uncertainties.

Fit Results $\Lambda(\bar{\Lambda})K^0_S$

Pair Type	Centrality	Fit Parameters: λ	R	$\mathbb{R}f_0$	$\mathbb{I}f_0$	d_0
ΛK^0_S	0-10%	0.400 ± 0.187 (stat.) ± 0.116 (sys.)	3.024 ± 0.541 (stat.) ± 0.329 (sys.)	-0.157 ± 0.031 (stat.) ± 0.043 (sys.)	0.176 ± 0.077 (stat.) ± 0.059 (sys.)	3.566 ± 0.947 (stat.) ± 2.836 (sys.)
	10-30%		2.270 ± 0.413 (stat.) ± 0.324 (sys.)			
	30-50%		1.669 ± 0.307 (stat.) ± 0.280 (sys.)			
$\bar{\Lambda} K^0_S$	0-10%		3.024 ± 0.541 (stat.) ± 0.329 (sys.)			
	10-30%		2.270 ± 0.413 (stat.) ± 0.324 (sys.)			
	30-50%		1.669 ± 0.307 (stat.) ± 0.280 (sys.)			

Table 7: Fit Results $\Lambda(\bar{\Lambda})K^0_S$. Each pair is fit simultaneously with its conjugate (ie. ΛK^0_S with $\bar{\Lambda} K^0_S$) across all centralities (0-10%, 10-30%, 30-50%), for a total of 6 simultaneous analyses in the fit. Each analysis has a unique λ and normalization parameter. The radii are shared between analyses of like centrality, as these should have similar source sizes. The scattering parameters ($\mathbb{R}f_0$, $\mathbb{I}f_0$, d_0) are shared amongst all. The fit is done on the data with only statistical error bars. The errors marked as "stat." are those returned by MINUIT. The errors marked as "sys." are those which result from my systematic analysis (as outlined in Section 6).

Fit Results $\Lambda(\bar{\Lambda})K^{\pm}$

Pair Type	Centrality	Fit Parameters: λ	R	$\mathbb{R}f_0$	$\mathbb{I}f_0$	d_0
ΛK^+	0-10%	0.379 ± 0.085 (stat.) ± 0.220 (sys.)	4.045 ± 0.381 (stat.) ± 0.830 (sys.)	-0.687 ± 0.160 (stat.) ± 0.223 (sys.)	0.391 ± 0.143 (stat.) ± 0.111 (sys.)	0.639 ± 0.534 (stat.) ± 1.621 (sys.)
	10-30%	0.485 ± 0.129 (stat.) ± 0.241 (sys.)	3.923 ± 0.454 (stat.) ± 0.663 (sys.)			
	30-50%	0.639 ± 0.195 (stat.) ± 0.204 (sys.)	3.717 ± 0.554 (stat.) ± 0.420 (sys.)			
$\bar{\Lambda} K^-$	0-10%	0.371 ± 0.083 (stat.) ± 0.217 (sys.)	4.045 ± 0.381 (stat.) ± 0.830 (sys.)			
	10-30%	0.411 ± 0.111 (stat.) ± 0.201 (sys.)	3.923 ± 0.454 (stat.) ± 0.663 (sys.)			
	30-50%	0.616 ± 0.192 (stat.) ± 0.203 (sys.)	3.717 ± 0.554 (stat.) ± 0.420 (sys.)			
ΛK^-	0-10%	0.453 ± 0.162 (stat.) ± 0.186 (sys.)	4.787 ± 0.788 (stat.) ± 1.375 (sys.)	0.183 ± 0.134 (stat.) ± 0.095 (sys.)	0.453 ± 0.181 (stat.) ± 0.184 (sys.)	-5.292 ± 2.895 (stat.) ± 7.658 (sys.)
	10-30%	0.395 ± 0.149 (stat.) ± 0.198 (sys.)	4.001 ± 0.719 (stat.) ± 0.978 (sys.)			
	30-50%	0.199 ± 0.077 (stat.) ± 0.132 (sys.)	2.112 ± 0.517 (stat.) ± 0.457 (sys.)			
$\bar{\Lambda} K^+$	0-10%	0.479 ± 0.170 (stat.) ± 0.152 (sys.)	4.787 ± 0.788 (stat.) ± 1.375 (sys.)			
	10-30%	0.491 ± 0.179 (stat.) ± 0.148 (sys.)	4.001 ± 0.719 (stat.) ± 0.978 (sys.)			
	30-50%	0.224 ± 0.083 (stat.) ± 0.106 (sys.)	2.112 ± 0.517 (stat.) ± 0.457 (sys.)			

Table 8: Fit Results $\Lambda(\bar{\Lambda})K^{\pm}$ Each pair is fit simultaneously with its conjugate (ie. ΛK^+ with $\bar{\Lambda} K^-$ and ΛK^- with $\bar{\Lambda} K^+$) across all centralities (0-10%, 10-30%, 30-50%), for a total of 6 simultaneous analyses in the fit. Each analysis has a unique λ and normalization parameter. The radii are shared between analyses of like centrality, as these should have similar source sizes. The scattering parameters ($\mathbb{R}f_0$, $\mathbb{I}f_0$, d_0) are shared amongst all. The fit is done on the data with only statistical error bars. The errors marked as "stat." are those returned by MINUIT. The errors marked as "sys." are those which result from my systematic analysis (as outlined in Section 6).

		Fit Parameters (value ± statistical error ± systematic error)		
Pair Type	**Centrality**	**R**		
ΛK^{+} & $\bar{\Lambda}K^{-}$	**0-10%**	**4.04 ± 0.38 ± 0.83**		
	10-30%	**3.92 ± 0.45 ± 0.66**		
	30-50%	**3.72 ± 0.55 ± 0.42**		
		$\Re f_0$	$\Im f_0$	d_0
		-0.69 ± 0.16 ± 0.22	**0.39 ± 0.14 ± 0.11**	**0.64 ± 0.53 ± 1.62**
ΛK^{-} & $\bar{\Lambda}K^{+}$	**0-10%**	**4.79 ± 0.79 ± 1.38**		
	10-30%	**4.00 ± 0.72 ± 0.98**		
	30-50%	**2.11 ± 0.52 ± 0.46**		
		$\Re f_0$	$\Im f_0$	d_0
		0.18 ± 0.13 ± 0.10	**0.45 ± 0.18 ± 0.18**	**-5.29 ± 2.94 ± 7.66**
ΛK^{0}_{S} & $\bar{\Lambda}K^{0}_{S}$	**0-10%**	**3.02 ± 0.54 ± 0.33**		
	10-30%	**2.27 ± 0.41 ± 0.32**		
	30-50%	**1.67 ± 0.30 ± 0.28**		
		$\Re f_0$	$\Im f_0$	d_0
		-0.16 ± 0.03 ± 0.04	**0.18 ± 0.08 ± 0.06**	**3.57 ± 0.95 ± 2.84**

Figure 39 shows extracted $R_{\rm inv}$ parameters as a function of tranverse mass ($m_{\rm T}$) for various pair systems over several centralities. The published ALICE data [10] is shown with transparent, open symbols. The new ΛK results are shown with opaque, filled symbols. The radii shown an increasing size with increasing centrality, as is expected from the simple geometric picture of the collisions. The radii decrease in size with increasing $m_{\rm T}$, and we see an approximate scaling of the radii with transverse mass, as is expected in the presence of collective flow in the system.

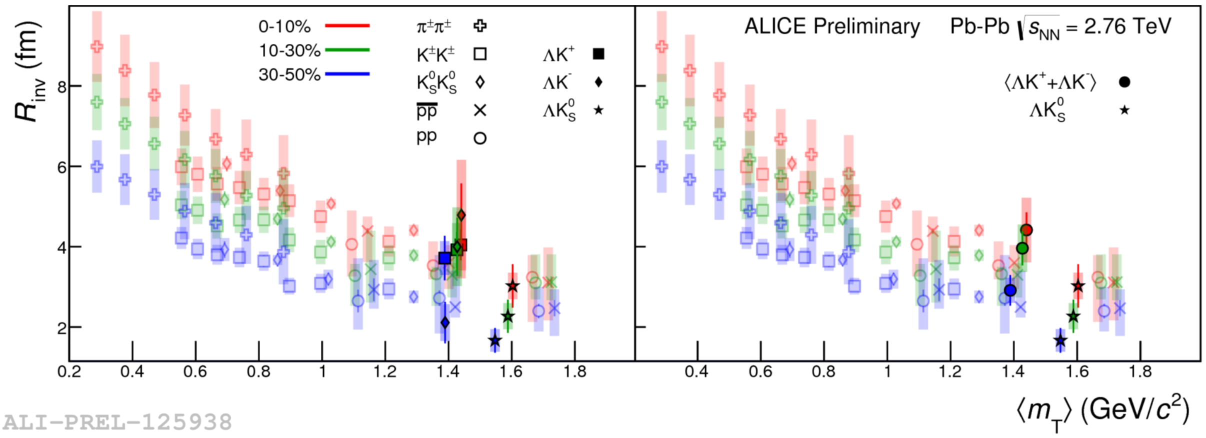

Fig. 31: No residual correlations in ΛK fits. Extracted fit $R_{\rm inv}$ parameters as a function of pair transverse mass ($m_{\rm T}$) for various pair systems over several centralities. The ALICE published data [10] is shown with transparent, open symbols. The new ΛK results are shown with opaque, filled symbols. In the left, the ΛK^+ (with it's conjugate pair) results are shown separately from the ΛK^- (with it's conjugate pair) results. In the right, all $\Lambda K^{\pm}$ results are averaged.

648 ### 7.1.2 Results: ΛK^0_S and $\Lambda K^{\pm}$: 3 Residual Correlations Included in Fit

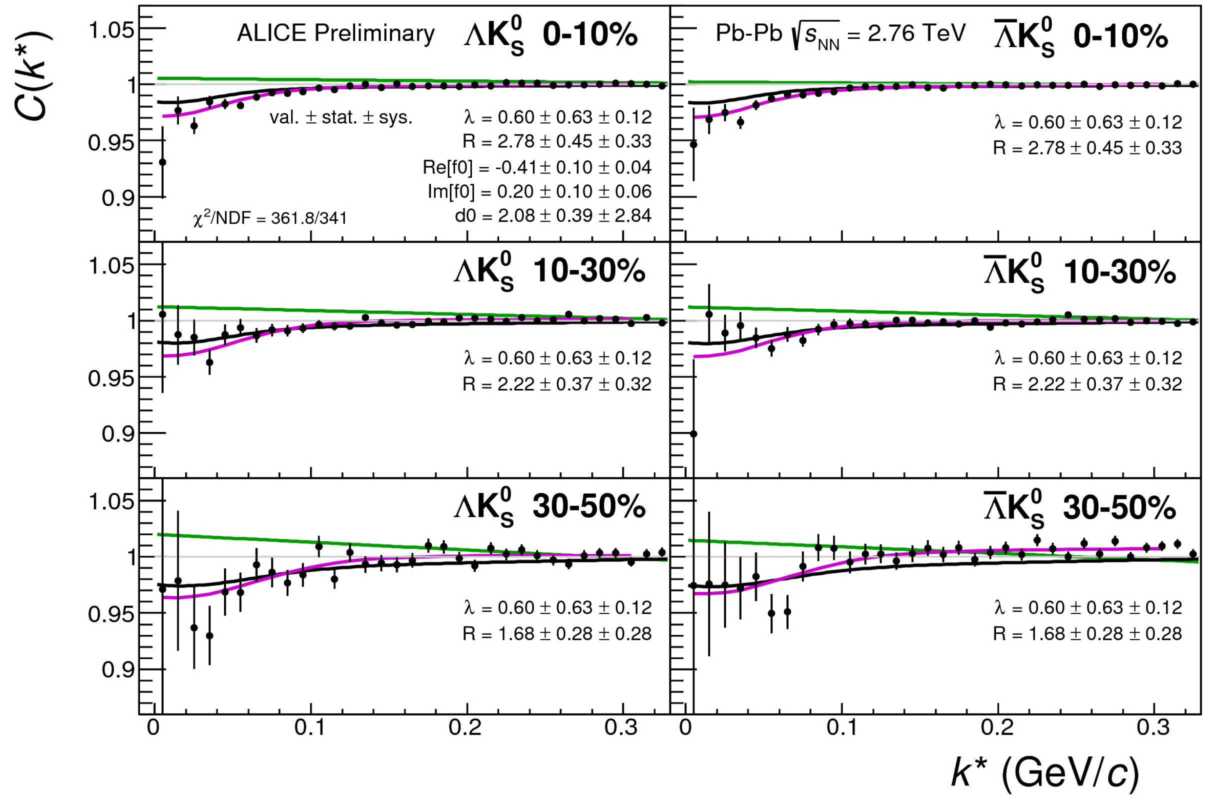

Fig. 32: Fits, with 3 residual correlations included, to the ΛK^0_S (left) and $\bar{\Lambda} K^0_S$ (right) data for the centralities 0-10% (top), 10-30% (middle), and 30-50% (bottom). The lines represent the statistical errors, while the boxes represent the systematic errors. Each has unique λ and normalization parameters. The radii are shared amongst like centralities; the scattering parameters ($\mathbb{R}f_0$, $\mathbb{I}f_0$, d_0) are shared amongst all. The black solid line represents the "raw" fit, i.e. not corrected for momentum resolution effects nor non-flat background. The green line shows the fit to the non-flat background. The purple points show the fit after momentum resolution and non-flat background corrections have been applied. The initial values of the parameters is listed, as well as the final fit values with uncertainties. Here, R was restricted to [2.,10.] and Λ was restricted to [0.1,0.8].

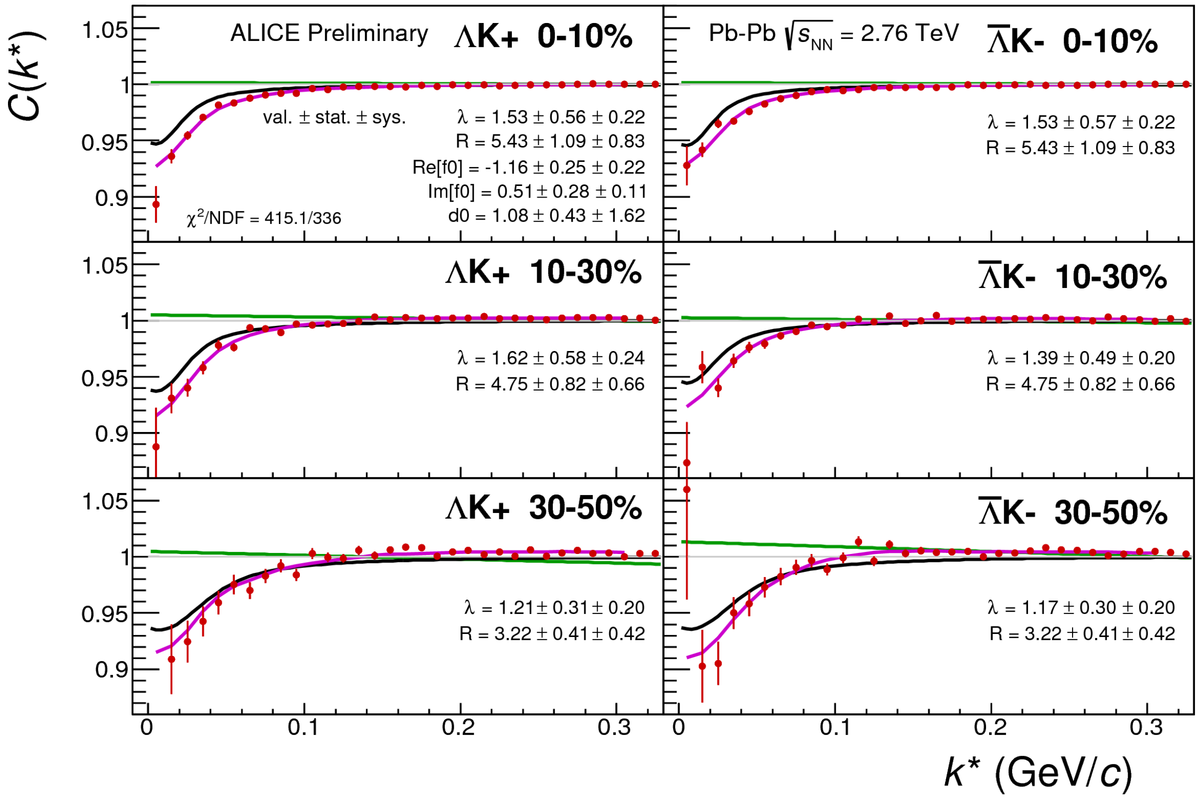

Fig. 33: Fits, with 3 residual correlations included, to the ΛK^+ (left) and $\bar{\Lambda}K^-$ (right) data for the centralities 0-10% (top), 10-30% (middle), and 30-50% (bottom). The lines represent the statistical errors, while the boxes represent the systematic errors. Each has unique λ and normalization parameters. The radii are shared amongst like centralities; the scattering parameters ($\mathbb{R}f_0$, $\mathbb{I}f_0$, d_0) are shared amongst all. The black solid line represents the "raw" fit, i.e. not corrected for momentum resolution effects nor non-flat background. The green line shows the fit to the non-flat background. The purple points show the fit after momentum resolution and non-flat background corrections have been applied. The initial values of the parameters is listed, as well as the final fit values with uncertainties.

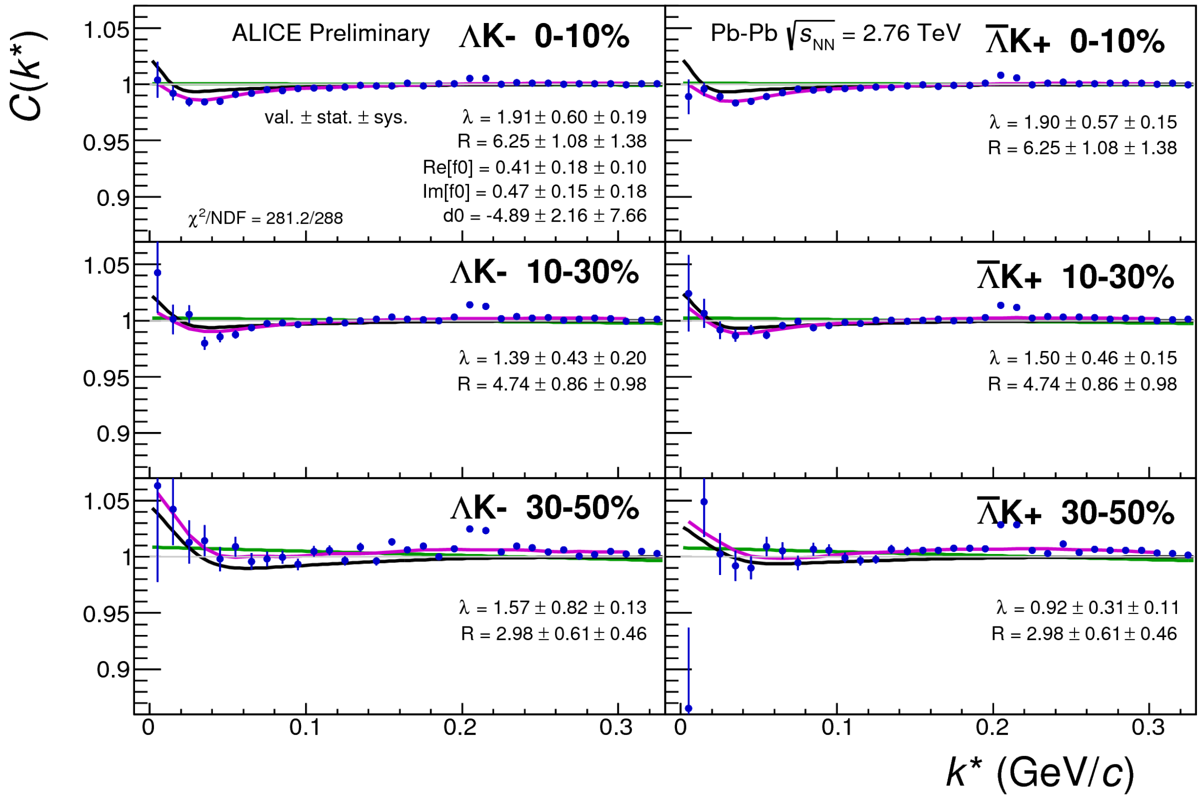

Fig. 34: Fits, with 3 residual correlations included, to the ΛK^-(left) with $\bar{\Lambda}K^+$ (right) data for the centralities 0-10% (top), 10-30% (middle), and 30-50% (bottom). The lines represent the statistical errors, while the boxes represent the systematic errors. Each has unique λ and normalization parameters. The radii are shared amongst like centralities; the scattering parameters ($\mathbb{R}f_0$, $\mathbb{I}f_0$, d_0) are shared amongst all. The black solid line represents the "raw" fit, i.e. not corrected for momentum resolution effects nor non-flat background. The green line shows the fit to the non-flat background. The purple points show the fit after momentum resolution and non-flat background corrections have been applied. The initial values of the parameters is listed, as well as the final fit values with uncertainties.

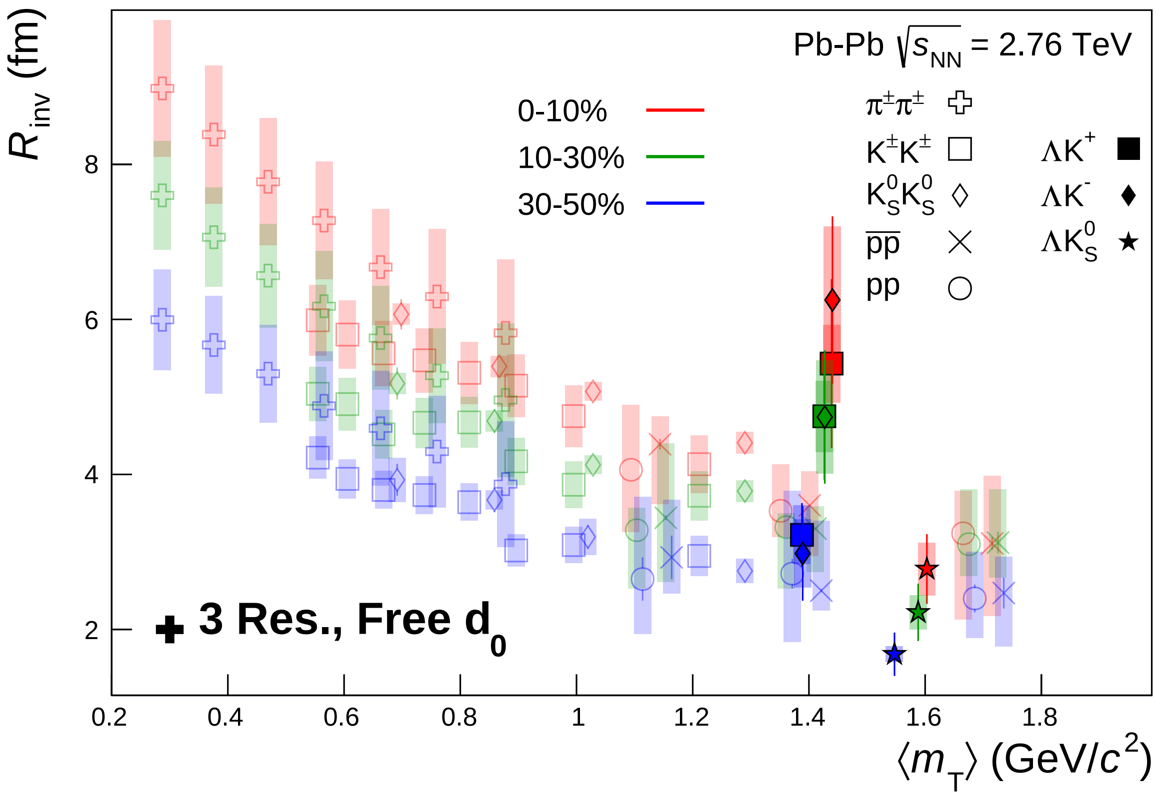

Fig. 35: 3 residual correlations in ΛK fits. Extracted fit R_{inv} parameters as a function of pair transverse mass (m_T) for various pair systems over several centralities. The ALICE published data [10] is shown with transparent, open symbols. The new ΛK results are shown with opaque, filled symbols. In the left, the ΛK^+ (with it's conjugate pair) results are shown separately from the ΛK^- (with it's conjugate pair) results. In the right, all $\Lambda K^{\pm}$ results are averaged.

649 ### 7.1.3 *Results: ΛK^0_S and $\Lambda K^{\pm}$: 10 Residual Correlations Included in Fit*

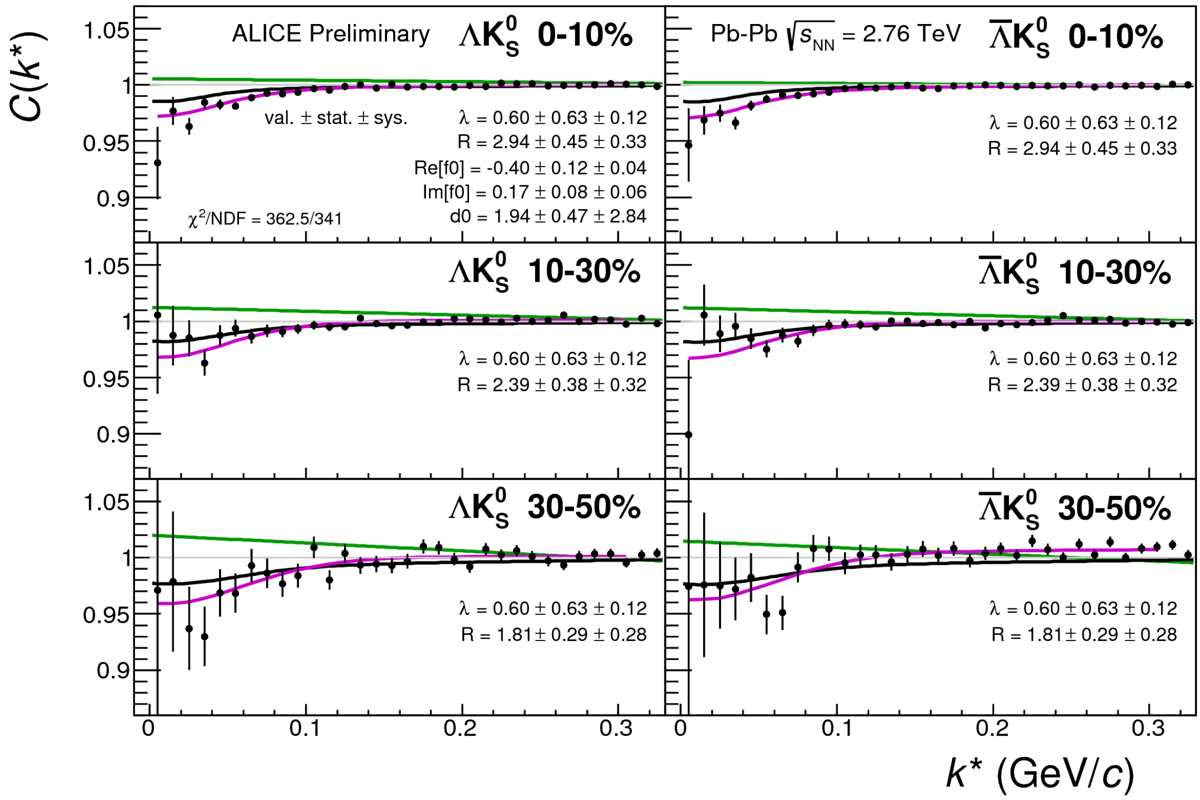

Fig. 36: Fits, with 10 residual correlations included, to the ΛK^0_S (left) and $\bar{\Lambda}K^0_S$ (right) data for the centralities 0-10% (top), 10-30% (middle), and 30-50% (bottom). The lines represent the statistical errors, while the boxes represent the systematic errors. Each has unique λ and normalization parameters. The radii are shared amongst like centralities; the scattering parameters ($\mathbb{R}f_0$, $\mathbb{I}f_0$, d_0) are shared amongst all. The black solid line represents the "raw" fit, i.e. not corrected for momentum resolution effects nor non-flat background. The green line shows the fit to the non-flat background. The purple points show the fit after momentum resolution and non-flat background corrections have been applied. The initial values of the parameters is listed, as well as the final fit values with uncertainties. Here, R was restricted to [2.,10.] and Λ was restricted to [0.1,0.8].

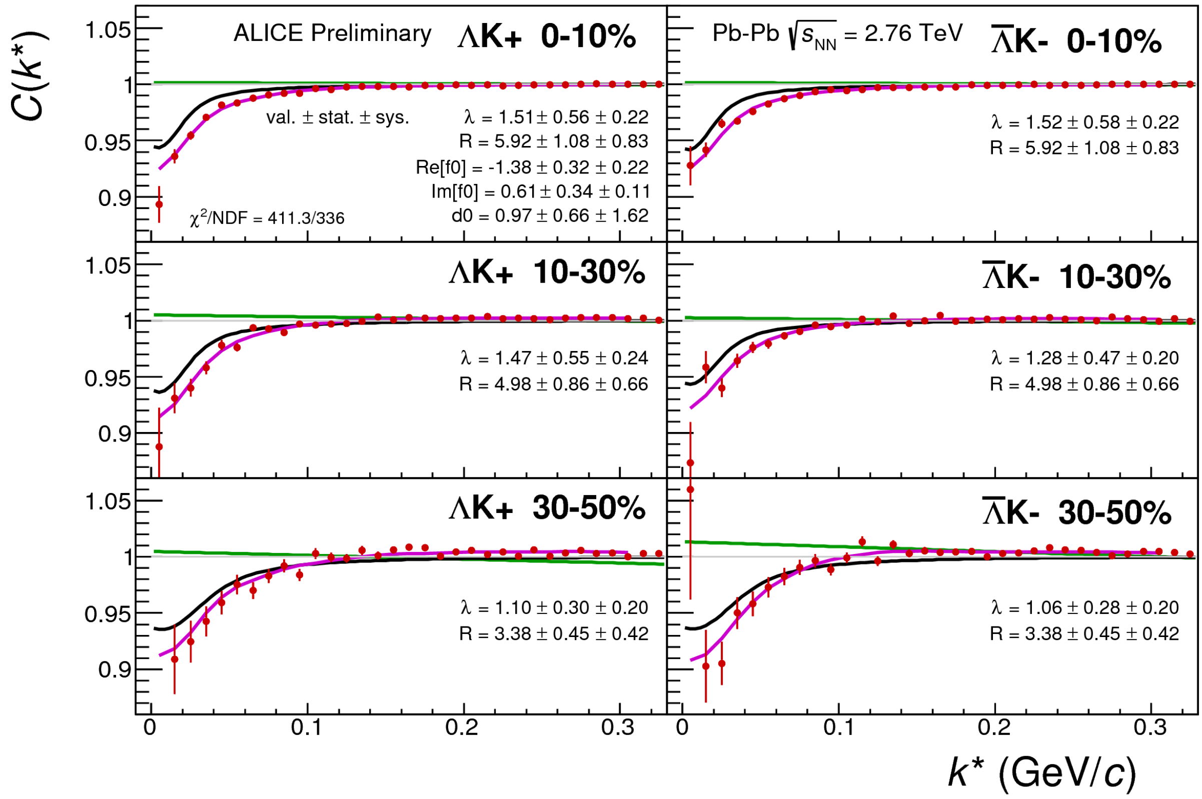

Fig. 37: Fits, with 10 residual correlations included, to the ΛK^{+} (left) and $\bar{\Lambda}K^{-}$ (right) data for the centralities 0-10% (top), 10-30% (middle), and 30-50% (bottom). The lines represent the statistical errors, while the boxes represent the systematic errors. Each has unique λ and normalization parameters. The radii are shared amongst like centralities; the scattering parameters ($\mathbb{R}f_0$, $\mathbb{I}f_0$, d_0) are shared amongst all. The black solid line represents the "raw" fit, i.e. not corrected for momentum resolution effects nor non-flat background. The green line shows the fit to the non-flat background. The purple points show the fit after momentum resolution and non-flat background corrections have been applied. The initial values of the parameters is listed, as well as the final fit values with uncertainties.

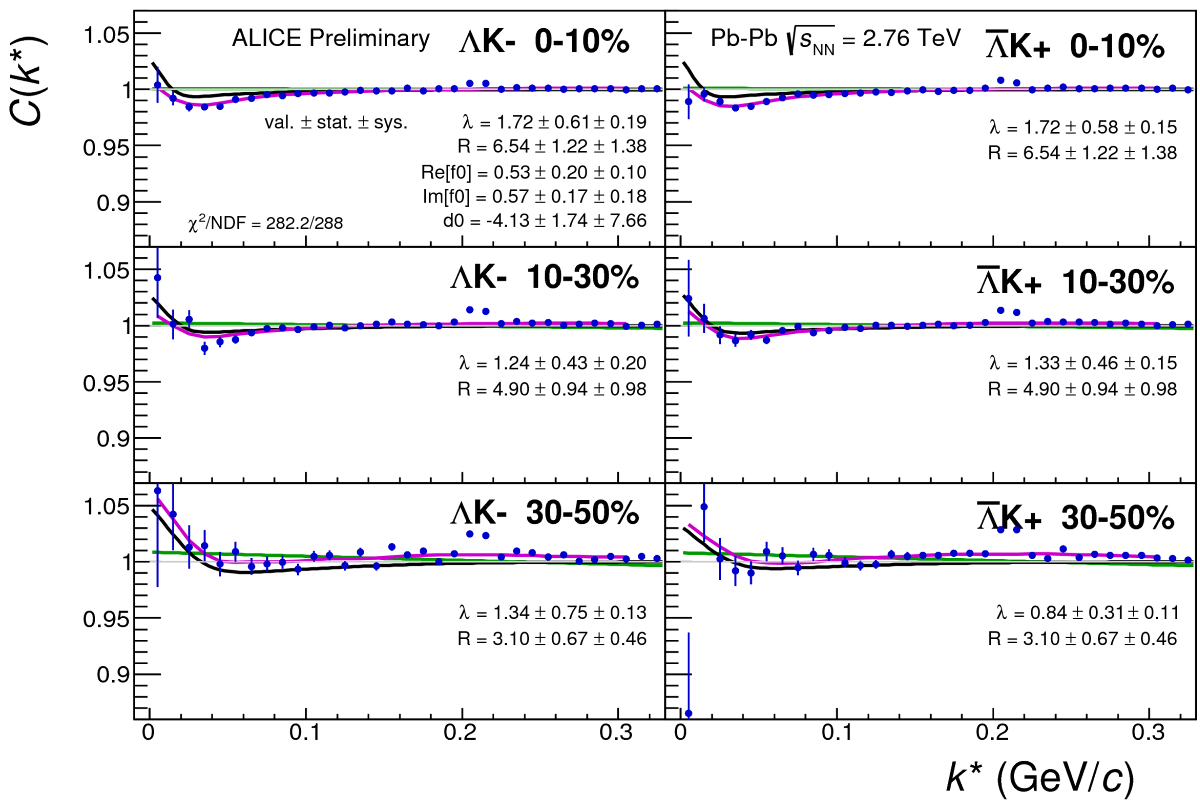

Fig. 38: Fits, with 10 residual correlations included, to the ΛK^-(left) with $\bar{\Lambda}K^+$ (right) data for the centralities 0-10% (top), 10-30% (middle), and 30-50% (bottom). The lines represent the statistical errors, while the boxes represent the systematic errors. Each has unique λ and normalization parameters. The radii are shared amongst like centralities; the scattering parameters ($\mathbb{R}f_0$, $\mathbb{I}f_0$, d_0) are shared amongst all. The black solid line represents the "raw" fit, i.e. not corrected for momentum resolution effects nor non-flat background. The green line shows the fit to the non-flat background. The purple points show the fit after momentum resolution and non-flat background corrections have been applied. The initial values of the parameters is listed, as well as the final fit values with uncertainties.

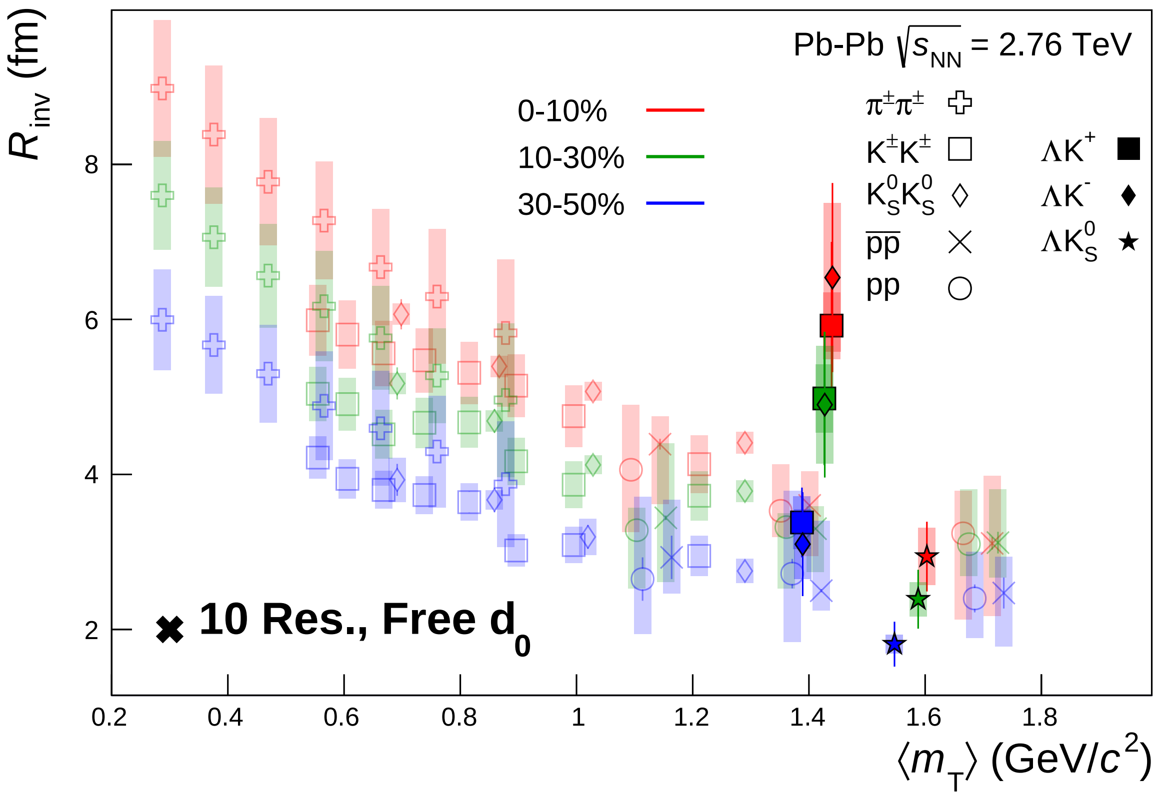

Fig. 39: 10 residual correlations in ΛK fits. Extracted fit R_{inv} parameters as a function of pair transverse mass (m_T) for various pair systems over several centralities. The ALICE published data [10] is shown with transparent, open symbols. The new ΛK results are shown with opaque, filled symbols. In the left, the ΛK^+ (with it's conjugate pair) results are shown separately from the ΛK^- (with it's conjugate pair) results. In the right, all $\Lambda K^{\pm}$ results are averaged.

7.2 Results: $\Xi K^{\pm}$

Even without any fits to the data, the fact that the $\Xi^{-}K^{+}$ data dips below unity (Fig. 40) is exciting, as this cannot occur purely from a Coulomb interaction. We hope that this dip signifies that we are able to peer through the overwhelming contribution from the Coulomb interaction to see the effects arising from the strong interaction.

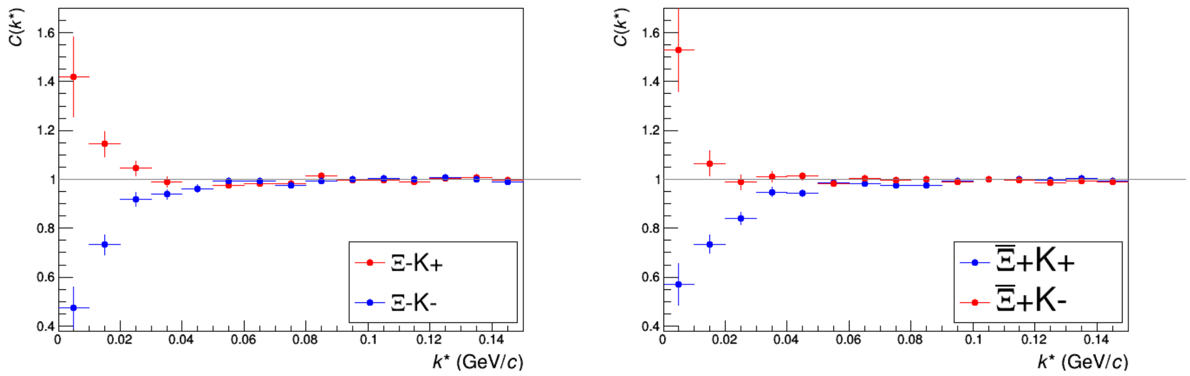

Fig. 40: $\Xi K^{\pm}$ Results for 0-10% Centrality. (Left) $\Xi^{-}K^{+}$ and $\Xi^{-}K^{-}$ (Right) $\bar{\Xi}^{+}K^{+}$ and $\bar{\Xi}^{+}K^{-}$

Figure 41 demonstrates graphically, that the $\Xi^{-}K^{+}$ results cannot be described by solely the Coulomb interaction. In this figure, we present the data along with a Coulomb-only band. The Coulomb-only band is spanned by two Coulomb-only curves, whose parameters are given in the figure. The Coulomb-only curves were generated using a technique identical to the generation of the fit function, described in Sec. 5.2, except, of course, with the nuclear scattering parameters all set to zero. The Coulomb-only curves change monotonically with varying λ or varyin radius parametres, therefore, any curves built with parameter sets intermediate to those use in the Coulomb-only band will be contained in the band.

Including the strong interaction into the simulation can dramatically change the resulting correlation function, as shown in Figure 42. In the figure, the solid line represents a Coulomb-only curve, i.e. a simulated correlation function with the strong interaction turned off. The dashed lines represent a full simulation, including both the strong and Coulomb interactions. The two dashed lines differ only in the real part of the assumed scattering length: positive in Set 1, and negative in Set 2. In the top figure, for the $\Xi^{-}K^{+}$ simulation, we see that parameter set 2, with a negative real part of the scattering length, causes the simulated curve to dip below unity, as is seen in the data. If there is a parallel to be drawn between this analysis and the ΛK analysis, we expect to see similar effects in the ΛK+ system and the $\Xi^{-}K^{+}$ systems. In these systems, we could have an $s\bar{s}$ annihilation picture. Or, another possible way of thinking about these systems is in terms of net strangeness. The ΛK^{+} system has S=0, while the ΛK^{-} has S=-2. The $\Xi^{-}K^{+}$ has S=-1, while the $\Xi^{-}K^{-}$ has S=-3.

The author was asked to perform a global Coulomb-only fit to the data, to ensure that the system truly could not be described simply by the Coulomb interaction. In order words, in the fit, the strong force was turned off, and the $\Xi^{-}K^{+}$, $\bar{\Xi}^{+}K^{-}$, $\Xi^{-}K^{-}$, $\bar{\Xi}^{+}K^{+}$ systems all share one sinlge radius parameter, while the pair and conjugate pair systems share a λ parameter. The results of this fit are shown in Figures 43 and 44. In Fig. 43, there was a lower limit of 0.1 fm placed on the radius parameter, and the radius parameter was initialized to 3 fm (as seems reasonable, when considering the transverse mass of the system and looking at Fig. 39). As is shown in the results, the radius parameter reached this unrealistic lower bound of 0.1 fm. In Fig. 44, the parameters were all unbounded, and the radius parameter was initialized to 10 fm. In this case, the radius parameters reamins high, and ends at an unrealistic value of 10.84 fm. In both cases, the λ parameters are too low. From these figures, we conclude that a global Coulomb-only fit is not suitable for the data.

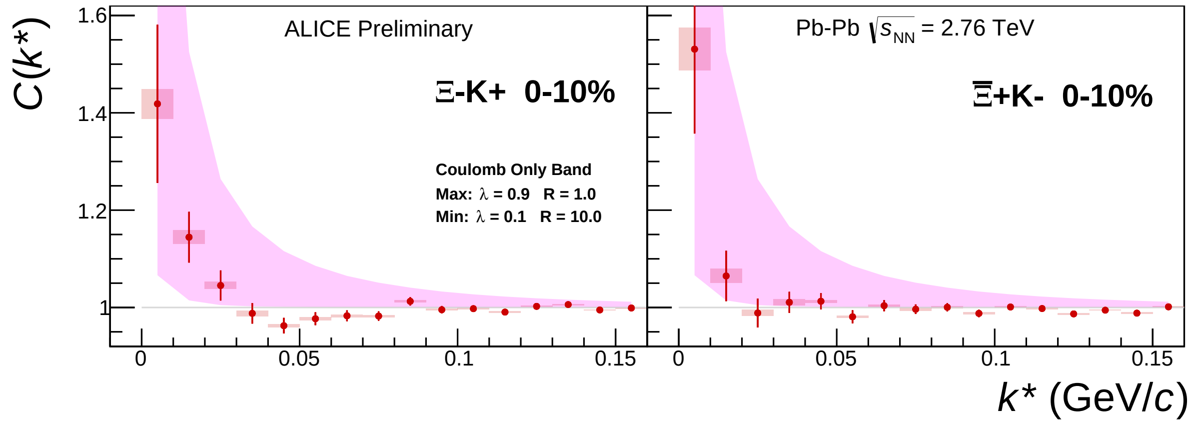

(a) (Left) ΞK^+ and (Right) $\bar{\Xi} K^-$

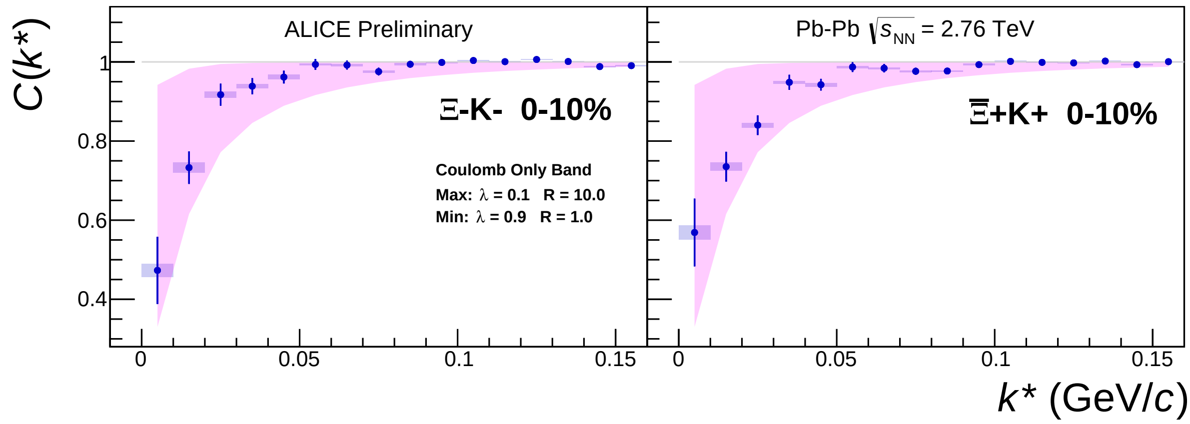

(b) (Left) ΞK^- and (Right) $\bar{\Xi} K^+$

Fig. 41: $\Xi K^{\pm}$ data with Coulomb-only bands for the 0-10% centrality bin. The Coulomb-only bands span two sets of Coulomb-only curves: (1) λ = 0.9, R = 1.0 fm and (2) λ = 0.1, R = 10.0 fm. The Coulomb-only curves are simulated correlation functions for the respective pair system assuming only a Coulomb interaction, i.e. ignoring the strong interaction. The Coulomb-only curves change monotonically with varying λ and varying R, therefore, any intermediate parameter set will fall within this Coulomb-only band.

Although the global Coulomb-only fit failed, it is possible that a Coulomb-only fit performed on $\Xi^- K^+$ and $\bar{\Xi}^+ K^-$ separately from $\Xi^- K^-$ and $\bar{\Xi}^+ K^+$ could be suitable. The result of such fits are shown in Figures 45 and 46. Figure 45, shows that the fit is not able to describe the dip in the $\Xi^- K^+$ data below unity. Of course, this is obviously true for an attractive Coulomb-only fit. The radius parameter of 8.43 fm extracted from this fit is unrealistically large. In Figure 46 shows the Coulomb-only fit can described the $\Xi^- K^-$ data reasonable well; although the extracted radius of 3.73 fm is somewhat larger than expected.

8 To Do

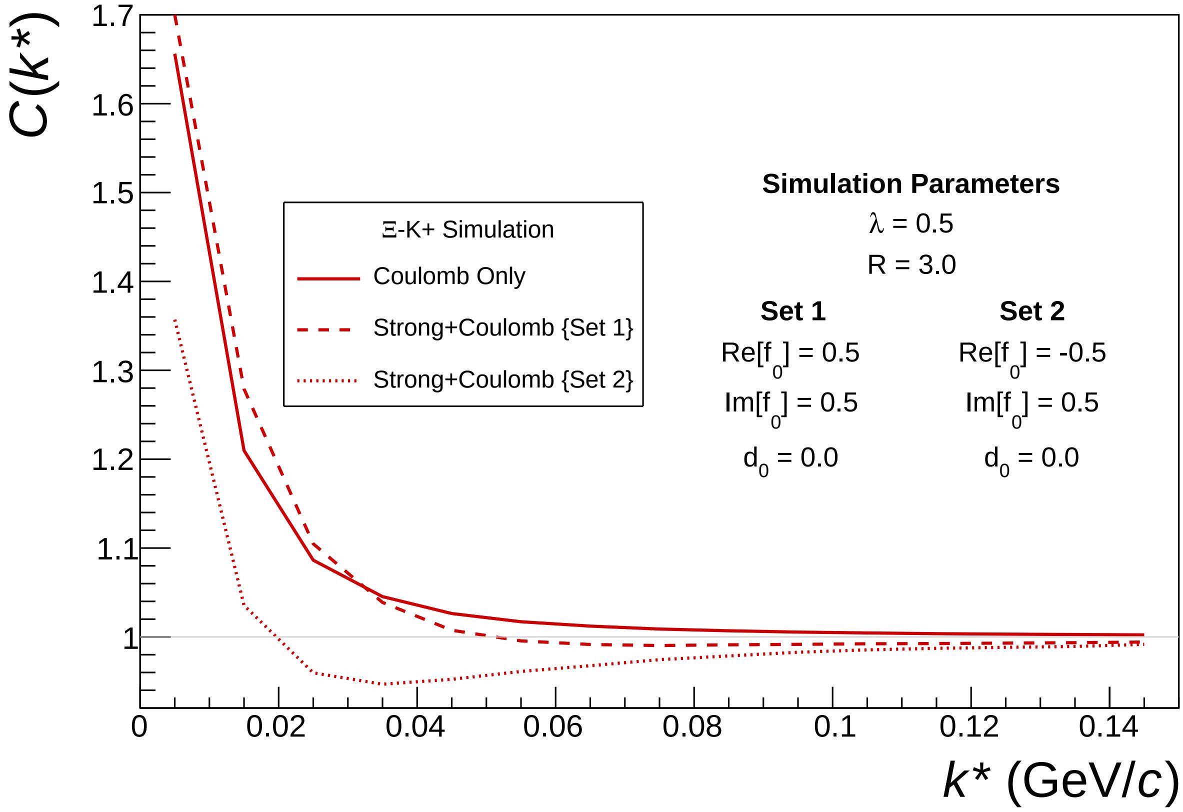

(a) ΞK^+ and $\bar{\Xi} K^-$ simulation

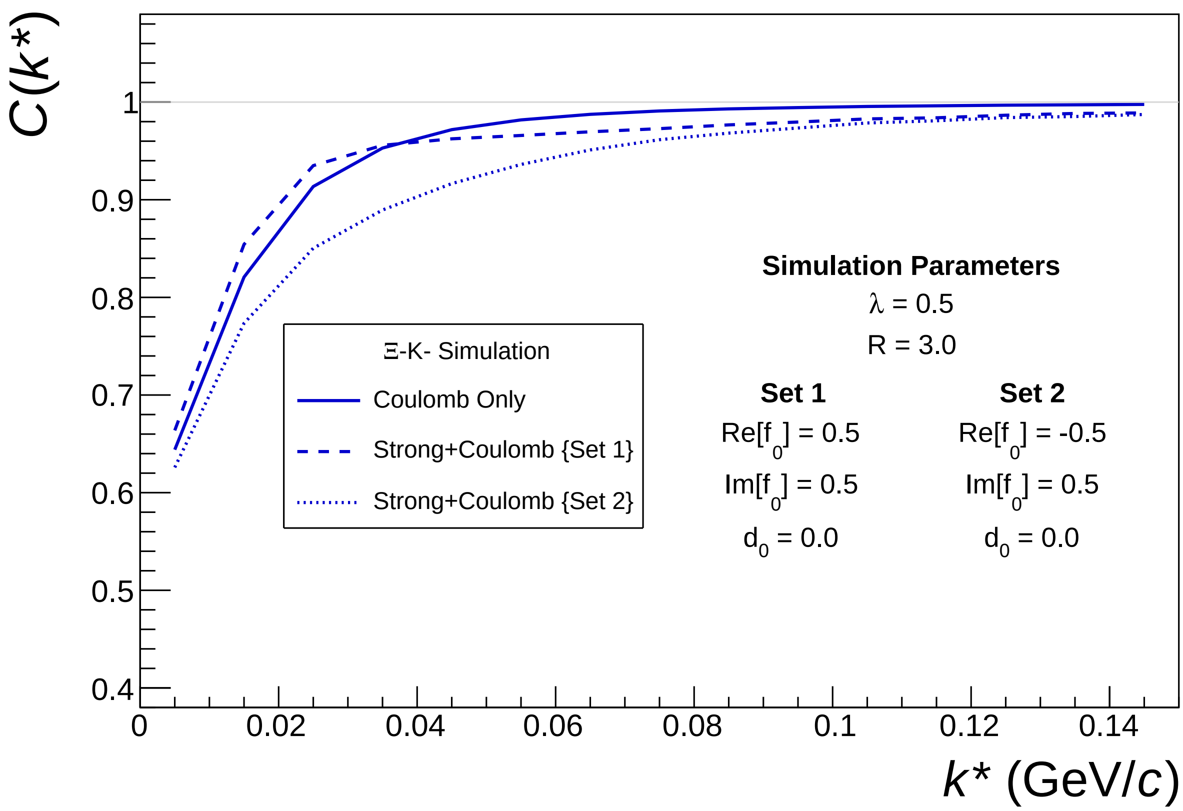

(b) ΞK^- and $\bar{\Xi} K^+$ simulation

Fig. 42: Effect on the Coulomb-only curve of including the strong interaction for $\Xi K^{\pm}$ systems. The solid line represents a Coulomb-only curve, i.e. a simulated correlation function with the strong interaction turned off. The dashed lines represent a full simulation, including both the strong and Coulomb interactions. The two dashed lines differ only in the real part of the assumed scattering length: positive in Set 1, and negative in Set 2.

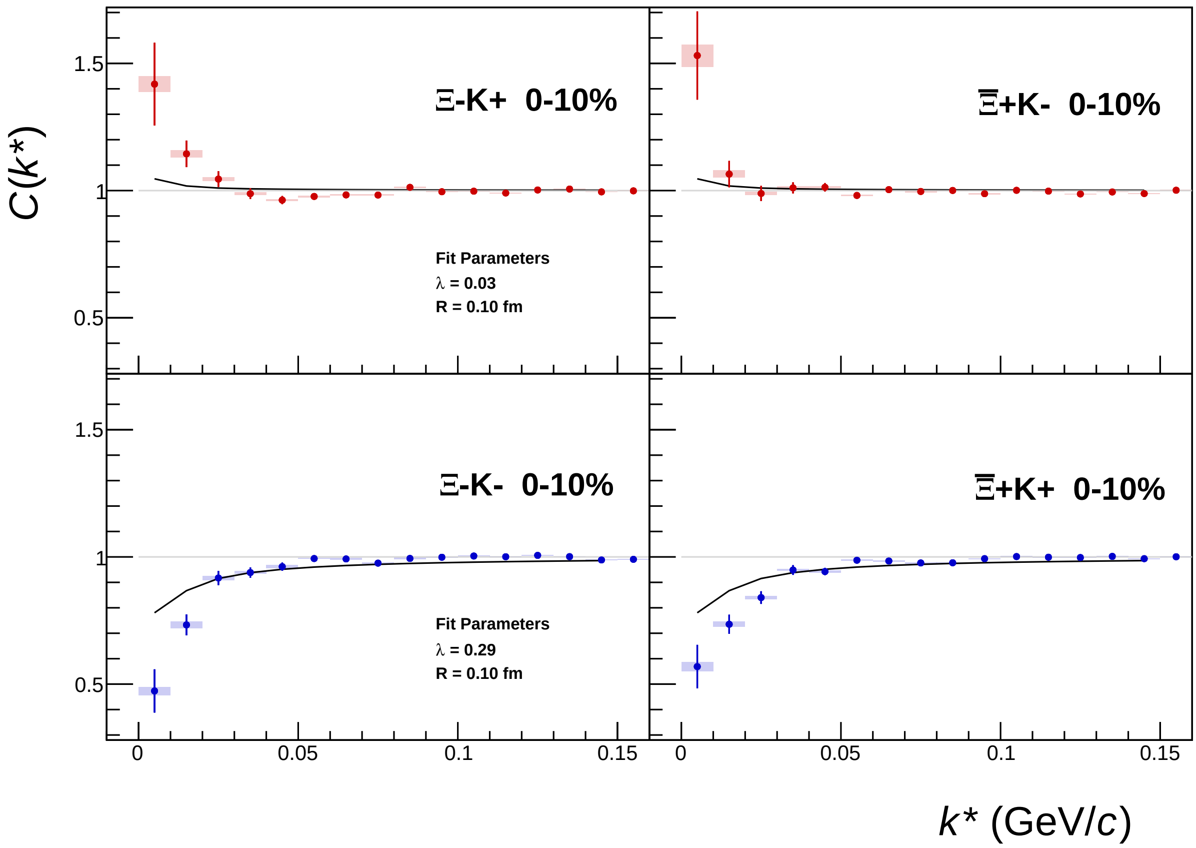

Fig. 43: $\Xi K^{\pm}$ Global Coulomb-only fit (Set 1) for 0-10% centrality. In this fit, there was a lower limit of 0.1 fm placed on the radius parameter, and the radius parameter was initialized to 3 fm (as seems reasonable, when considering the transverse mass of the system and looking at Fig. 39). As is shown in the results, the radius parameter reached this unrealistic lower bound of 0.1 fm. Also, the extracted λ parameters are too low.

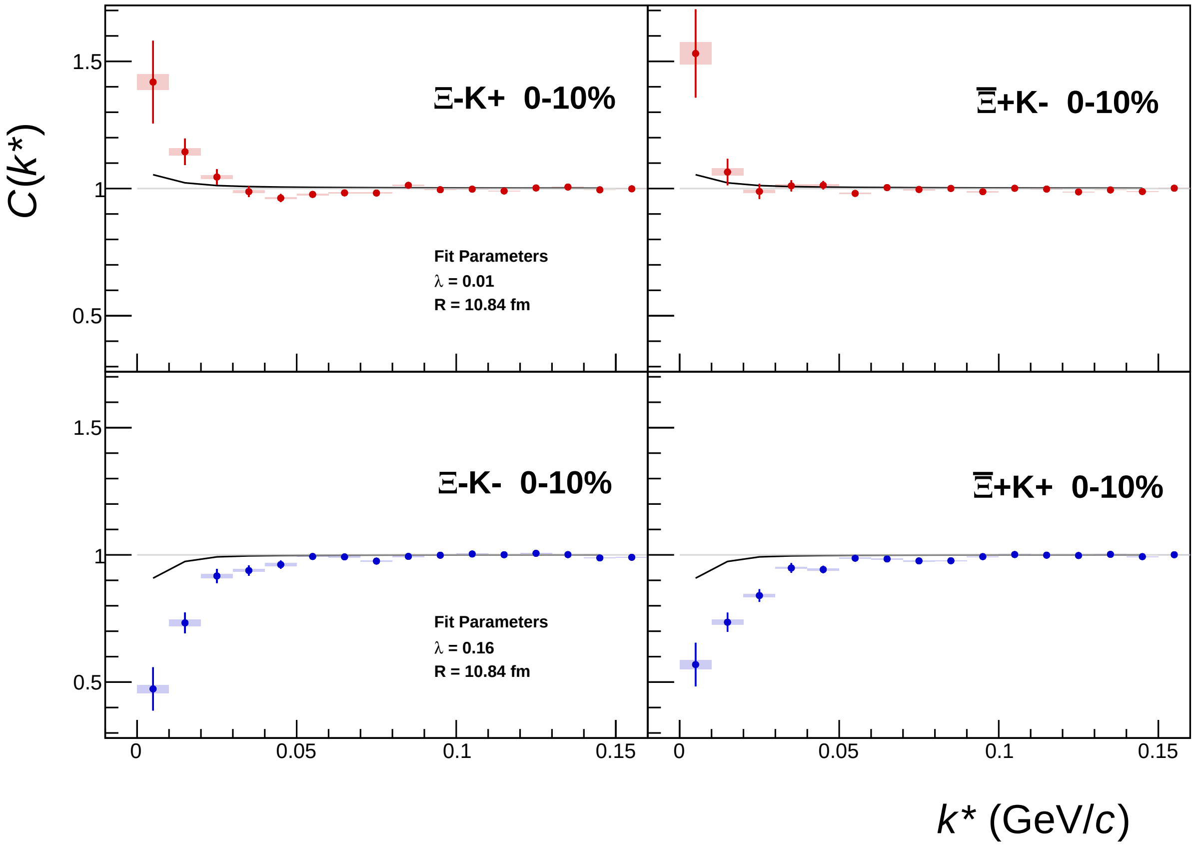

Fig. 44: $\Xi K^{\pm}$ Global Coulomb-only fit (Set 2) for 0-10% centrality. In this fit, the parameters were all unbounded, and the radius parameter was initialized to 10 fm. In this case, the radius parameters reamins high, and ends at an unrealistic value of 10.84 fm. Also, the extracted λ parameters are too low.

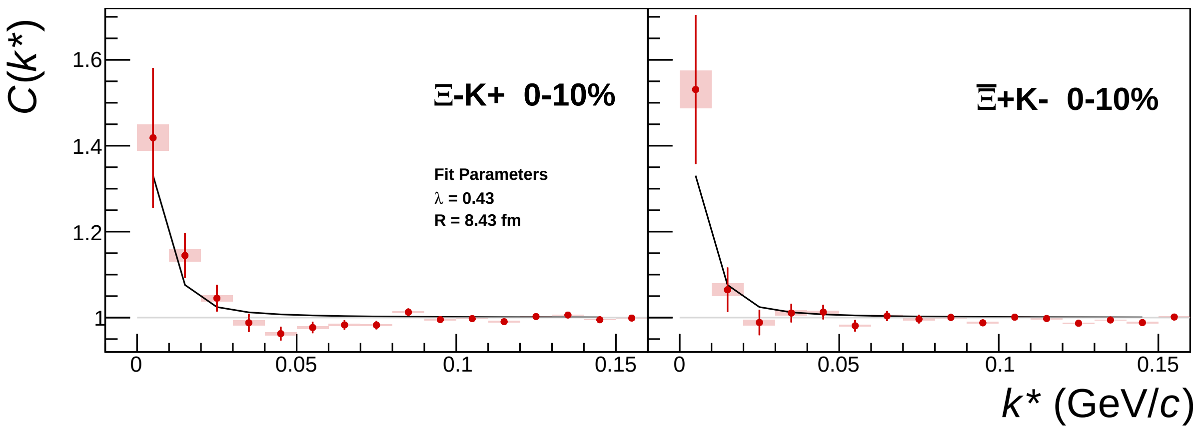

Fig. 45: $\Xi^{-}K^{+}$ Coulomb-only fit for 0-10% centrality

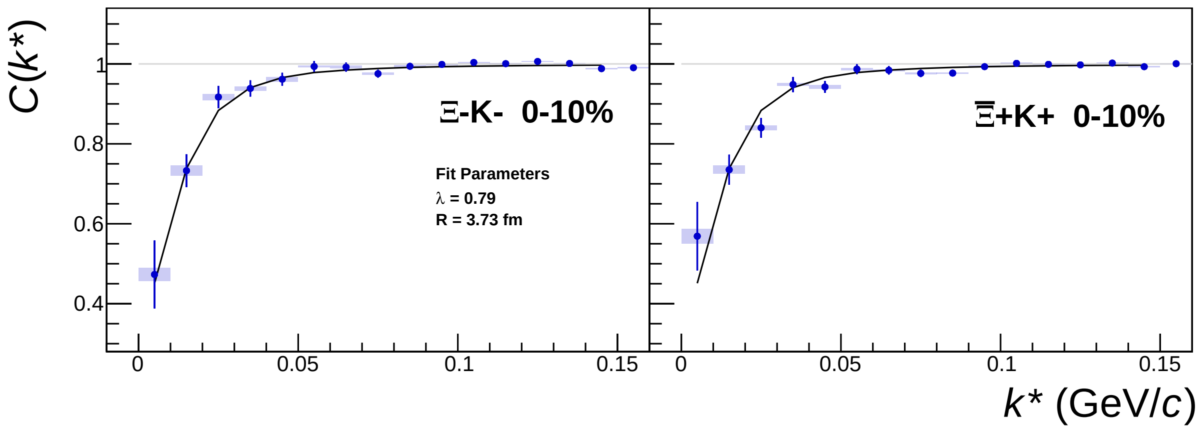

Fig. 46: $\Xi^{-}K^{-}$ Coulomb-only fit for 0-10% centrality

692 # 9 Additional Figures

693 ## 9.1 Residuals

694 ### *9.1.1 ΛK^{+} Residuals*

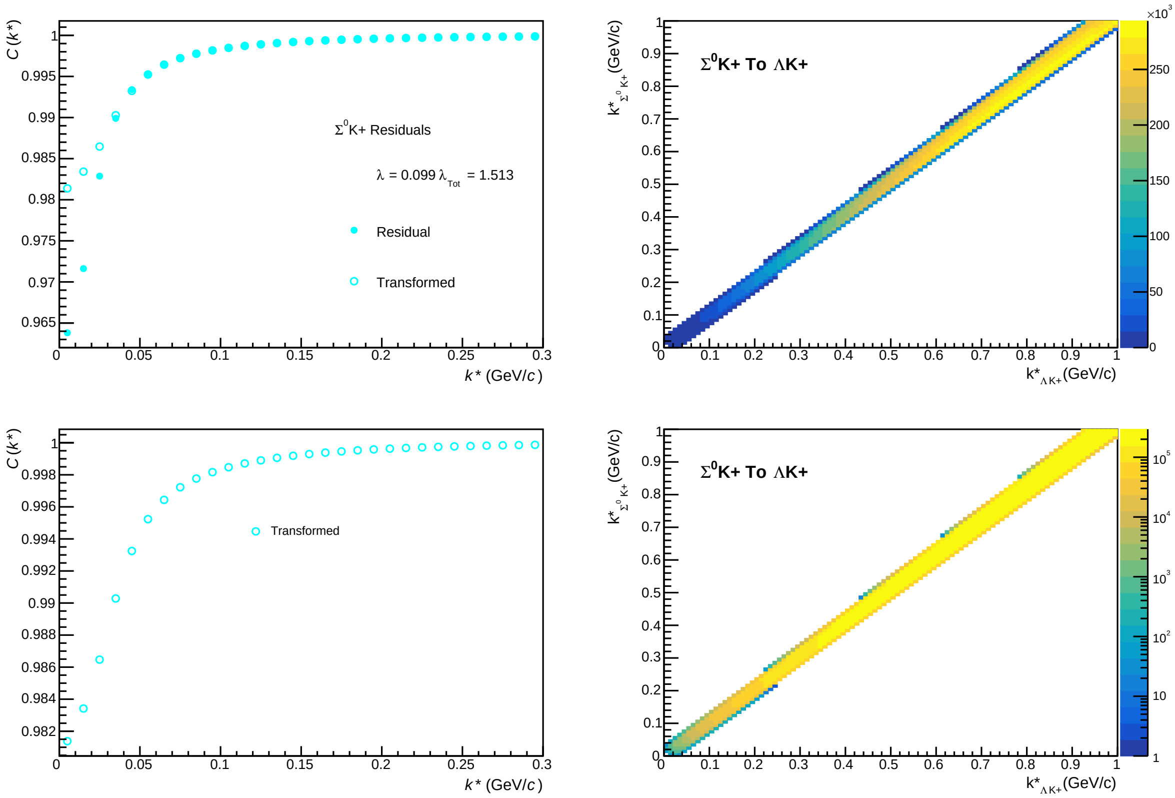

Fig. 47: Residuals: Σ^0K^+ to ΛK^+ (0-10% Centrality)

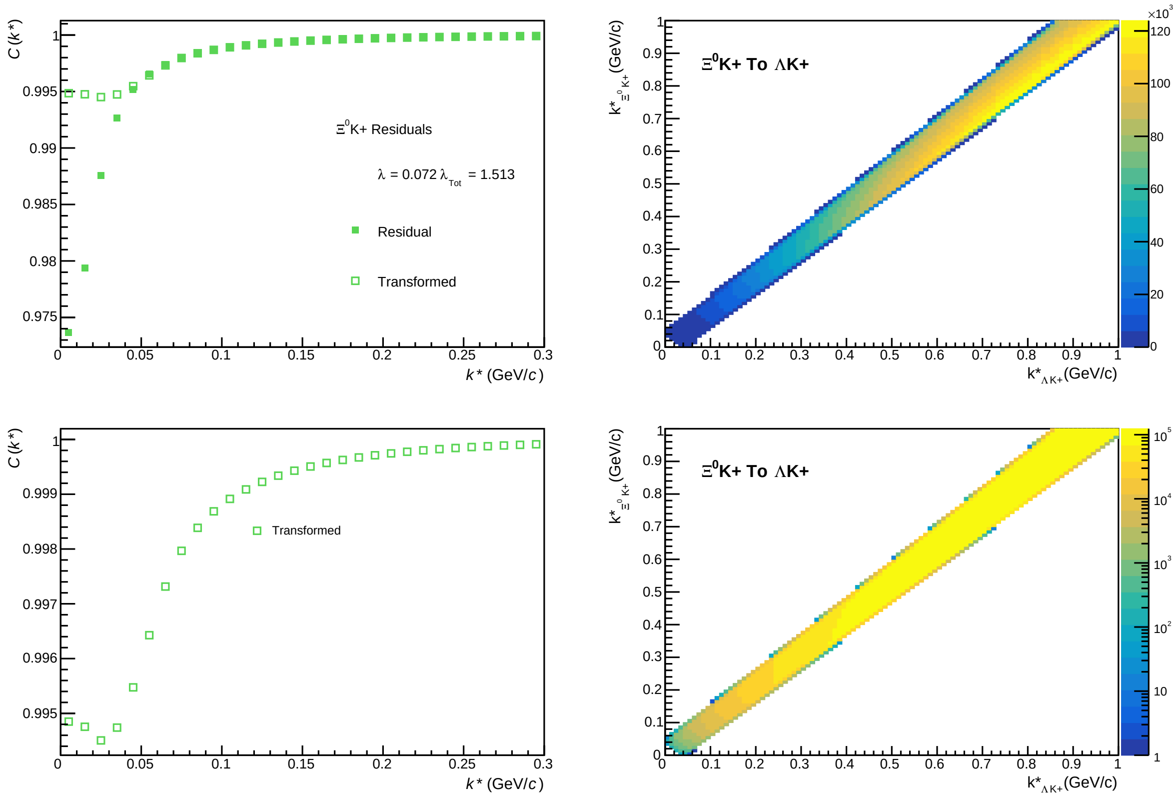

Fig. 48: Residuals: Ξ^0K$^+$ to ΛK$^+$ (0-10% Centrality)

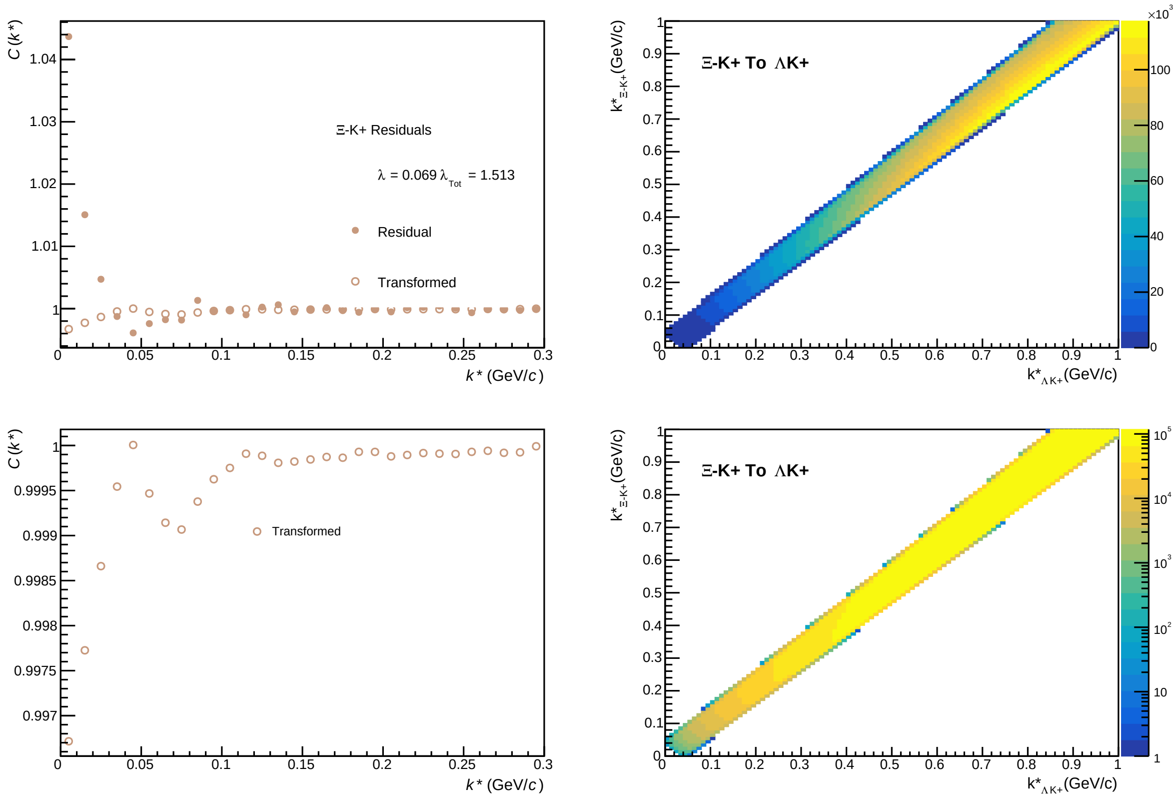

Fig. 49: Residuals: Ξ^-K$^+$ to ΛK$^+$ (0-10% Centrality)

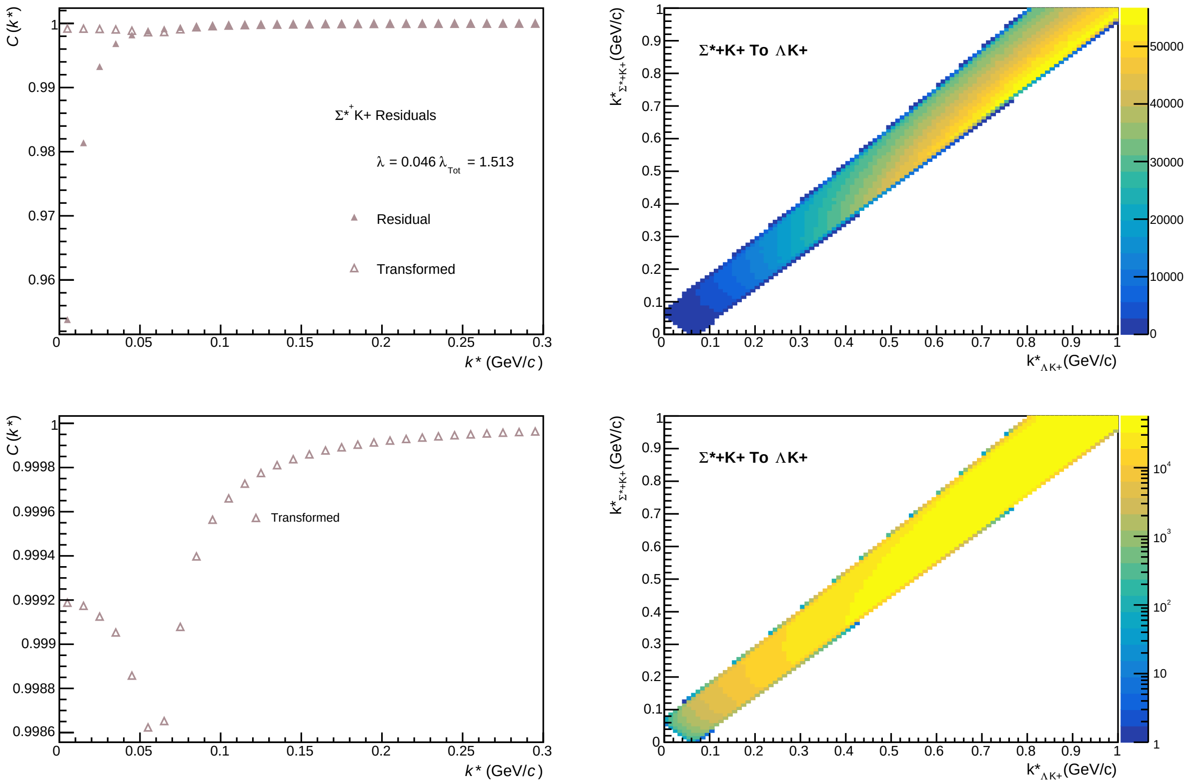

Fig. 50: Residuals: $\Sigma^{*+}K^{+}$ to ΛK^{+} (0-10% Centrality)

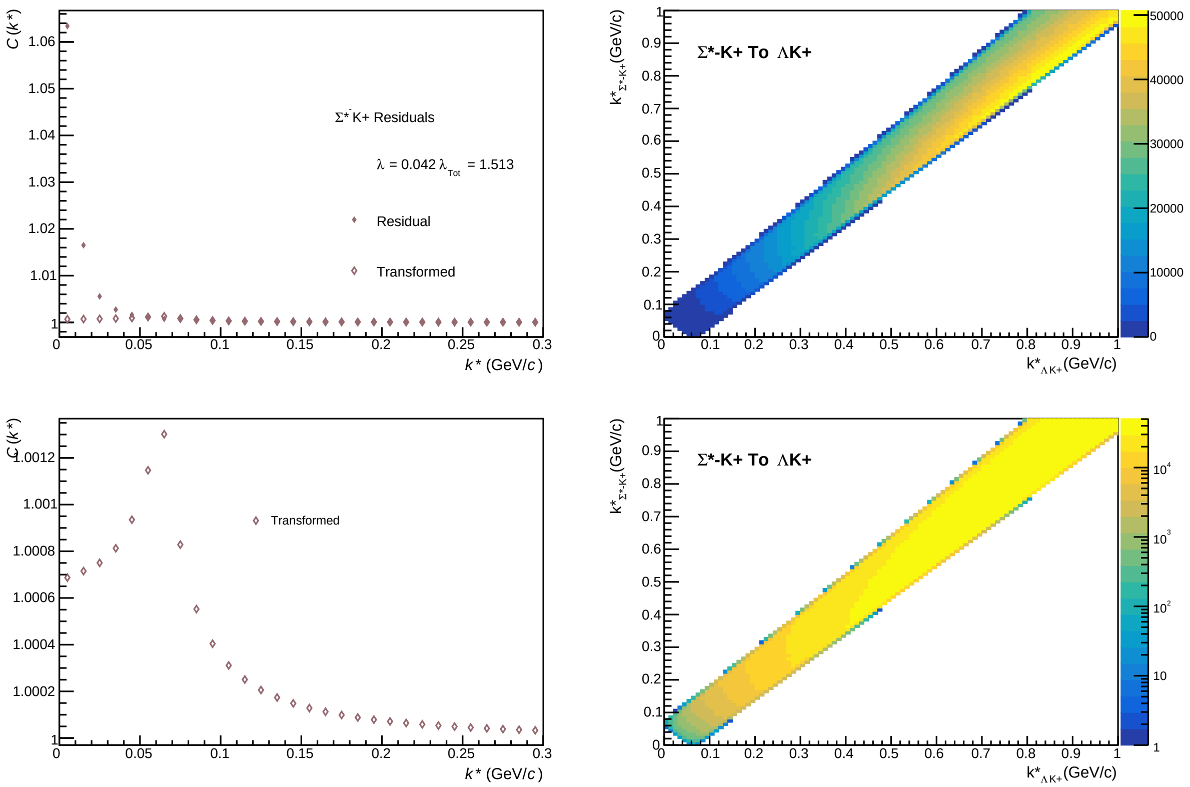

Fig. 51: Residuals: $\Sigma^{*-}K^{+}$ to ΛK^{+} (0-10% Centrality)

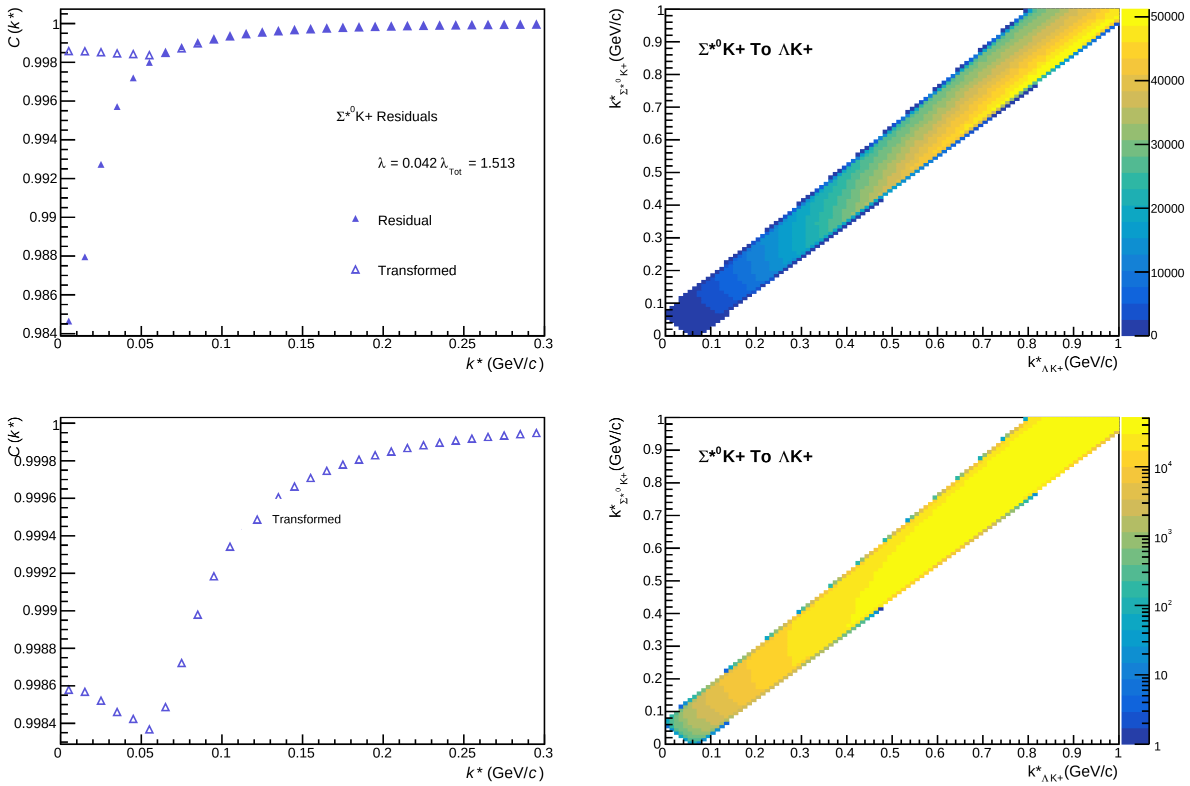

Fig. 52: Residuals: $\Sigma^{*0}K^{+}$ to ΛK^{+} (0-10% Centrality)

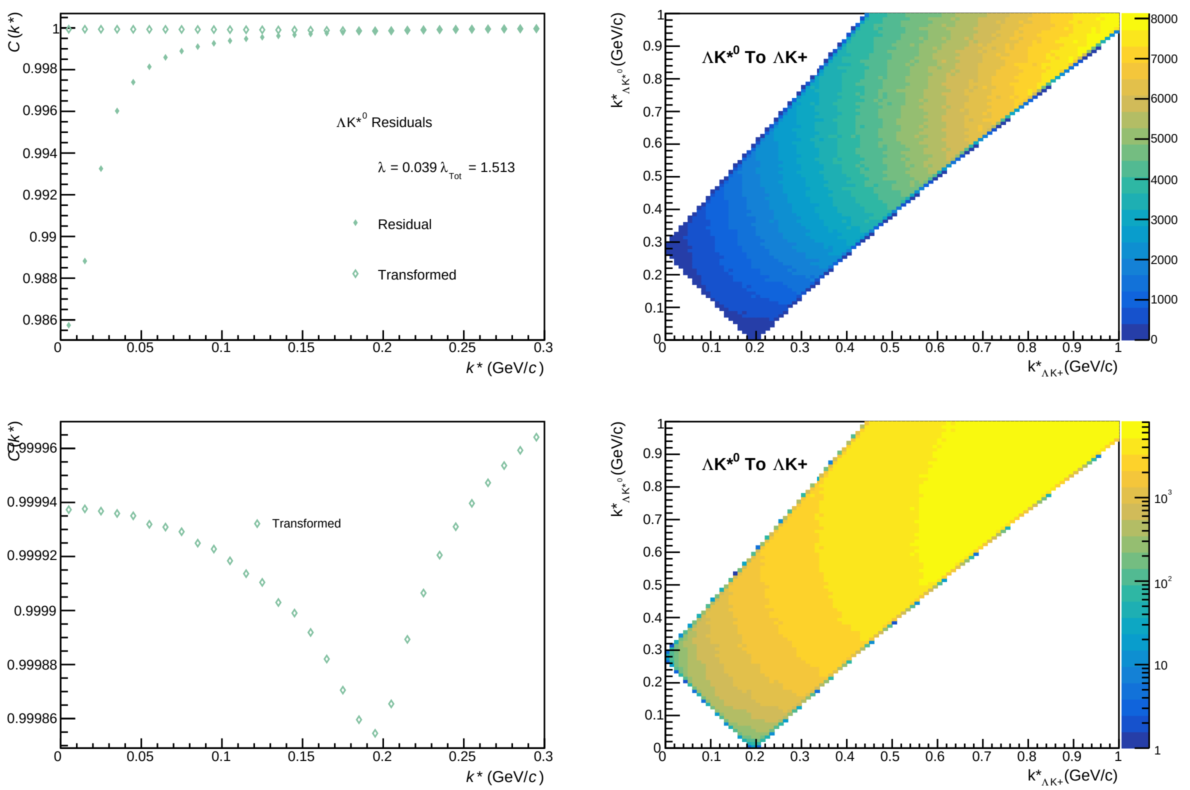

Fig. 53: Residuals: ΛK^{*0} to ΛK^{+} (0-10% Centrality)

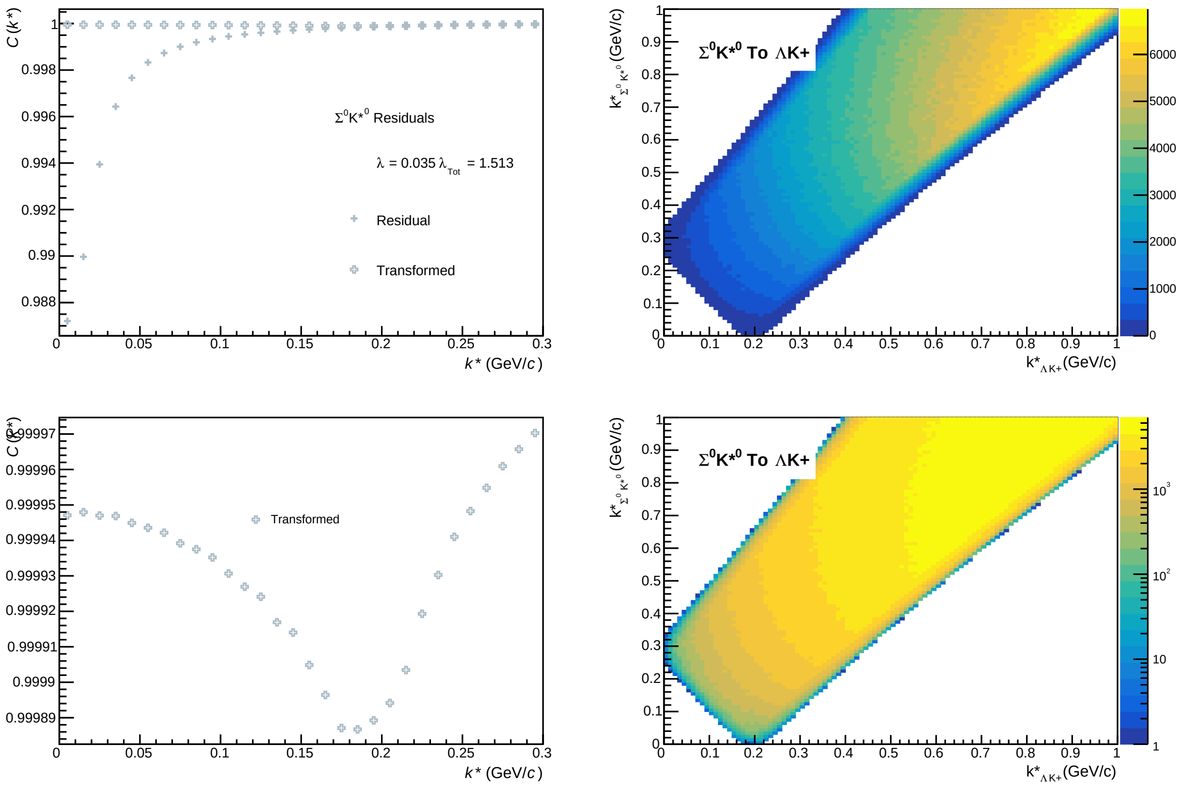

Fig. 54: Residuals: $\Sigma^0 K^{*0}$ to ΛK^+ (0-10% Centrality)

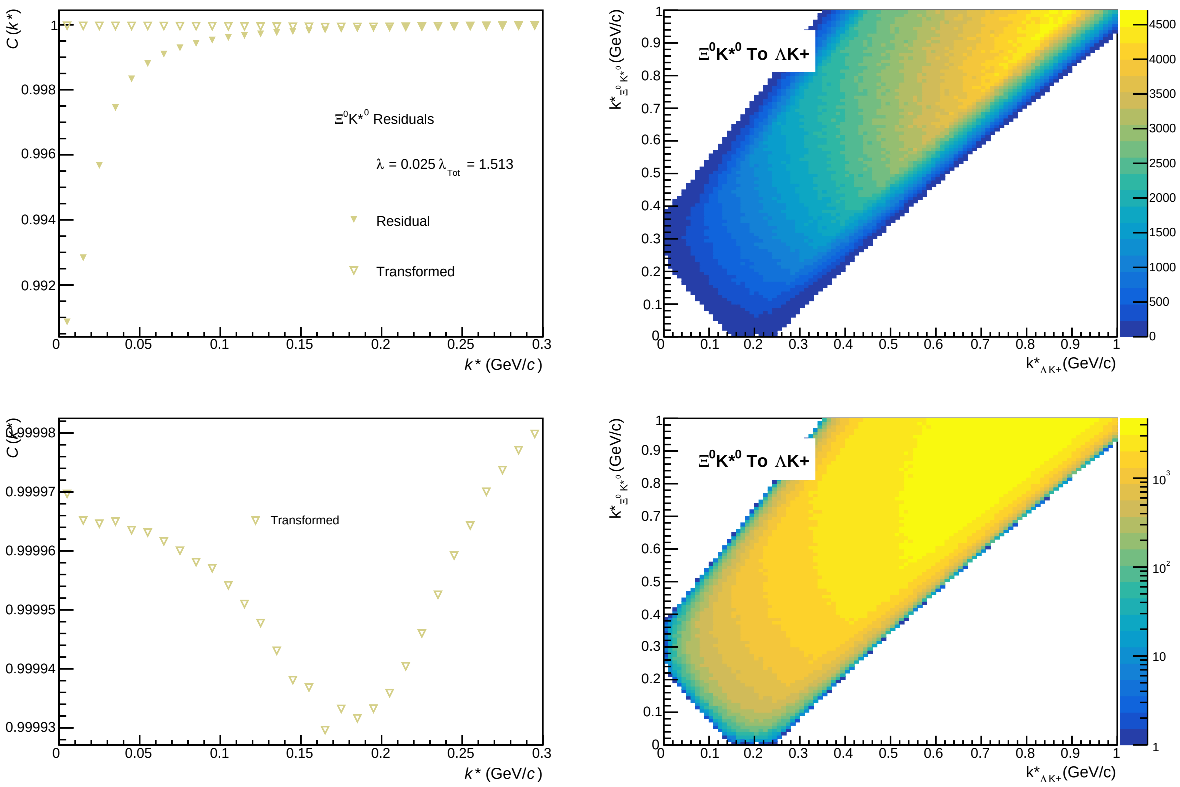

Fig. 55: Residuals: $\Xi^0 K^{*0}$ to ΛK^+ (0-10% Centrality)

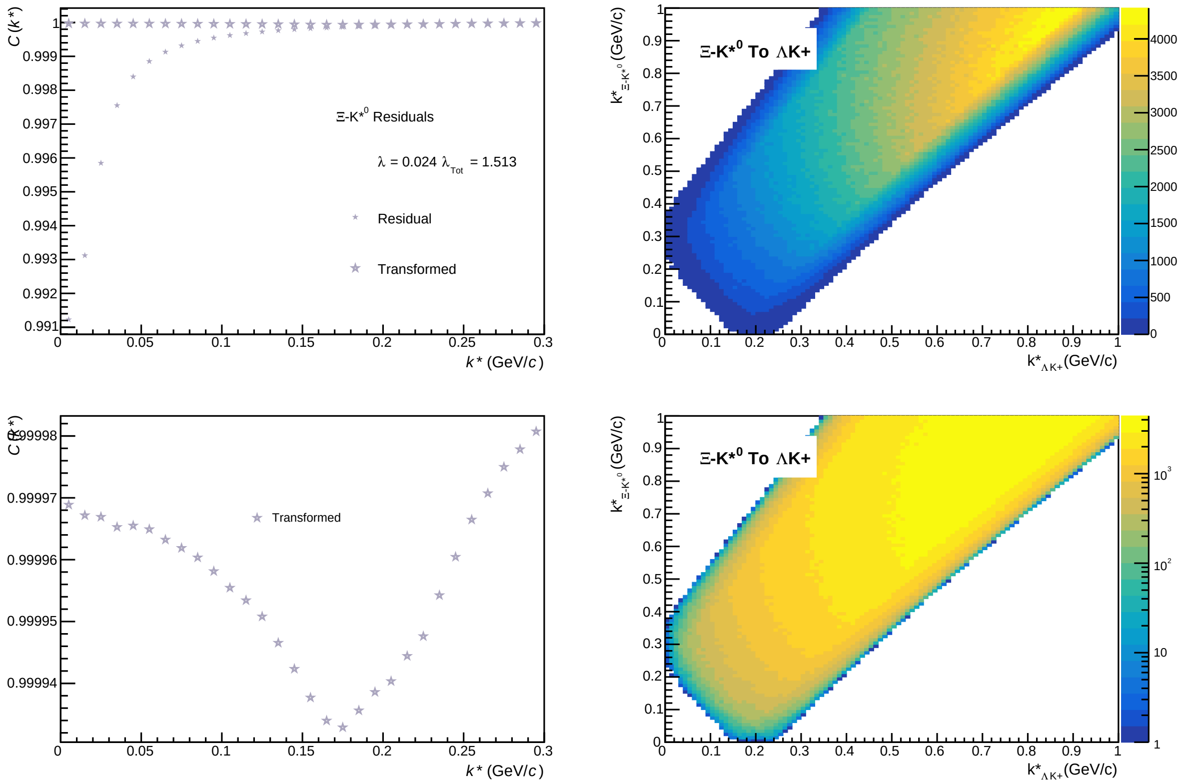

Fig. 56: Residuals: $\Xi^{-}K^{*0}$ to ΛK^{+} (0-10% Centrality)

695 ### 9.1.2 ΛK^- Residuals

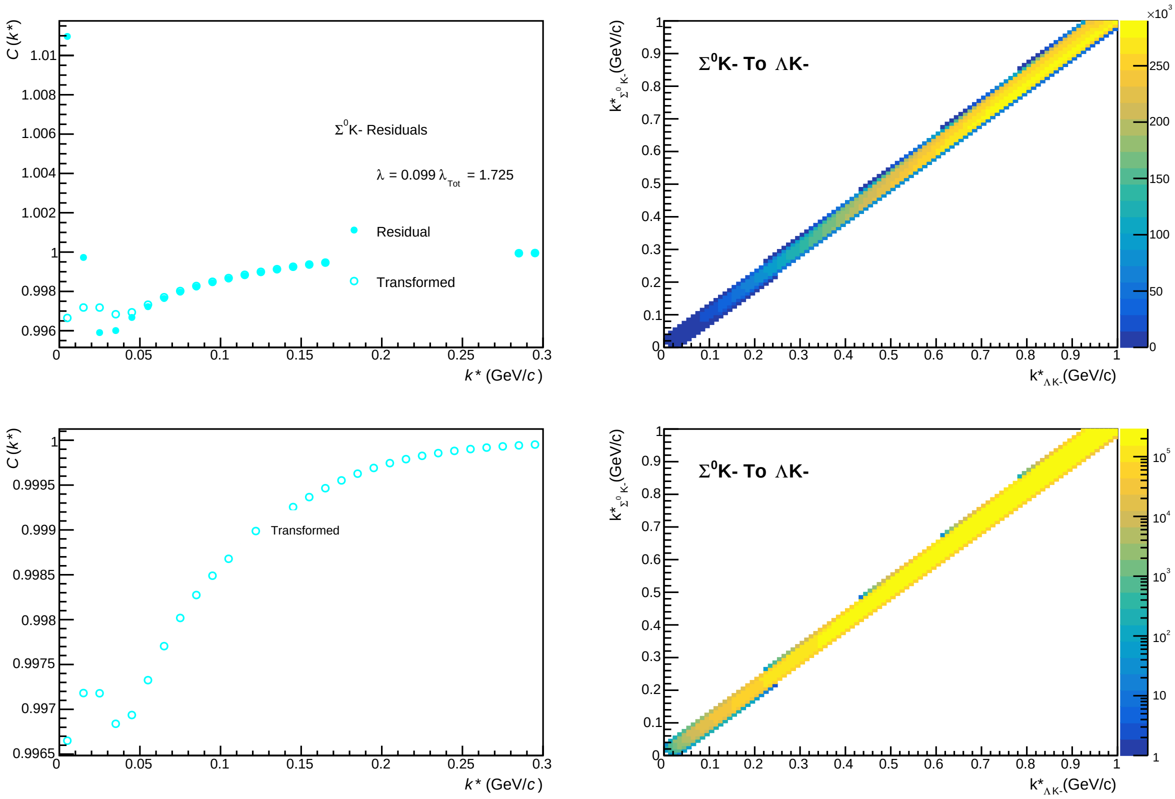

Fig. 57: Residuals: Σ^0K^- to ΛK^- (0-10% Centrality)

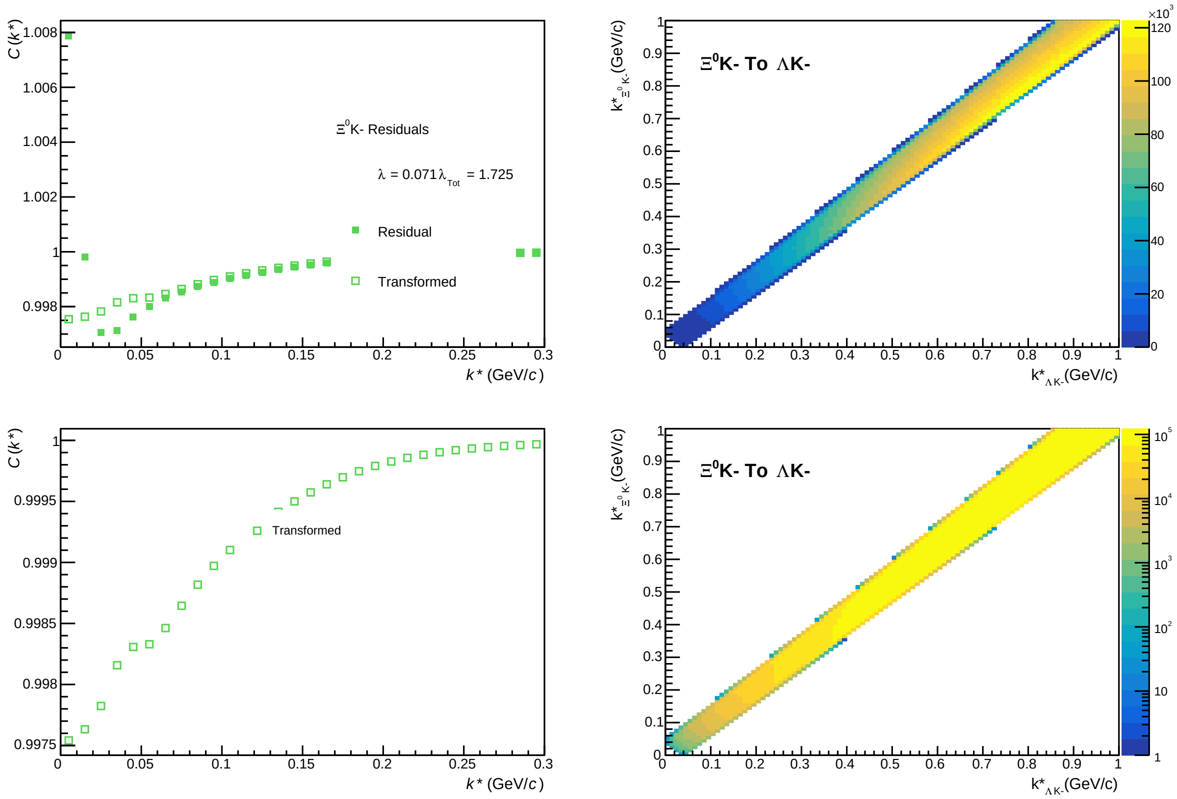

Fig. 58: Residuals: $\Xi^0\mathrm{K}^-$ to $\Lambda\mathrm{K}^-$ (0-10% Centrality)

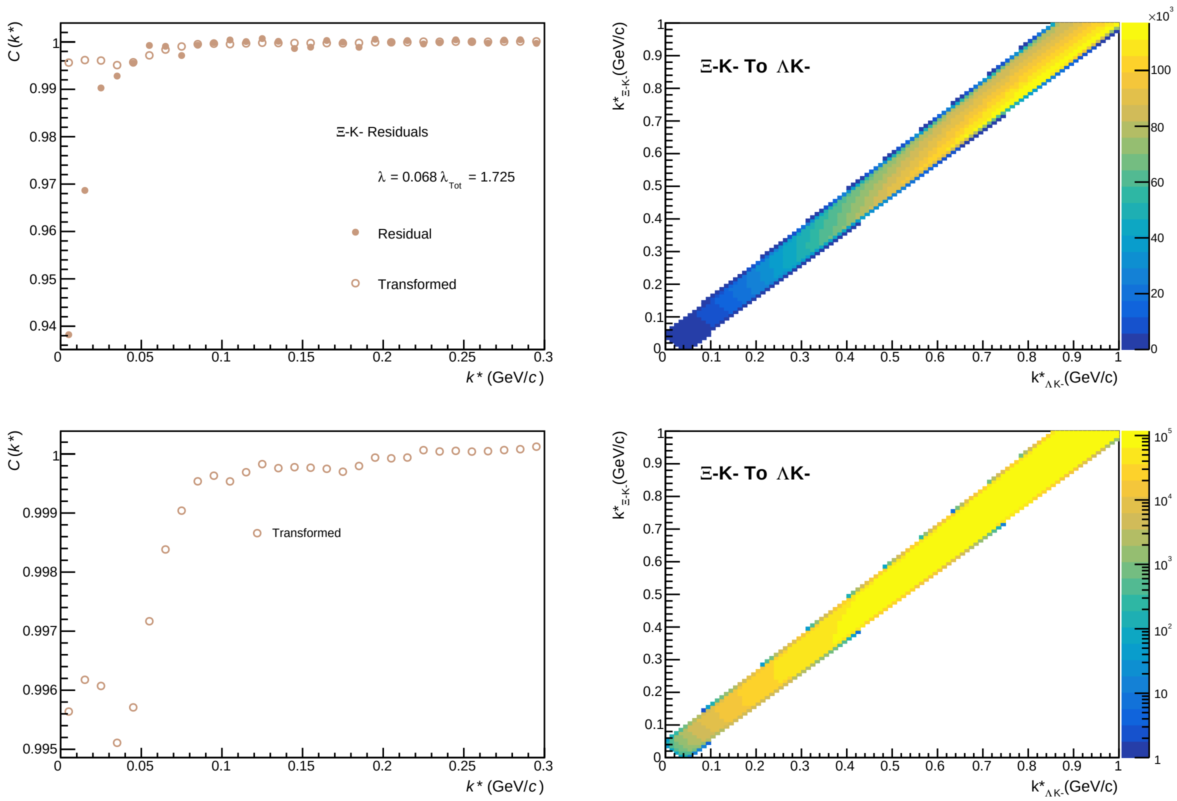

Fig. 59: Residuals: $\Xi^-\mathrm{K}^-$ to $\Lambda\mathrm{K}^-$ (0-10% Centrality)

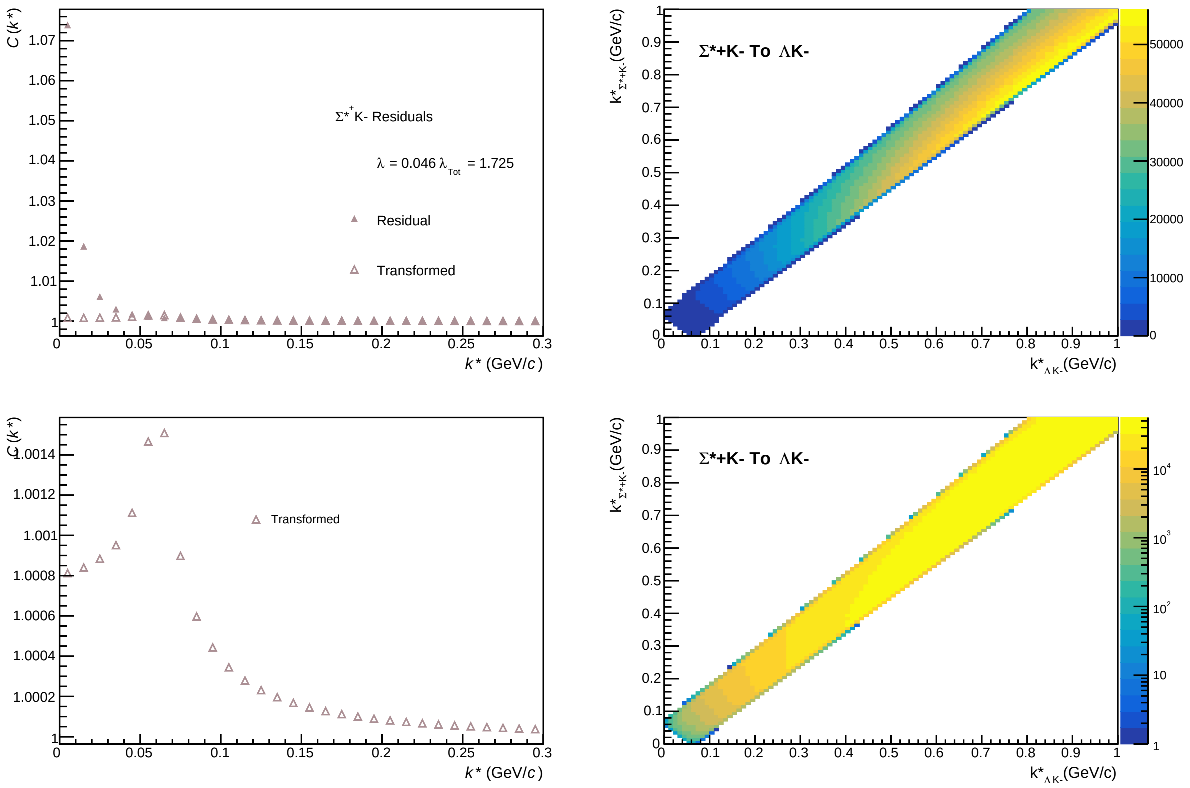

Fig. 60: Residuals: $\Sigma^{*+}K^{-}$ to ΛK^{-} (0-10% Centrality)

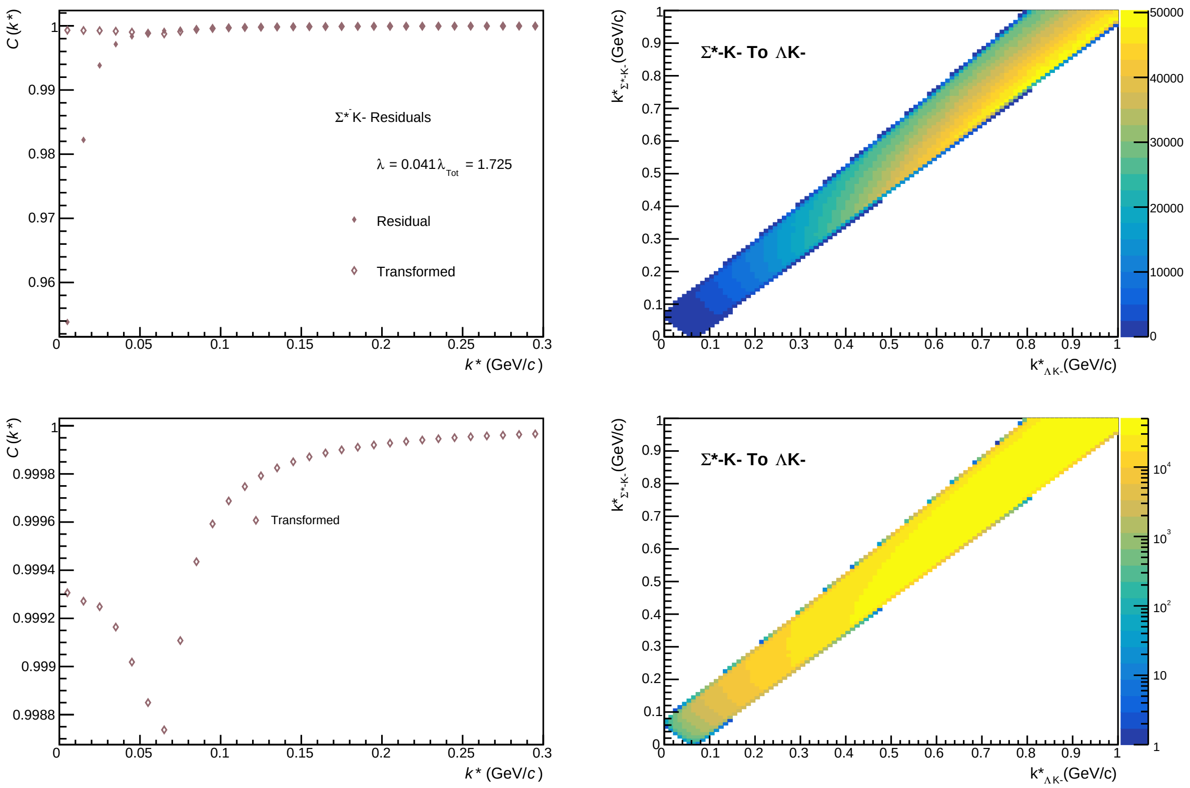

Fig. 61: Residuals: $\Sigma^{*-}K^{-}$ to ΛK^{-} (0-10% Centrality)

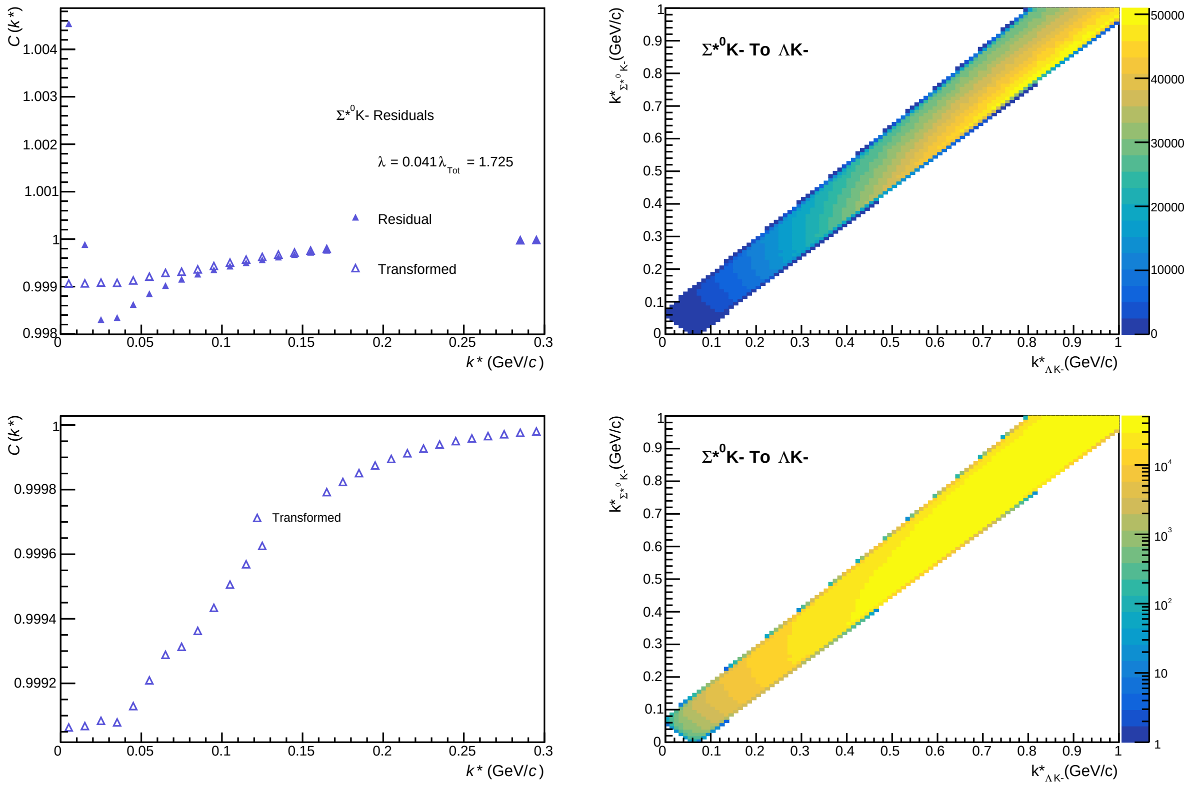

Fig. 62: Residuals: $\Sigma^{*0}K^-$ to ΛK^- (0-10% Centrality)

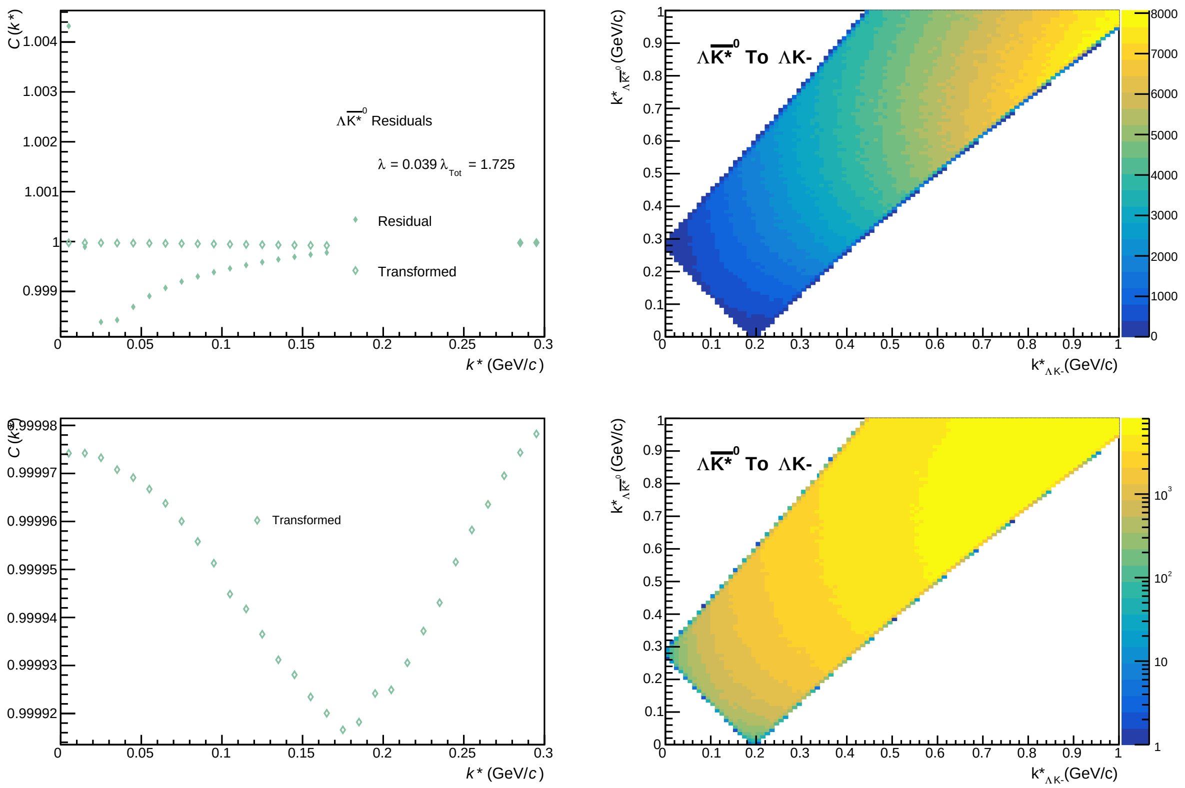

Fig. 63: Residuals: $\Lambda\bar{K}^{*0}$ to ΛK^- (0-10% Centrality)

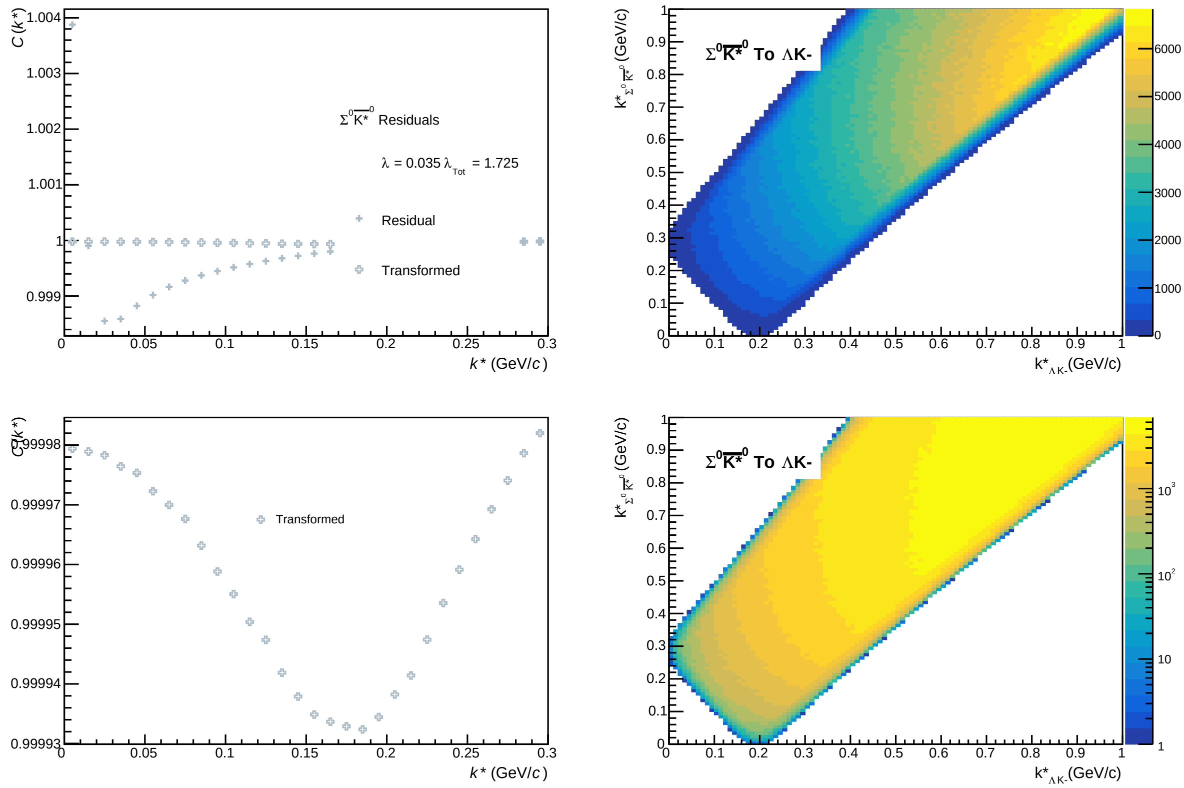

Fig. 64: Residuals: $\Sigma^0\bar{K}^{*0}$ to ΛK^- (0-10% Centrality)

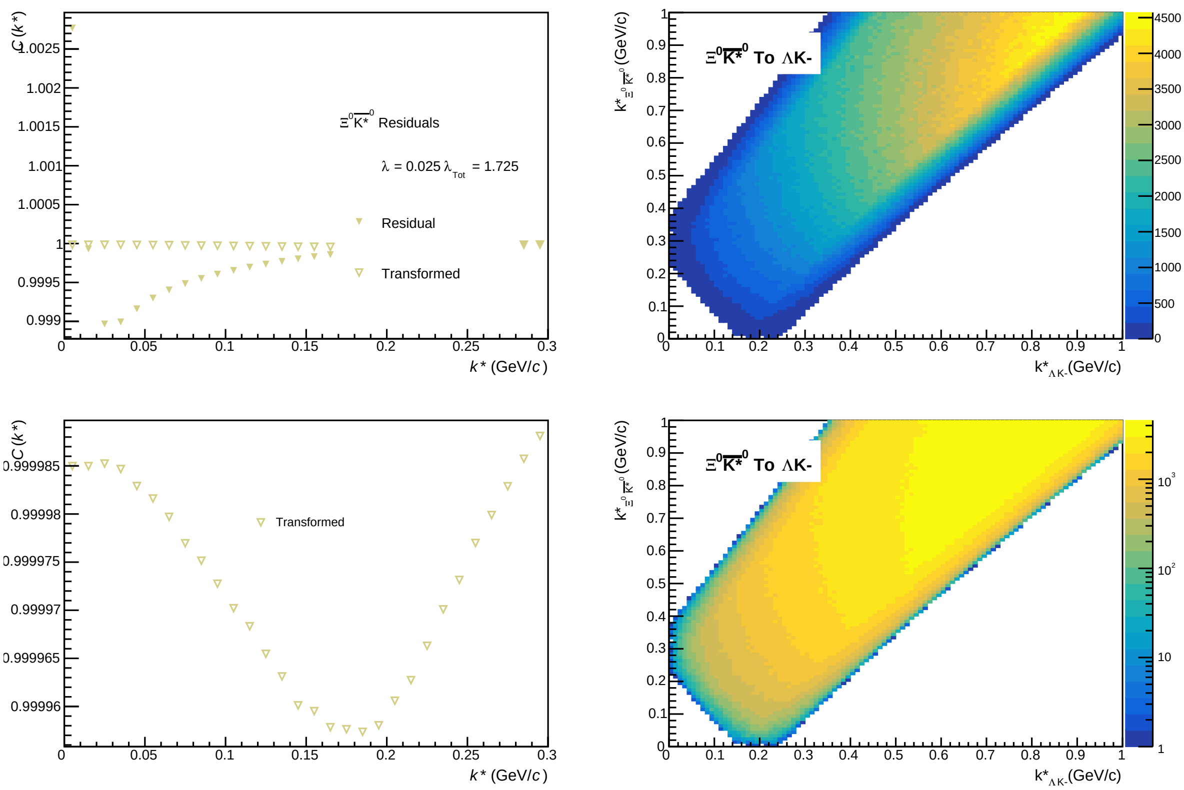

Fig. 65: Residuals: $\Xi^0\bar{K}^{*0}$ to ΛK^- (0-10% Centrality)

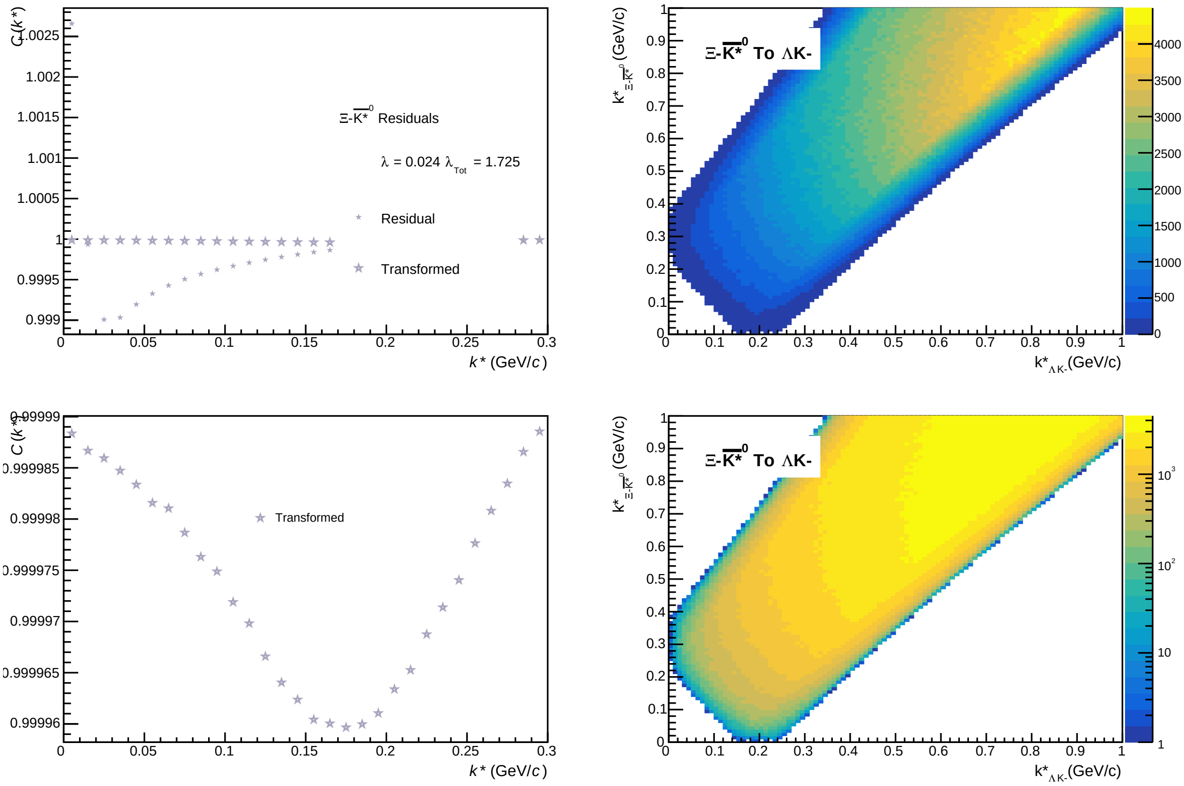

Fig. 66: Residuals: $\Xi^-\bar{K}^{*0}$ to ΛK^- (0-10% Centrality)

696 9.1.3 ΛK^0_S Residuals

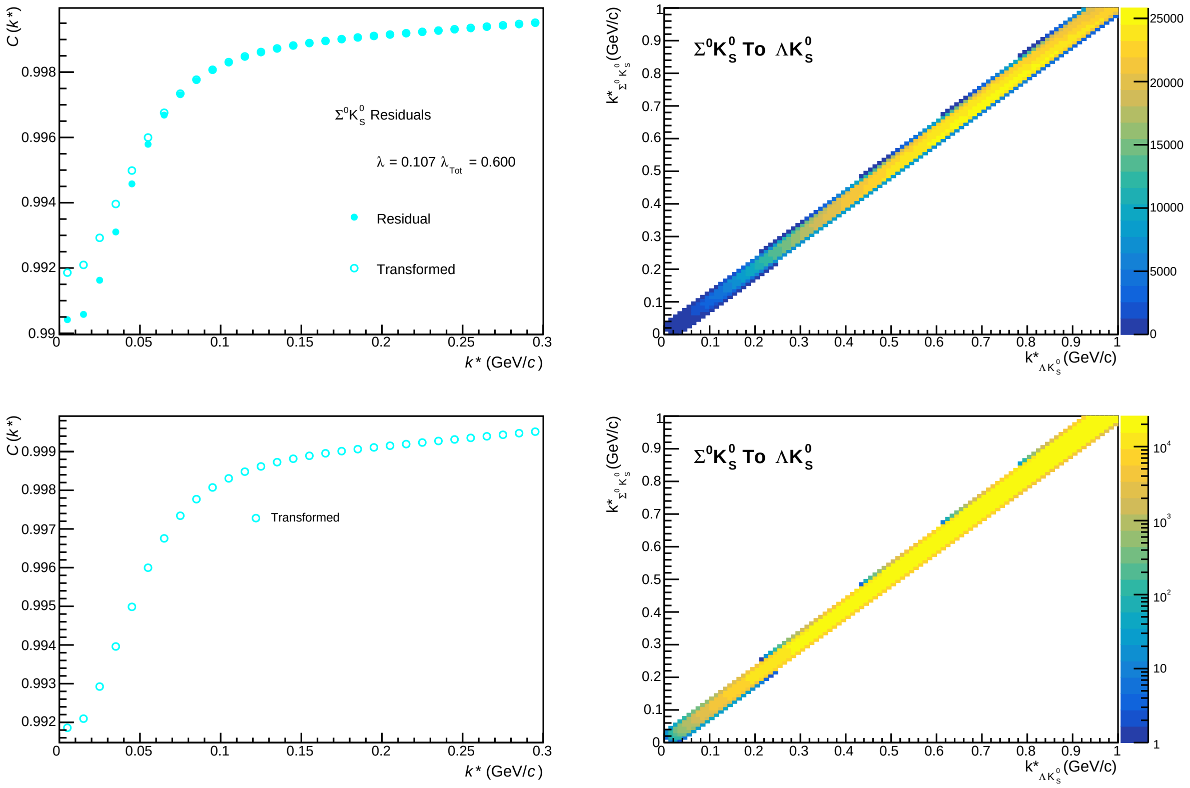

Fig. 67: Residuals: $\Sigma^0 K^0_S$ to ΛK^0_S (0-10% Centrality)

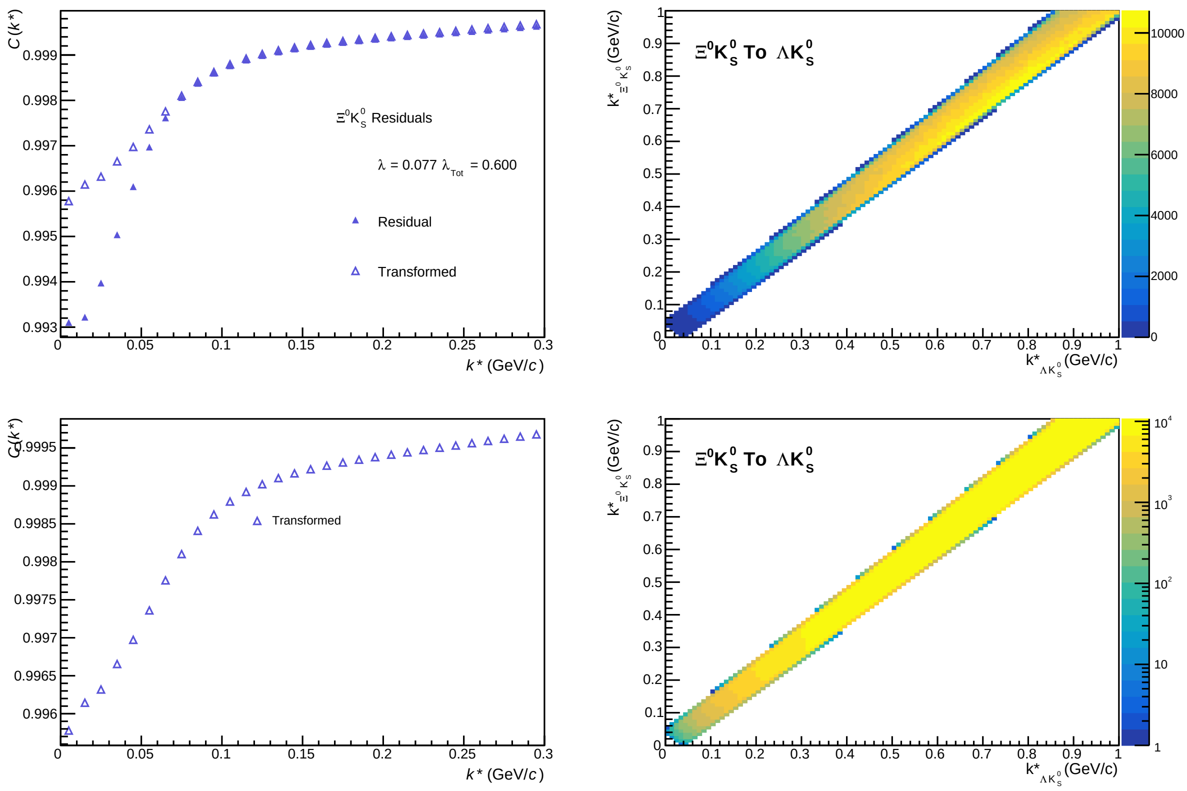

Fig. 68: Residuals: $\Xi^0 K^0_S$ to ΛK^0_S (0-10% Centrality)

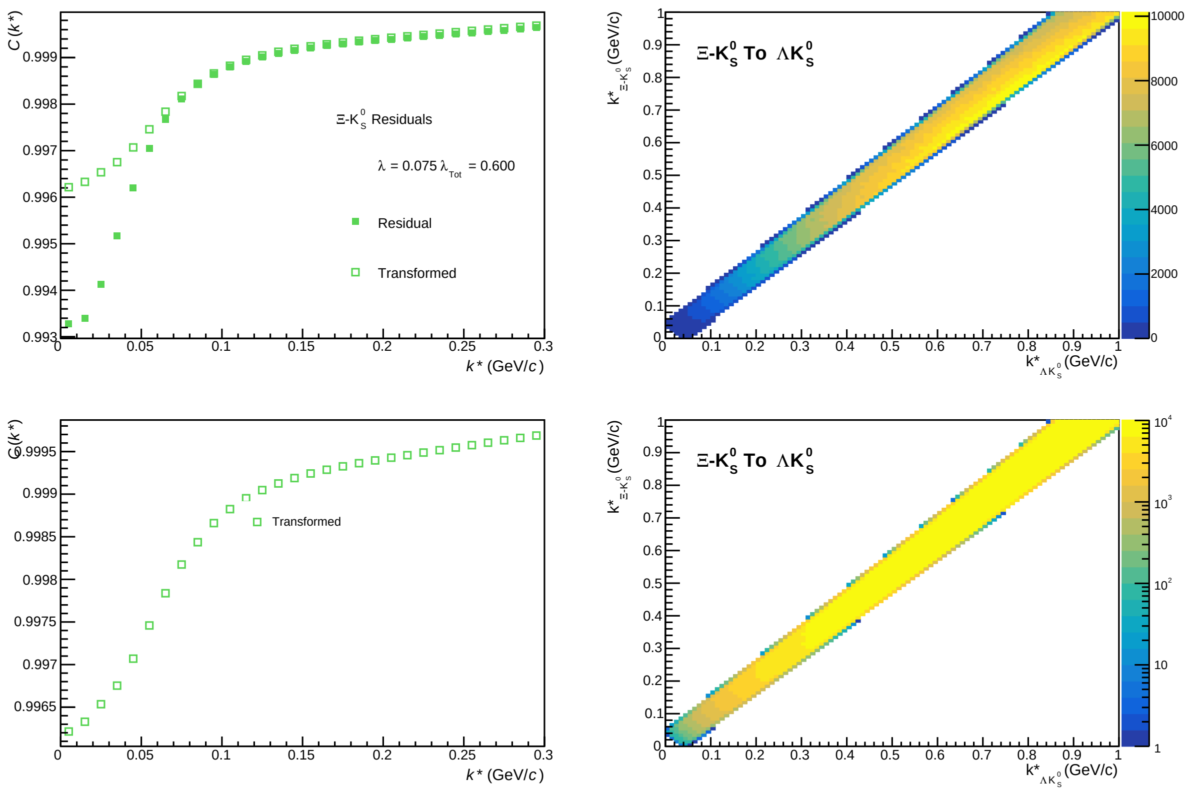

Fig. 69: Residuals: $\Xi^- K^0_S$ to ΛK^0_S (0-10% Centrality)

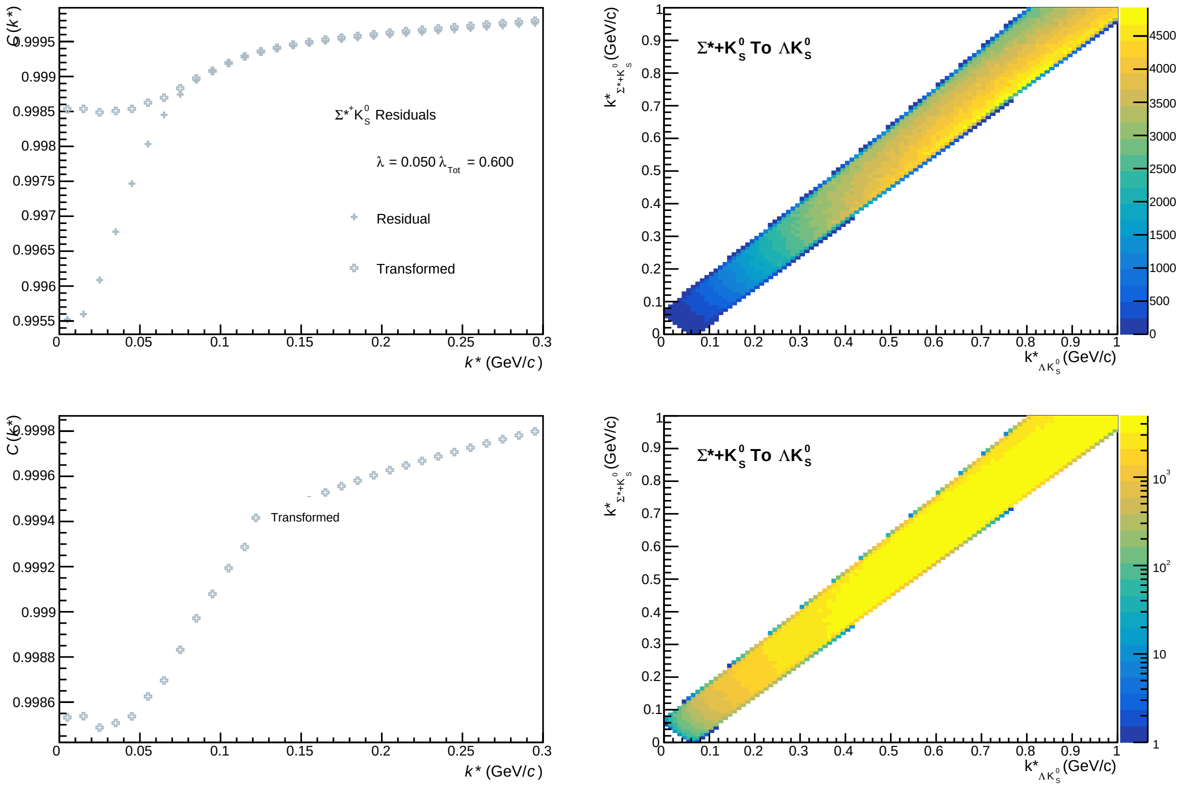

Fig. 70: Residuals: $\Sigma^{*+}K^0_S$ to ΛK^0_S (0-10% Centrality)

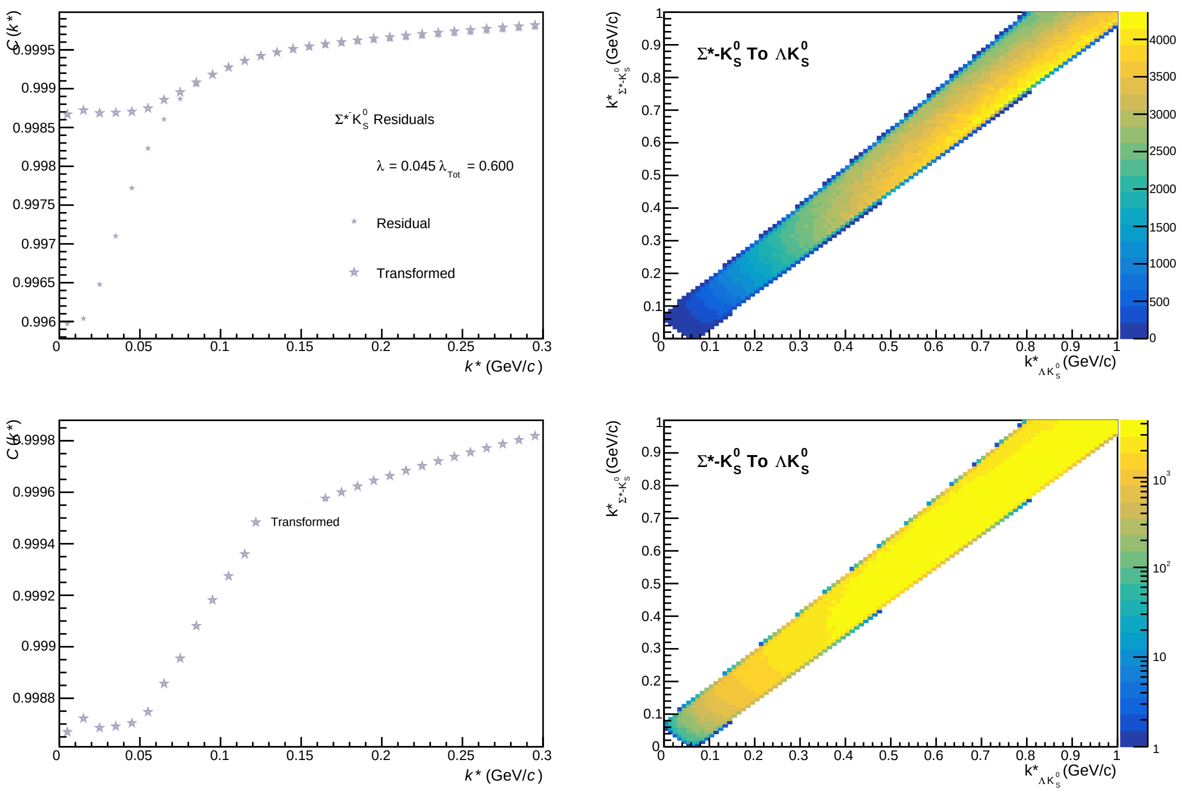

Fig. 71: Residuals: $\Sigma^{*-}K^0_S$ to ΛK^0_S (0-10% Centrality)

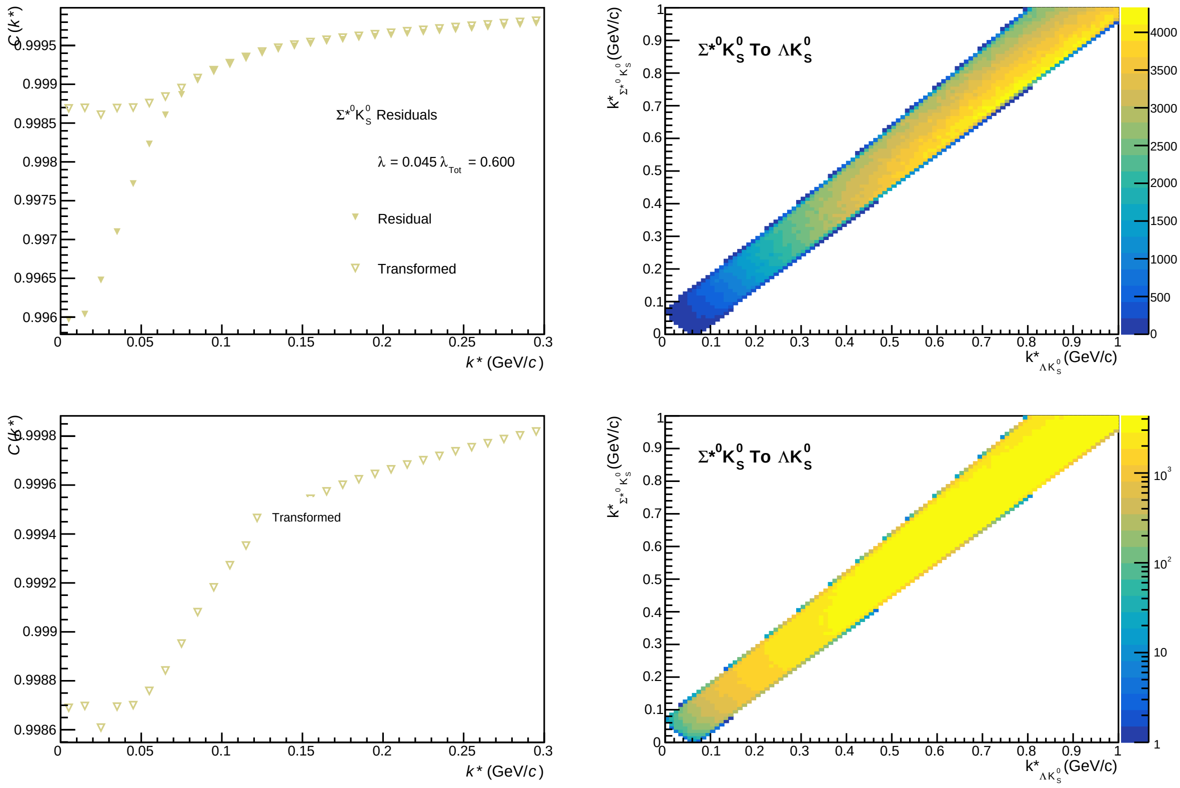

Fig. 72: Residuals: $\Sigma^{*0}K^0_S$ to ΛK^0_S (0-10% Centrality)

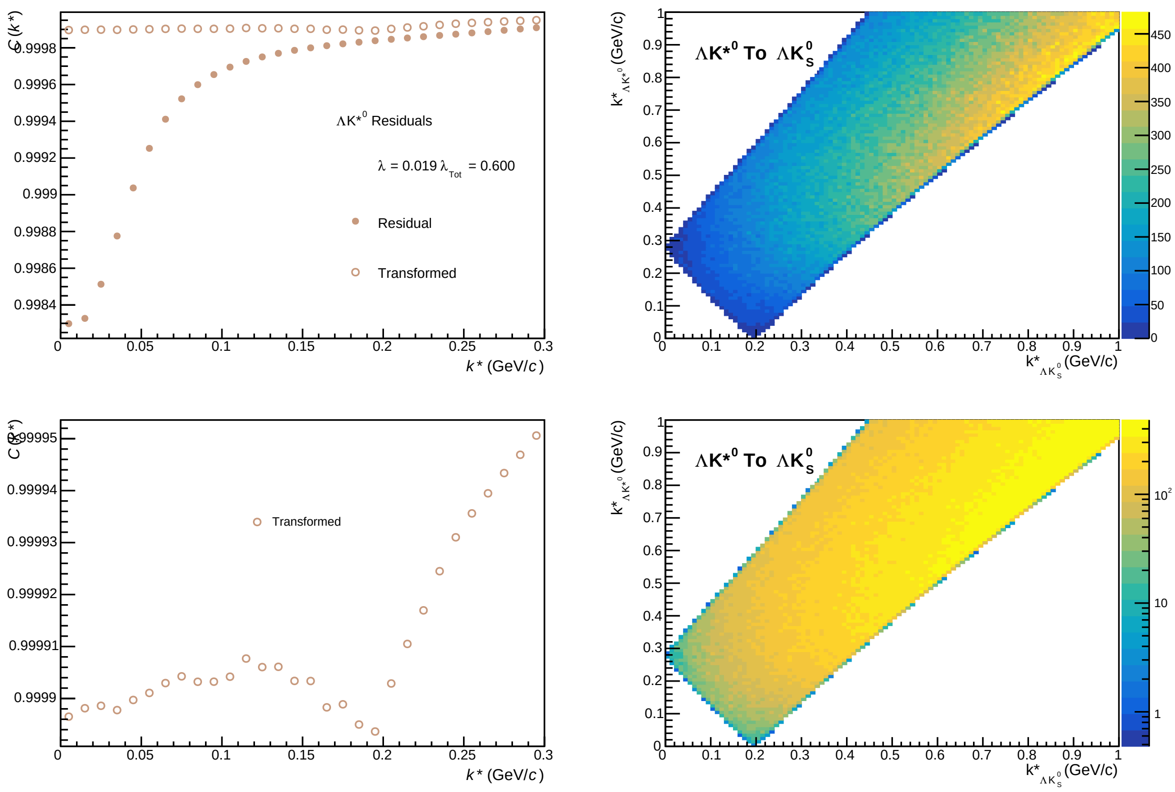

Fig. 73: Residuals: ΛK^{*0} to ΛK^0_S (0-10% Centrality)

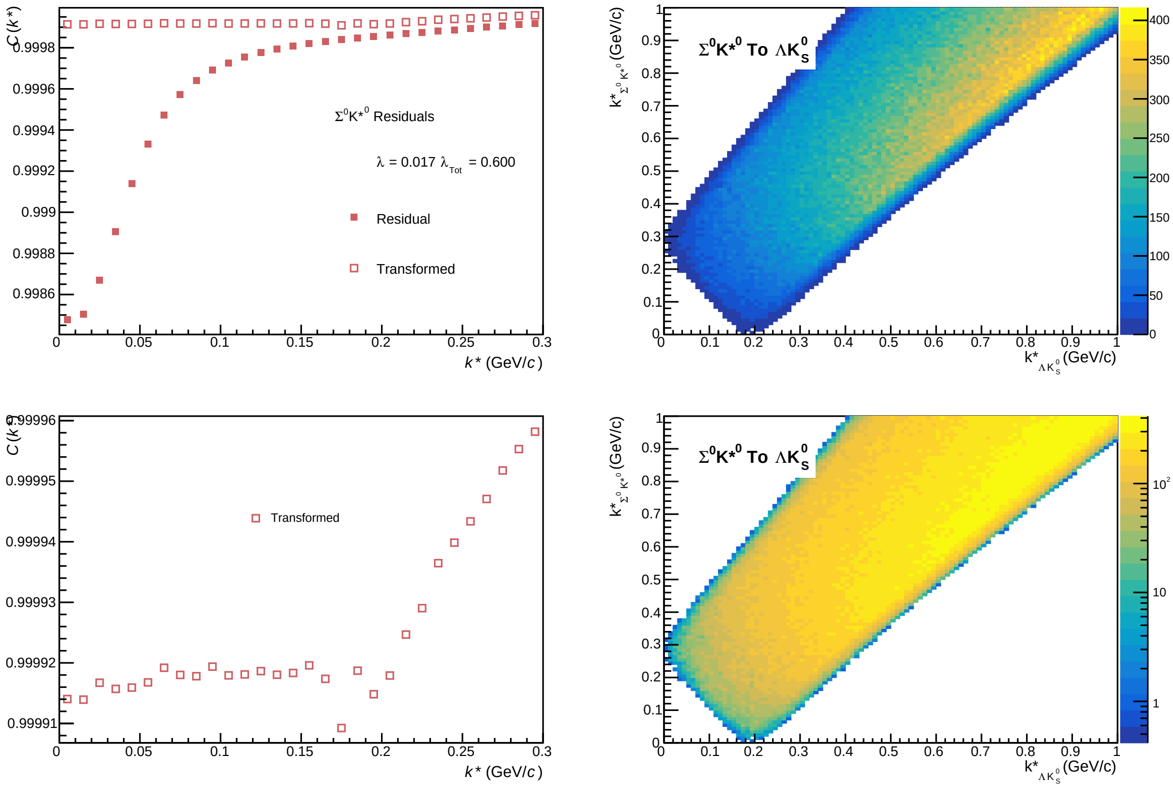

Fig. 74: Residuals: Σ^0K^{*0} to ΛK^0_S (0-10% Centrality)

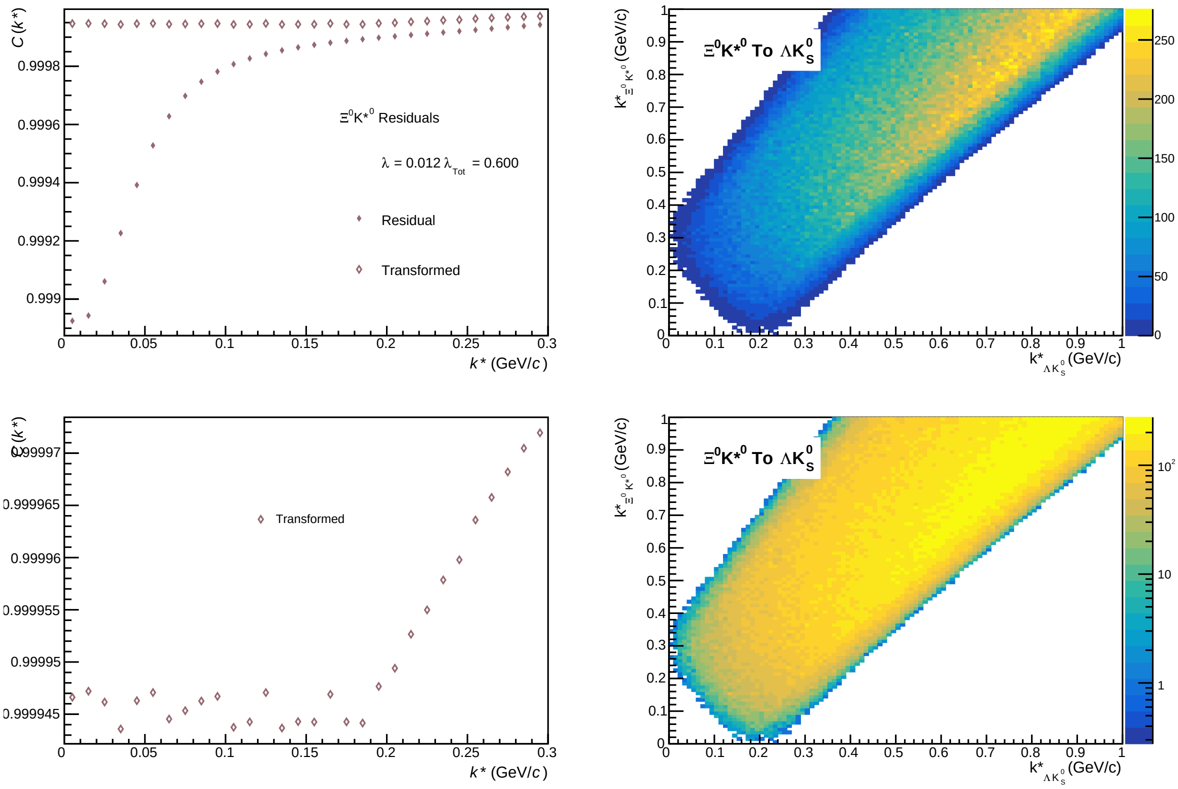

Fig. 75: Residuals: Ξ^0K^{*0} to ΛK^0_S (0-10% Centrality)

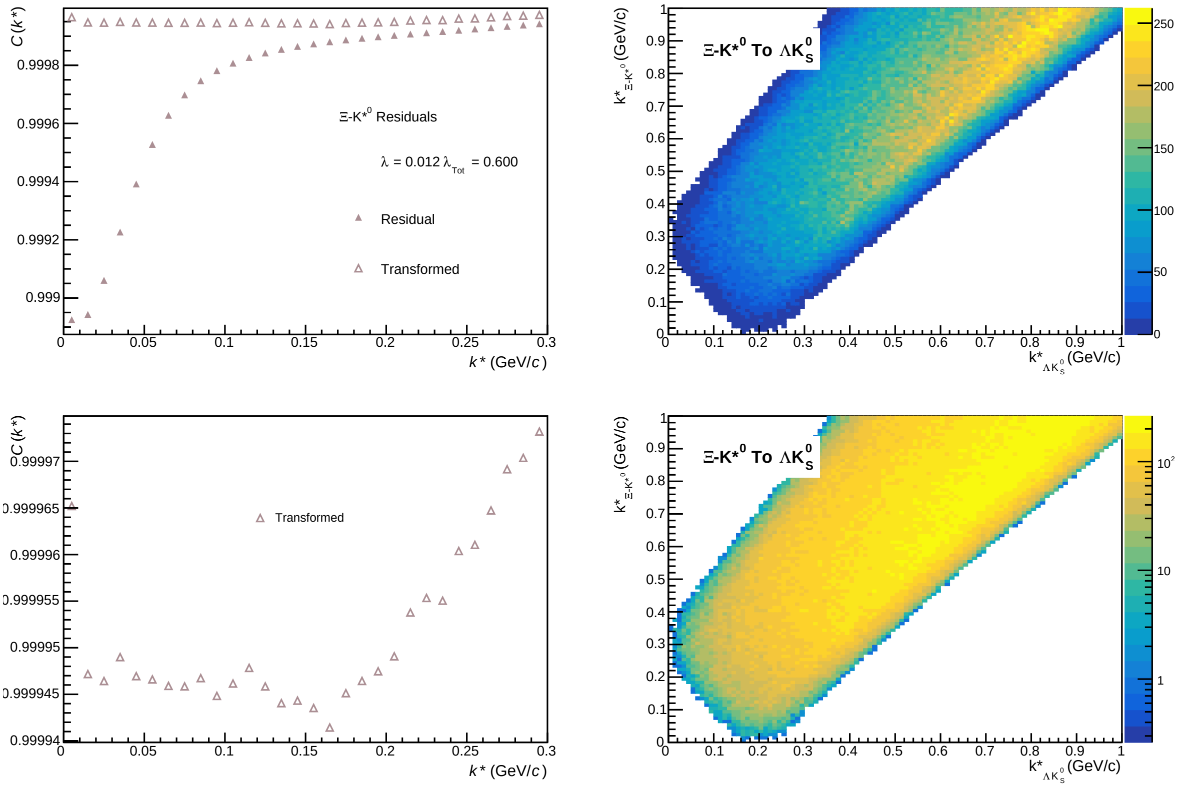

Fig. 76: Residuals: $\Xi^{-}K^{*0}$ to ΛK^{0}_{S} (0-10% Centrality)

References

[1] R. Lednicky and V. L. Lyuboshitz. *Sov. J. Nucl. Phys.*, 35:770, 1982.

[2] Michael Annan Lisa, Scott Pratt, Ron Soltz, and Urs Wiedemann. Femtoscopy in relativistic heavy ion collisions. *Ann. Rev. Nucl. Part. Sci.*, 55:357–402, 2005.

[3] S. E. Koonin. Proton Pictures of High-Energy Nuclear Collisions. *Phys. Lett.*, B70:43–47, 1977.

[4] S. Pratt, T. Csorgo, and J. Zimanyi. Detailed predictions for two pion correlations in ultrarelativistic heavy ion collisions. *Phys. Rev.*, C42:2646–2652, 1990.

[5] Richard Lednicky. Finite-size effects on two-particle production in continuous and discrete spectrum. *Phys. Part. Nucl.*, 40:307–352, 2009.

[6] Adam Kisiel, Hanna Zbroszczyk, and Maciej Szymaski. Extracting baryon-antibaryon strong interaction potentials from p$\bar{\Lambda}$ femtoscopic correlation functions. *Phys. Rev.*, C89(5):054916, 2014.

[7] Jai Salzwedel and Thomas Humanic. Lambda femtoscopy in $\sqrt{s_{NN}} = 2.76$ TeV Pb-Pb collisions at ALICE, Jan 2017. Presented 15 Dec 2016.

[8] Yan-Rui Liu and Shi-Lin Zhu. Meson-baryon scattering lengths in HB chi PT. *Phys. Rev.*, D75:034003, 2007.

[9] Maxim Mai, Peter C. Bruns, Bastian Kubis, and Ulf-G. Meissner. Aspects of meson-baryon scattering in three and two-flavor chiral perturbation theory. *Phys. Rev.*, D80:094006, 2009.

[10] Jaroslav Adam et al. One-dimensional pion, kaon, and proton femtoscopy in Pb-Pb collisions at $\sqrt{s_{\rm NN}}$ =2.76 TeV. *Phys. Rev.*, C92(5):054908, 2015.